



저작자표시-비영리-변경금지 2.0 대한민국

이용자는 아래의 조건을 따르는 경우에 한하여 자유롭게

- 이 저작물을 복제, 배포, 전송, 전시, 공연 및 방송할 수 있습니다.

다음과 같은 조건을 따라야 합니다:



저작자표시. 귀하는 원저작자를 표시하여야 합니다.



비영리. 귀하는 이 저작물을 영리 목적으로 이용할 수 없습니다.



변경금지. 귀하는 이 저작물을 개작, 변형 또는 가공할 수 없습니다.

- 귀하는, 이 저작물의 재이용이나 배포의 경우, 이 저작물에 적용된 이용허락조건을 명확하게 나타내어야 합니다.
- 저작권자로부터 별도의 허가를 받으면 이러한 조건들은 적용되지 않습니다.

저작권법에 따른 이용자의 권리는 위의 내용에 의하여 영향을 받지 않습니다.

이것은 [이용허락규약\(Legal Code\)](#)을 이해하기 쉽게 요약한 것입니다.

[Disclaimer](#)

공학박사학위논문

**Tailless Flapping-wing Micro Aerial Vehicle with
Attitude Regulation**

꼬리날개 없는 날갯짓 초소형 비행체의
자세조절

2020 년 8 월

서울대학교 대학원

기계항공공학부

류 승 완

Tailless Flapping-wing Micro Aerial Vehicle with Attitude Regulation

SEUNG WAN RYU

Department of Mechanical and Aerospace Engineering
Seoul National University

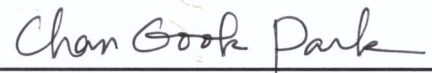
APPROVED:



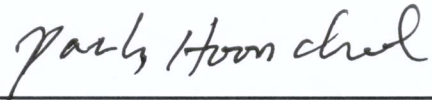
Youdan Kim, Chair, Ph.D.



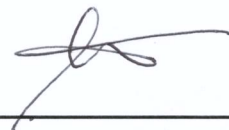
H. Jin Kim, Ph.D.



Chan Gook Park, Ph.D.



Hoon Cheol Park, Ph.D.



Hyeonbeom Lee, Ph.D.

Tailless Flapping-wing Micro Aerial Vehicle with Attitude Regulation

A Dissertation

by

Seungwan Ryu

Presented to the Faculty of the Graduate School of
Seoul National University
in Partial Fulfillment
of the Requirements
for the Degree of

DOCTOR OF PHILOSOPHY

Department of Mechanical and Aerospace Engineering

Seoul National University

Supervisor : Professor H. Jin Kim

AUGUST 2020

to my

MOTHER, FATHER, and SISTERS

and

WIFE

with love.

Abstract

Tailless Flapping-wing Micro Aerial Vehicle with Attitude Regulation

Seungwan Ryu

Department of Mechanical & Aerospace Engineering

The Graduate School

Seoul National University

Flapping wing micro air vehicles (FWMAVs) that generate thrust and lift by flapping their wings are regarded as promising flight vehicles because of their advantages in terms of similar appearance and maneuverability to natural creatures. Reducing weight and air resistance, insect-inspired tailless FWMAVs are an attractive aerial vehicle rather than bird-inspired FWMAVs. However, they are challenging platforms to achieve autonomous flight because they have insufficient control surfaces to secure passive stability and a complicated wing mechanism for generating three-axis control moments simultaneously. In this thesis, as preliminary autonomous flight research, I present the study of an attitude regulation and trajectory tracking control of a tailless FWMAV developed.

For these tasks, I develop my platform, which includes two DC motors for generating thrust to support its weight and servo motors for generating three-axis control moments to regulate its flight attitude. First, I conduct the force and moment measurement experiment to confirm the magnitude and direction of the lift and moment generated from the wing mechanism. From the measurement test, it is confirmed that the wing mechanism generates enough thrust to float the vehicle and control moments for attitude regulation.

Through the dynamic equations in the three-axis direction of the vehicle, a controller for maintaining a stable attitude of the vehicle can be designed. To this end, a dynamic equation related to the rotational motion in the roll, pitch, and yaw axes is derived. Based on the derived dynamic equations, we design a proportional-integral-differential controller (PID) type controller to compensate for the attitude of the vehicle. Besides, we use a multi-loop control structure (inner-

loop: attitude control, outer-loop: position control) to track various trajectories. Simulation results show that the designed controller is effective in regulating the platform's attitude and tracking a trajectory.

To check whether the developed vehicle and the designed controller are operating effectively to regulate its attitude, I design a lightweight gyroscope apparatus using medium-density-fiberboard (MDF) material. The rig is capable of freely rotating in the roll, pitch, and yaw axes. I consider two situations in which each axis is controlled independently, and all axes are controlled simultaneously. In both cases, attitude regulation is properly performed.

Two flight situations are considered for the trajectory tracking experiment. In the first case, a string connects between the ceiling and the top of the platform. In the second case, the helium-filled balloon is connected to the top of the vehicle. In both cases, the platform tracks various types of trajectories well in error by less than 10 cm. Finally, an experiment is conducted to check whether the tailless FWMAV could fly autonomously in place by removing external devices (string, balloon), and the tailless FWMAV flies within 1 m³ space for about 15 seconds..

Keyword : Flapping-wing micro aerial vehicle (FWMAV), tailed FWMAV, tailless FWMAV, attitude regulation, trajectory tracking control.

Student Number : 2015-31002

Table of Contents

	Page
Abstract	iii
Table of Contents	v
List of Figures	viii
List of Tables	xiii
Chapter	
1 Introduction	1
1.1 Background & Motivation	1
1.2 Literature review	3
1.3 Thesis contribution	7
1.4 Thesis outline	8
2 Design of tailless FWMAV	13
2.1 Platform appearance	13
2.2 Flight control system	17
2.3 Principle of actuator mechanism	18
3 Force measurement experiment	28
3.1 Measurement setup	28
3.2 Measurement results	30
4 Dynamics & Controller design	37
4.1 Preliminary	37
4.2 Dynamics & Attitude control	39
4.2.1 Roll direction	41
4.2.2 Pitch direction	43
4.2.3 Yaw direction	45
4.2.4 PID control	47
4.3 Trajectory tracking control	48
5 Attitude regulation experiments	50

5.1	Design of gyroscope testbed	50
5.2	Experimental environment	52
5.3	Roll axis free	53
5.3.1	Simulation	54
5.3.2	Experiment	55
5.4	Pitch axis free	56
5.4.1	Simulation	57
5.4.2	Experiment	58
5.5	Yaw axis free	59
5.5.1	Simulation	59
5.5.2	Experiment	60
5.6	All axes free	60
5.6.1	Simulation	60
5.6.2	Experiment	61
5.7	Design of universal joint testbed & Experiment	64
6	Trajectory tracking	68
6.1	Simulation	68
6.2	Preliminary	69
6.3	Experiment: Tied-to-the-ceiling	70
6.4	Experiment: Hung-to-a-balloon	71
6.5	Summary	72
6.6	Hovering flight	73
7	Conclusion	83
A	Appendix: Wing gearbox	85
A.1	4-bar linkage structure	85
B	Appendix: Disturbance observer (DOB)	87
B.1	DOB controler	87
B.2	Simulation	89
B.2.1	Step input	89
B.2.2	Sinusoid input	91

B.3 Experiment	92
References	95

List of Figures

1.1	Various types of robots. (1st row) conventional robots, (2nd and 3rd rows) biomimetic robots, (1st column) terrestrial robots, (2nd column) aerial robots, (3rd column) aquatic robots; (a) SpotMini [1], (b) Bat Bot [2], (c) Octobot [3], (d) Gecko [4], (e) Robird [5], and (f) SoFi [6].	9
1.2	Examples of tailed FWMAVs; (a) Phoenix [MIT] [15], (b) Robird [Univ. of Twente] [5], (c) DelFly II [Delft] [16], (d) Explorer [Delft] [17], (e) Ours [SNU] [18], (f) H2bird [19], (g) Microbat [Caltech] [20], (h) Smart bird [Festo] [21], and (i) Meta fly [Bionicbird] [22].	10
1.3	Examples of tailless FWMAVs; (a) KU-2017 [39], (b) KU-2019 [45], (c) ULB-2019 [41], (d) Purdue-2019 [44], (e) NUS-2018 [38], and (f) Delft-2018 [40].	11
1.4	Illustration of the wing mechanism of tailless FWMAVs that generate control moments for attitude regulation; (a) [left] pitch moment, [right] yaw moment, (b) [left] pitch moment, [right] yaw moment, (c) [left] pitch moment, [right] yaw moment, and (d) Two forms for generating roll moments.	12
2.1	Flapping-wing gearbox; (a) Configuration of gears and links, (b) Real picture of gearbox.	14
2.2	Movement of wing mechanism; (a) Flapping angle displacement with respect to crank angle during two wing strokes, (b) Trajectory of biplane-wing tip.	15
2.3	Commercially available tailed FWMAV; (a) Top view, (b) Side view, and (c) Biplane-wing structure.	20
2.4	Arrangement of the parts constituting the flight control system; (a) Front view, (b) Upper side view, (c) Side view, and (d) Reverse side view.	21
2.5	Various types of developed FWMAVs; (a) 1 st version (b) 2 nd version, and (c) Final version.	22
2.6	Circuit diagram of the detailed elements of the flight control system; The red line is power, black and blue lines are ground, and yellow and orange lines are signal. .	23

2.7	Pie chart for the weight distribution of developed tailless FWMAV.	24
2.8	Configuration of wing mechanism for rolling motion; (a) The range of motion of gearbox, (b) The principle of generation of the roll moment.	25
2.9	Configuration of wing mechanism for pitching motion; (a) The range of motion of servo motor, (b) The principle of generation of the pitch moment.	26
2.10	Configuration of wing mechanism for yawing motion; (a) The range of motion of servo motor, (b) The principle of generation of the yaw moment.	27
3.1	Experimental set-up for thrust and moment measurements; (a) Schematic diagram for the measurement experiment, (b) Actual experimental environment using a load cell sensor (LRM200), and (c) a force/torque sensor (Nano-17).	32
3.2	Time history of thrust measurement results at 100 percent input to DC motor; (a) During four strokes ([top] raw data, [bottom] filtered data), (b) During two strokes.	33
3.3	Measurement results; (a) DC motor input vs thrust, (b) Wing frequency vs thrust, and (c) Wing frequency vs thrust/power	34
3.4	Measurement results; (a) Normalized pitch command vs thrust, (b) Normalized pitch command vs pitch moment, and (c) Normalized yaw command vs yaw moment.	35
3.5	Battery duration test during 80 seconds with constant 86 % DC motor inputs.	36
4.1	Right-handed cartesian coordinate system of the tailless-FWMAV; (a) Configuration, (b) Actual platform with the cartesian coordinate system.	38
4.2	Free body diagram (FBD) of tailless FWMAV about roll axis.	41
4.3	FBD of tailless FWMAV about pitch axis.	43
4.4	FBD of tailless FWMAV about yaw axis.	45
4.5	Signal flow for the closed-loop feedback control to regulate the attitude of the platform and for trajectory tracking flight. Euler angles are provided by the external system (VICON). (signal-loop and double-loop structure).	49
5.1	Examples of using an external device; (a) [51], (b) [52], (c) [53], (d) [54], (e) [55], (f) [56], and (g) [39].	51

5.2	Designed gyroscope testbed. Most of the frames are made by MDF materials except for the brackets; (a) 3D image by CATIA program, (b) Actual testbed with tailless FWMAV.	52
5.3	Indoor experimental environment; (a) VICON cameras are located on the upper edge of the room, (b) VICON software, and (c) Tailless FWMAV with four reflective markers.	53
5.4	Simulation results of roll angle regulation. Reference angle is +45 degrees. (a) Initial state, (b) The point in time after 7.5, seconds, and (c) Time history graph of roll angle regulation.	54
5.5	Experiment results of roll angle regulation. Captured images at various reference angles; (a) -45, (b) 0, (c) +45, and (d-e) Time history of roll angle and control input of two DC motors.	55
5.6	Simulation results of pitch angle regulation. Reference angle is -45 degrees. (a) Initial state, (b) The point in time after 7.8 seconds, and (c) Time history graph of pitch angle regulation.	56
5.7	Experiment results of pitch angle regulation. Captured images at various reference angles; (a) -45, (b) 0, (c) +45, and (d-e) Time history of pitch angle and control input of pitch servo motor.	57
5.8	Simulation results of yaw angle regulation. Reference angle is -45 degrees. (a) Initial state, (b) The state after 8.1 seconds, and (c) Time history graph of yaw angle regulation.	58
5.9	Experiment results of yaw angle regulation. Captured images at various reference angles; (a) -45, (b) 0, (c) +45, and (d-e) Time history of yaw angle and control input of yaw servo motor.	59
5.10	Hovering situation to regulate all Euler angles; (a) Initial state, (b) The state after 3.23 seconds, (c) The state after 6.29 seconds, and (d) The state after 9.18 seconds.	61
5.11	Without feedback control; (a) Euler angles stay at a non-zero meaningless value, (b) Euler angles vary randomly.	62

5.12	Hovering situation to regulate all Euler angles; (a) Initial state, (b) Hovering state, and (c) Time history of Euler angles and control inputs of DC motors and servo motors.	63
5.13	Time history of measurement results about sinusoid reference angle; (a) The results of roll angle tracking, (b) Pitch angle tracking.	64
5.14	Universal joint testbed for attitude regulation; (a) CAD design of universal joint, (b) View from above, (c) View from side, (d) Initial attitude, (e) Hovering state, and (f) Time history of Euler angles.	66
5.15	Tethered flight environment for trajectory tracking control environment; (a) Tied-to-the-ceiling, (b) Hung-to-a-balloon.	67
6.1	Simulation results of trajectory tracking; (a) Animation of tailless FWMAV, (b) Straight forward trajectory, (c) Circle trajectory, and (d) Number eight shape trajectory.	74
6.2	Tied-to-the-ceiling test: experimental results of moving toward \pm X-direction, (top) Overlaid sequence of snapshots of the platform during the experiment, (bottom-left) Trajectory in XY-plane, and (bottom-right) Time history of the position. . . .	75
6.3	Tied-to-the-ceiling test: experimental results of moving toward \pm Y-direction, (top) Overlaid sequence of snapshots of the platform during the experiment, (bottom-left) Trajectory in XY-plane, and (bottom-right) Time history of the position. . . .	76
6.4	Tied-to-the-ceiling test: experimental results of moving toward square trajectory, (top) Overlaid sequence of snapshots of the platform during the experiment, (bottom-left) Trajectory in XY-plane, and (bottom-right) Time history of the position. . . .	77
6.5	Hung-to-a-balloon test: experimental results of moving toward \pm X-direction, (top) Overlaid sequence of snapshots of the platform during the experiment, (bottom-left) Trajectory in XY-plane, and (bottom-right) Time history of the position. . . .	78
6.6	Hung-to-a-balloon test: experimental results of moving toward \pm Y-direction, (top) Overlaid sequence of snapshots of the platform during the experiment, (bottom-left) Trajectory in XY-plane, and (bottom-right) Time history of the position. . . .	79

6.7	Hung-to-a-balloon test: experimental results of moving toward square trajectory, (top) Overlaid sequence of snapshots of the platform during the experiment, (bottom-left) Trajectory in XY-plane, and (bottom-right) Time history of the position. . . .	80
6.8	Hung-to-a-balloon test: experimental results of moving toward circle trajectory, (top) Overlaid sequence of snapshots of the platform during the experiment, (bottom-left) Trajectory in XY-plane, and (bottom-right) Time history of the position. . . .	81
6.9	Experimental results of hovering flight, (a) Overlaid sequence of snapshots of the platform during the experiment, (b) Time history of the position, (c) Time history of the attitude, and (d) Trajectory in XY-plane.	82
B.1	Disturbance observer (DOB) signal flow.	88
B.2	Block diagram of control-loop; (a) PID, (b) PID+DOB.	89
B.3	Time history of Euler angles based on two types of controllers by step input; (a) PID controller, (b) PID+DOB controllers.	91
B.4	Time history of Euler angles based on two types of controllers by sine input; (a) PID controller, (b) PID+DOB controllers.	92
B.5	Experimental environment for validating DOB-based control structure; (a) Actual experimental environment, (b) Time history of Euler angles in wind disturbance. .	93
B.6	Experimental results for validating DOB-based controller; (a) PID controller, (b) PID+DOB controllers.	94

List of Tables

1.1	Wing kinematic and structural differences of two types of FWMAVs.	3
1.2	Characteristics of tailed FWMAVs.	4
1.3	Characteristics of tailless FWMAVs.	6
1.4	Summary of current status of tailless FWMAVs around the world.	7
2.1	Lengths of links in flapping-wing gearbox.	14
2.2	Geometric and physical specification of the platform.	16
2.3	Details of the components that make up the flight control system.	17
5.1	PID control gains for attitude regulation in two testbeds.	65
6.1	Simulation parameters for trajectory tracking.	69
6.2	Moving toward X-direction; ($V_y = 0$).	70
6.3	Moving toward Y-direction; ($V_x = 0$).	71
6.4	Moving toward square shape.	72
6.5	RMSE of trajectory tracking experiments.	72
A.1	The movement of the links according to the ‘Grashof structure’.	86
B.1	Parameters of the simulation environment.	90
B.2	Parameters of the tailless FWMAV.	90
B.3	Beaufort wing scale.	93

1.1 Background & Motivation

Biomimetic technology, which has recently attracted attention during the last decade, presents a new paradigm for all scientific fields. Analyzing the shape, structure, and behavior of living things, various attempts are being made to apply their strengths to many types of robots to overcome some issues that conventional robots have not solved or to obtain better performance results. For example, a ground robot uses legs instead of wheels, a sea robot uses fins instead of a rudder and a propeller, and an aerial robot uses wings instead of a propeller and jet engine. This is because living things undergo evolutionary processes to draw results in a more effective and efficient direction over a long period. Fig. 1.1 shows various types of biomimetic robots developed according to the environment in which the robots are operated.

Unmanned aerial vehicles (UAVs) are a promising research platform incorporating technology, security issues, and social regulations due to their remarkable applicability. Generally, UAVs can be classified into several groups based on specific criteria such as flight altitude, mission radius, wing types, size of the vehicle, and so on. In terms of size, micro aerial vehicles (MAVs) are a class of miniature UAVs with a dimension restriction. Depending on the wing types, there are three categories, i.e., fixed-wing, rotary-wing, and flapping-wing. Compared to the fixed-wing and the rotary-wing, the study of the flapping-wing aerial vehicles is relatively insufficient [7]. Further,

researchers are trying to apply biomimetic characteristics to MAVs, so intensive research on flapping-wing micro aerial vehicles (FWMAVs) has been carrying out because of their outstanding benefits [8, 9, 10, 11].

FWMAV is a flight vehicle that generates thrust and lift by using multiple wing movements such as flapping, bending, sweeping, and twisting motions. Especially, the platform has several advantages such as better maneuverability, lower power cost and noise, less damage from a collision, and user-friendly shape compared with conventional platforms on a similar scale [12, 13, 14]. In addition, as the name suggests, the platform has biomimetic characteristics and MAV capabilities, so it can perform a specialized task that requires concealment effect in a narrow space. Despite the many advantages, it still has many limitations, including size, weight, and power (Swap) constraints. Therefore, there are still significant challenges to be solved for FWMAV to achieve a fully autonomous flight.

FWMAV is categorized as either a bird-inspired platform or insect-inspired platform based on kinematic and structural differences of wing motion. In the latter case: 1) it has no tail wings, 2) the parts in charge of sensing and actuation of wing converge on wing hinge. 3) the wing inertia is low, 4) the wing frequency is higher, 5) the flapping angle is larger, and 6) the stroke plane is horizontal or nearly horizontal with respect to vertical body fuselage. Due to the above representative characteristics, the insect-inspired platforms are capable of hovering maneuvers, flying at low speed, and changing flight direction rapidly. (Exceptionally, there is a hummingbird inspired platform that has those flight performances). Those flight performances enable the platform to observe a particular place without wandering in the air and to avoid obstacles. Table. 1.1 shows a comparison of the characteristics of two types of FWMAVs.

In the next Section, I discuss what research has been conducted on two types of FWMAVs.

	Bird-inspired FWMAV	Insect-inspired FWMAV
Relative size	Big	Small
Tail wing	O	X
Control moment	Tail wings movement	Wing movement
Wing actuation	Distributed on wing	Converge on wing hinge
Wing inertia	High	Small
Wing frequency	$< 20 \sim 30$ Hz	$20 \sim 30$ Hz $<$
Wing rotation	Low angle	High angle
Stroke plane	(nearly) Vertical	(nearly) Horizontal
Stroke angle	Low amplitude	High amplitude
Maneuver	Glide	Hover

Table 1.1: Wing kinematic and structural differences of two types of FWMAVs.

1.2 Literature review

These days, research on FWMAVs is actively progressing because of their advantage and potential. Among two types of platforms, the development of bird-inspired platforms began earlier than the insect-affected platforms. So, more research has been conducted on the study of flight vehicles that mimic birds [7]. The overall background and concept of tailed FWMAV developed are explained in [8]. Fig. 1.2 shows the developed various types of tailed FWMAVs and Table. 1.2 shows the characteristics of those platforms.

Existing literatures about bird-inspired FWMAVs can be largely separated into four areas, which are structure design, modeling, control, and application. In structure design, [23] explains how to design power-efficient wings of FWMAV. The design procedure of the initial DelFly platform is presented in [24]. In [25], they develop a bird-mimetic up-down and twisting wing drive system based on double-crank linkage structure. The design and fabrication of the wing mechanism with compositive flapping and folding motions are described in [26].

Many nonlinear elements such as aerodynamic components and nonlinear geometric make it difficult to control the FWMAV, so obtaining an appropriate model of the platform is effective to control the vehicle. The importance of getting accurate dynamics is presented in [27], and the

	Mass [grams]	Wingspan [cm]	Wing [#]
Phoenix [15]	400	180	2
Robird [5]	730	112	2
DelFly II [16]	16-17	28	4
Explorer [17]	20	28	4
Ours [18]	18	28	4
H2Bird [19]	13	26.5	4
Microbat [20]	11.5	-	2
SmartBird [21]	450	196	2
MetaFly [22]	10	29	2

Table 1.2: Characteristics of tailed FWMAVs.

system identification of linear aerodynamic models of FWMAV using flight data is shown in [28]. [29] provides black-box linear models of tailed FWMAV using system identification method. A time-varying model and a time-averaged model for forward flight dynamics of an FWMAV are presented in [30].

In the case of control studies, [31] performs closed-loop height regulation using an external camera and custom-made onboard electronics. For the experiment, they only control the main wings for generating thrust with a fixed rudder. [19] attempts passing through window mission in cooperation with the ground station, which estimates heading angle. The effects of periodic tail motion on the longitudinal stability of FWMAV is investigated in [32] and they propose a method to reduce the oscillation of the fuselage caused by the wing motions. The regulation of attitude of a tailed FWMAV to maintain a flight height during hovering is achieved in [33].

Developing suitable algorithms to avoid obstacles and to track the specific target using visual sensors is an important research topic in the application area. [34] collects optical flow information during flight, and they confirm that periodic wing motion makes it difficult to use optical flow for advanced tasks. Although infrared (IR) camera provides less information than a standard camera and the IR information is available only in limited circumstances, [35] obtain satisfactory target tracking results using a sensor from a Wii module. To avoid obstacles during flight, a 4.0 grams onboard stereo vision camera is used in [17]. Although the platform can not send real-time images

to a ground control system (GCS), it completely performs autonomous flight. In [18], a low-cost and light-weight first per view (FPV) camera is used for tracking a target during free flight, and the platform successfully carries out the mission.

Through the miniaturization, weight reduction, and efficiency of sensors, computers, and batteries, the research area about tailless FWMAV is gradually expanding. In general, tailless FWMAVs have several inherent matters due to the structure and wing mechanism of the platform such as 1) it is not possible to largely obtain the effect of additional aerodynamic force because the platform is mainly flying at low speed or hovering maneuver. (it is necessary to generate thrust efficiently and effectively since the only thrust generated by the wing mechanism must support the weight of the platform.), 2) it is an inherently unstable system because it has no tail wings which play an important role in passive stability. (For generating control moments, continuous active control is required in a wing mechanism to regulate flight attitude.), and 3) the vibration produced by wing motions influences on the fuselage behavior of the platform. (A mechanical device or control algorithm that reduces vibration is needed.). Based on the above three points, developing an effective and efficient wing mechanism is the main task in tailless FWMAV research.

From the wing mechanism point of view, tailless FWMAVs can be classified into three groups based on how they generate control moments through the movement of a wing mechanism. In the first group, the platforms in [37, 38] can rotate the leading edge of the wing about the direction perpendicular to the axis of the fuselage, so they can tilt their wing stroke planes. For generating pitch moment, the stroke planes of the left and right wings are tilted in the same direction or tilted in the opposite direction to generate yaw moment. Fig 1.4.(a) shows an example of generating control moment using the corresponding wing mechanism.

In the second group, the platforms in [36, 39, 40, 41] can bend the wing roots of left and right wings while their wing stroke planes remain perpendicular with respect to the axis of the fuselage. The wing roots of both sides are tilted in the same direction to generate pitch moment, and tilted in the opposite direction to generate yaw moment. This type of wing mechanism is called as ‘twist modulation’. An example of generating control moments using the corresponding wing mechanism is shown in Fig 1.4.(b). In [39], a platform capable of active stabilization successfully performed a hovering flight, but sufficient control of the yaw axis is not demonstrated. Stable flights have been presented in [40, 41] through attitude regulation, but trajectory tracking is not specifically

	Mass [gram]	Wingspan [cm]	Wing [#]
Nano humming bird [36]	19	16.5	2
Robotic Hummingbird [37]	62	30.48	2
KU-Beetle [39]	21.4	16	2
Delfy Nimble [40]	28.2	33	4
KUbeetle-S1 [45]	16.4	17	2
Colibri Robotique [41]	23.5	21	2
Purdue Hummingbird [44]	12.1	16.79	2
KUbeetle-S2 [46]	15.8	20	2

Table 1.3: Characteristics of tailless FWMAVs.

mentioned.

In the last group, the platforms in [42, 43, 44] can change the size of the area of stroke plane and move the position of the stroke plane. Fig 1.4.(c) shows an example of generating control moments using the corresponding wing mechanism. In [44], a flight control strategy based on reinforcement learning has been reported with a position tracking experiment using the high power supplied externally.

The above three groups can generate a moment in the direction of the roll axis using two methods. One is 1) using the difference in thrust caused by controlling the frequency of both wings and the other method is 2) moving both side wing roots toward the lateral direction. An example of generating a roll moment using the corresponding methods is shown in Fig 1.4.(d), and Table. 1.3 shows the characteristics of developed tailless platforms.

Table. 1.4 summarizes the results of the study using a tailless FWMAV to regulate an attitude and to track a trajectory. Relatively compared to attitude control studies, trajectory tracking studies have not yet been studied much. So, the research on the fully autonomous flight of the tailless platform is still in a relatively early period.

Platform	Year	Battery	Roll	Pitch	Yaw	Time	XY-plane	Z
Nano humming bird [36]	2012	O	O	O	O	11 min.	-	-
Robotic Hummingbird [37]	2017	O	O	O	O	19 sec.	-	-
KU-Beetle [39]	2017	O	O	O	X	40 sec.	-	-
Delfy Nimble [40]	2018	O	O	O	O	5 min.	-	-
KUbeetle-S1 [45]	2019	O	O	O	O	3 min.	-	-
Colibri Robotique [41]	2019	O	O	O	X	12 sec.	O	X
Purdue Hummingbird [44]	2019	X	O	O	O	-	O	O
KUbeetle-S2 [46]	2020	O	O	O	O	8.8 min.	-	-

Table 1.4: Summary of current status of tailless FWMAVs around the world.

1.3 Thesis contribution

In this thesis, I develop a lightweight (< 30 grams) and a small size ($< 30 \text{ cm}^3$) tailless FWMAV. The flight platform has a wing mechanism that generates thrust and control moments simultaneously using DC motors and servo motors. For the flight control system, I use a single-board microcontroller Arduino Pro Mini to produce control signals to operate each actuator, and the system includes a Bluetooth communication module, so it can communicate wirelessly with a ground station. Our main contribution is as follows:

- I conduct thrust and control moment measurement experiments on the wing mechanism and analysis the measured values with respect to the input of actuators. It has been confirmed that the wing mechanism of a vehicle can generate thrust and control moments necessary for flight.
- I fabricate an experimental apparatus as an assist device for attitude regulation. In addition, an attitude controller based on the derived dynamics is designed. Experimental results show that the possibility of the designed control strategy for attitude regulation in the 3-axis direction.
- I conduct an autonomous tethered flight experiment for tracking a trajectory in tied-to-the ceiling and hung-to-a-balloon environments. Based on the results, hover flight is performed

and our tailless FWMAV flies for 15 seconds with small error variation in 3D position and Euler angles.

1.4 Thesis outline

The remaining sections of this thesis are divided as follows. In Section II, I explain the development processes of tailless FWMAV equipped with a flight control system. The principle of force generation in the wing mechanism is also presented. The experimental process to check the physical quantity of force generated by the wing mechanism, and the corresponding measurement results are described in Section III. I derive the dynamics of the tailless platform and design a controller for attitude regulation and trajectory tracking in Section IV. Section V covers the details of a testbed and shows the simulation and experimental results of attitude regulation. The experimental setup and the results of trajectory tracking are explained in Section VI. Section VII concludes by summarizing the main findings and an outlook on future work. Additional supplement materials are included in Appendix Section.

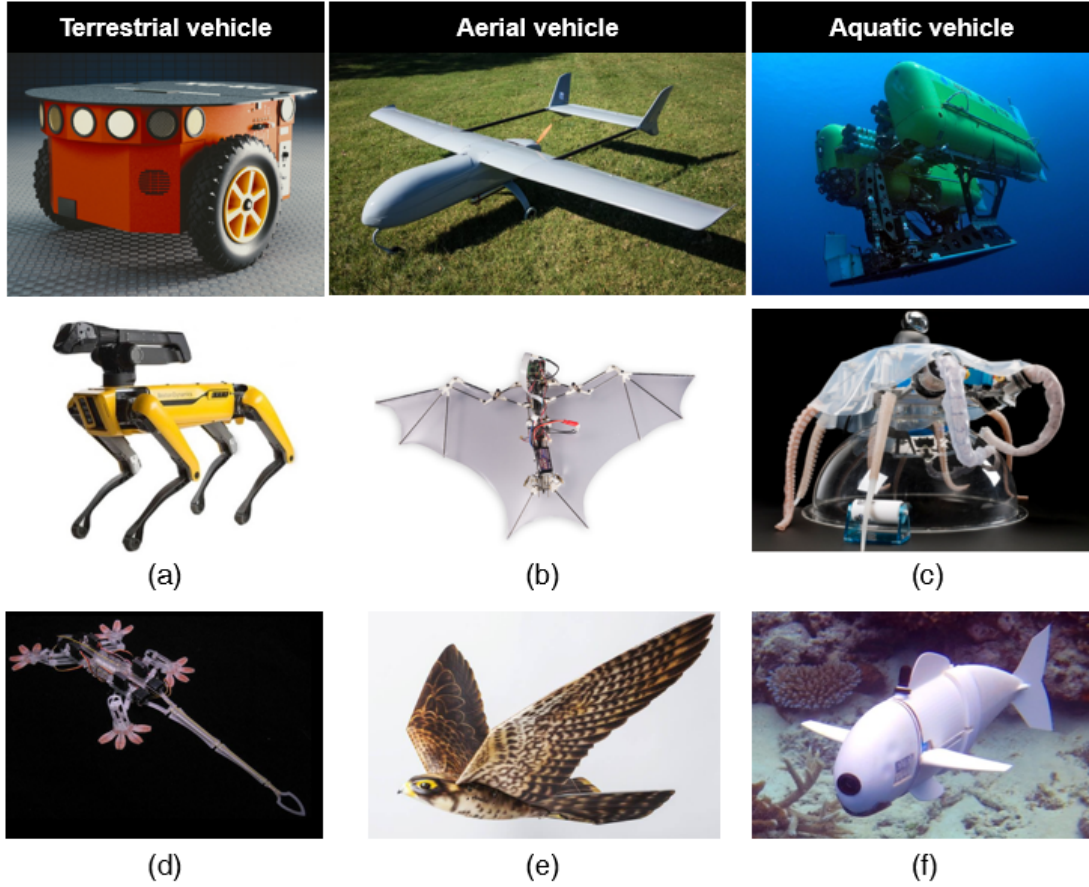


Figure 1.1: Various types of robots. (1st row) conventional robots, (2nd and 3rd rows) biomimetic robots, (1st column) terrestrial robots, (2nd column) aerial robots, (3rd column) aquatic robots; (a) SpotMini [1], (b) Bat Bot [2], (c) Octobot [3], (d) Gecko [4], (e) Robird [5], and (f) SoFi [6].

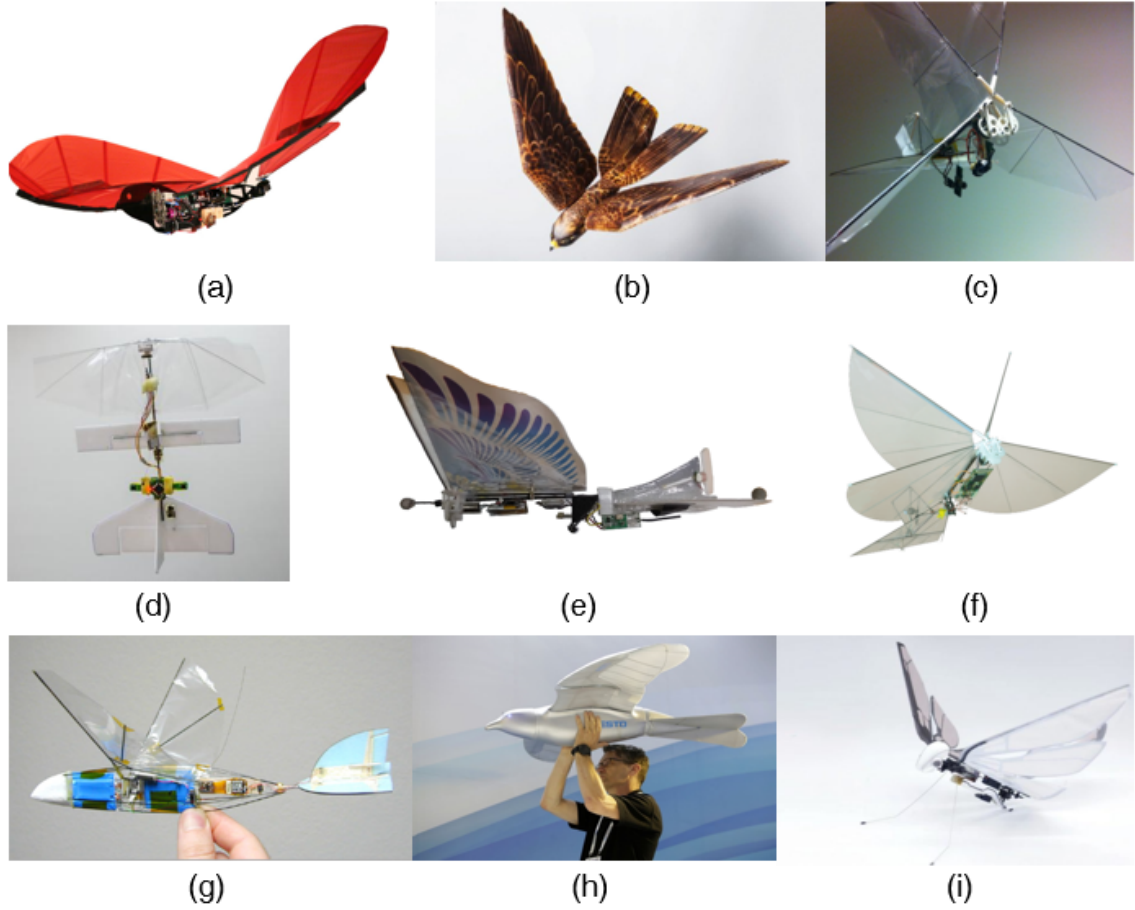


Figure 1.2: Examples of tailed FWMAVs; (a) Phoenix [MIT] [15], (b) Robird [Univ. of Twente] [5], (c) DelFly II [Delft] [16], (d) Explorer [Delft] [17], (e) Ours [SNU] [18], (f) H2bird [19], (g) Microbat [Caltech] [20], (h) Smart bird [Festo] [21], and (i) Meta fly [Bionicbird] [22].

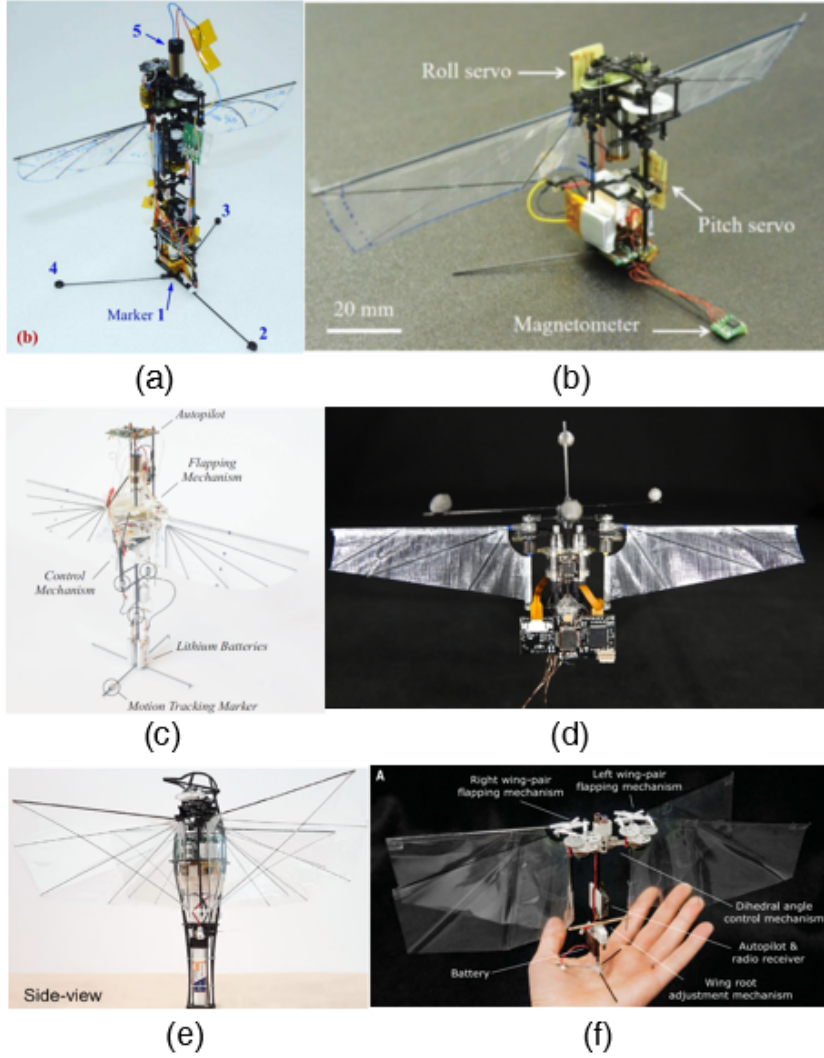


Figure 1.3: Examples of tailless FWMAVs; (a) KU-2017 [39], (b) KU-2019 [45], (c) ULB-2019 [41], (d) Purdue-2019 [44], (e) NUS-2018 [38], and (f) Delft-2018 [40].

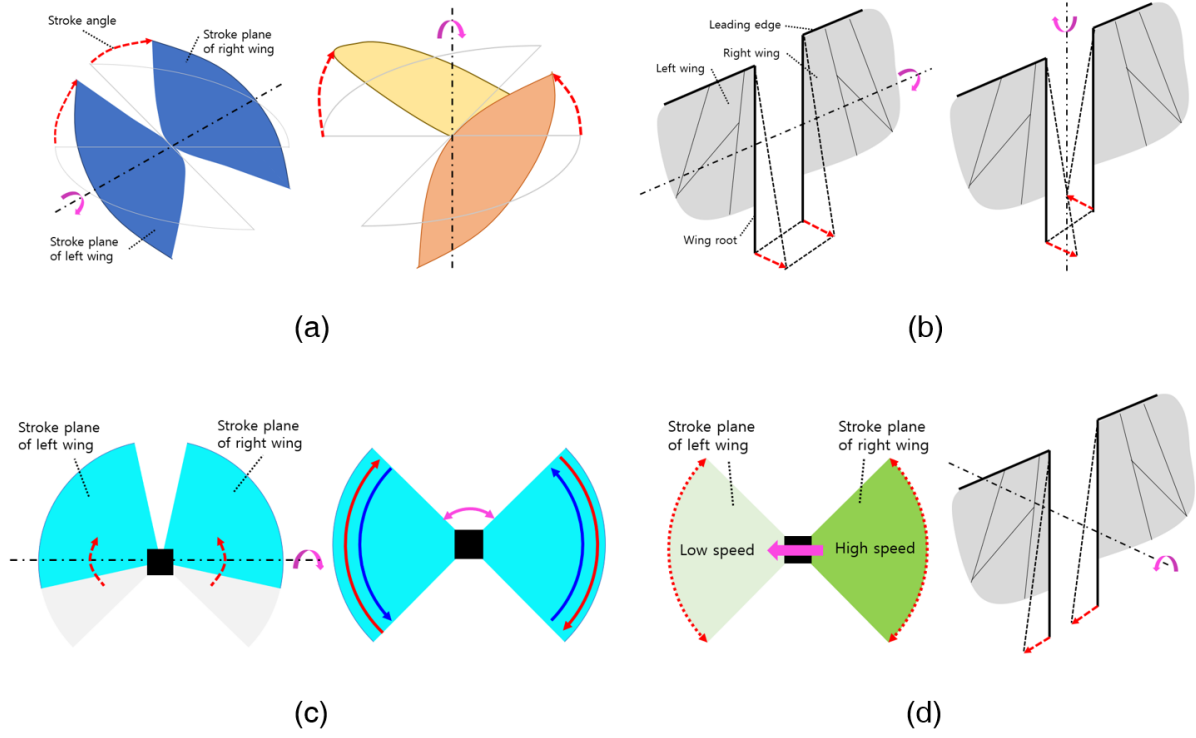


Figure 1.4: Illustration of the wing mechanism of tailless FWMVs that generate control moments for attitude regulation; (a) [left] pitch moment, [right] yaw moment, (b) [left] pitch moment, [right] yaw moment, (c) [left] pitch moment, [right] yaw moment, and (d) Two forms for generating roll moments.

2

Design of tailless FWMAV

In this Section, I explain the fabrication process to make the final version of a tailless FWMAV, and design of the platform. The components to build the flight control system and their functions are also described. In addition, I present the principle of generating the thrust and three-axis moments to regulate flight attitude in a wing mechanism. The geometrical target of the platform to be developed is set to be less than 30 cm^3 in *width* \times *length* \times *height* and the total weight of the platform is set within 30 grams.

2.1 Platform appearance

Fig. 2.3 shows a commercially available RC toy, and it looks like the shape of a pigeon. The main wing of the toy shown in Fig. 2.3. (c) is two pairs of wing structures, unlike the wings of ordinary birds. The carbon rod with a diameter of 0.95 mm is the leading edge of each wing, and wing cover is made of vinyl material. The tail wings are consist of horizontal and vertical wings, and they are made of styrofoam materials. There are elevator control surfaces on the horizontal tail wing and rudder control surface on the vertical tail wing. In the case of the elevators, there are no actuators. Instead, I can bend the control surfaces to a certain angle before a flight, and they keep the initial angle during flight. In the case of the rudder, it is driven by an actuator consisting of a enamel coil and neodymium magnet. Unlike a servo motor, the actuator does not have an

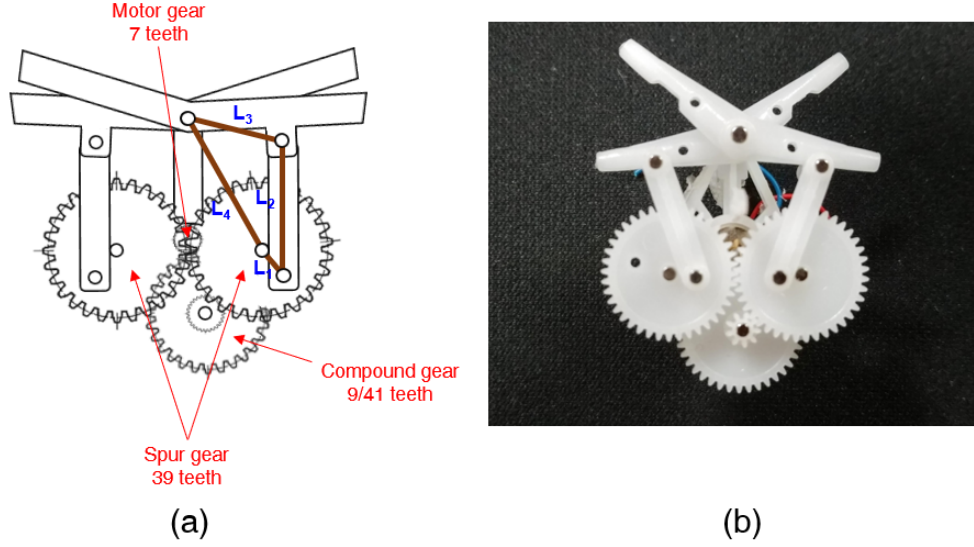


Figure 2.1: Flapping-wing gearbox; (a) Configuration of gears and links, (b) Real picture of gearbox.

	L_1	L_2	L_3	L_4
Length [mm]	3	11	9	14

Table 2.1: Lengths of links in flapping-wing gearbox.

intermediate point in the operating range. That is, it follows the concept of bang-bang control; the rudder control surface moves to the maximum right side, and the maximum left side. The toy has a 2.4 GHz receiver, is capable of flying for about 15 minutes indoor/outdoor environment with a 60 mAh lithium polymer battery and its weight is 15 grams.

Fig. 2.1 shows the wing gearbox of the RC toy which is the core structure of the flapping-wing mechanism. Among several 4-bar linkage structures, the wing gearbox has a crank-rocker structure (crank, coupler, rocker, and ground link), so the rotational movement of the crank link driven by DC motor causes the repetitive motion of rocker link which connects with the leading edge of the wing.

Table 2.1 summarizes lengths of links in the flapping-wing gearbox of RC toy and Fig. 2.2 shows flapping angle displacement with respect to the crank angle, and trajectory of the biplane-

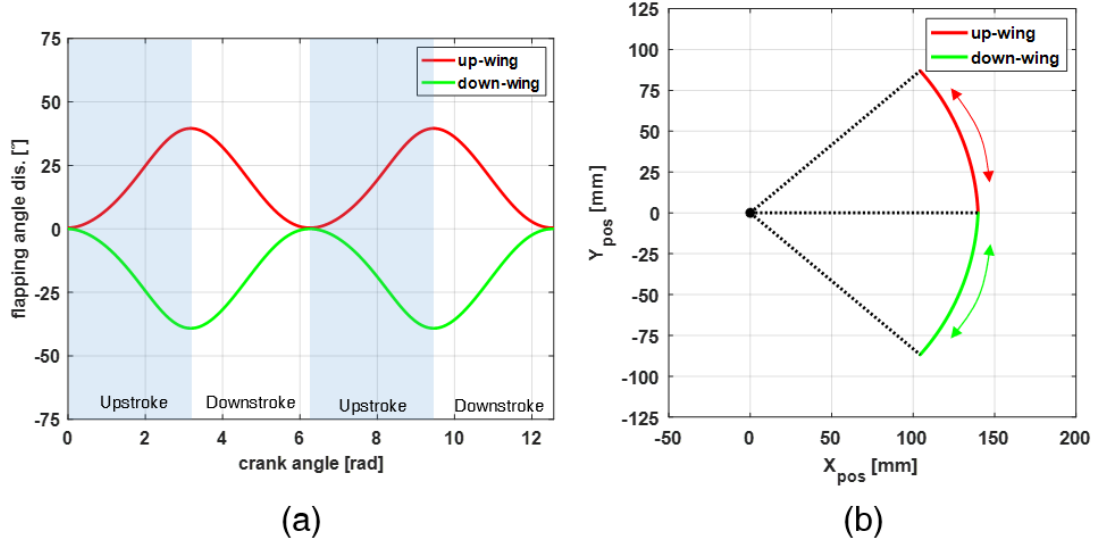


Figure 2.2: Movement of wing mechanism; (a) Flapping angle displacement with respect to crank angle during two wing strokes, (b) Trajectory of biplane-wing tip.

wing tip. Due to the biplane-wing structure, the upper and lower wings move simultaneously depending on the crank angle, and the maximum flapping angle between both wings is about 78 degrees.

Fig 2.5 shows various types of developed tailless FWMAVs. Among several parts of the RC toy, I used the flapping-wing gearbox and the biplane-wing as materials needed for the development of tailless FWMAV. For driving the wing mechanism, two gearboxes are required to move the left and right wings. For wing structure, biplane-wing is cut in half so that the left and right wings are symmetrical in the direction of the fuselage, and the carbon rod corresponding to the leading edge is attached to the left and right gearboxes. Another carbon rod with a diameter of 0.8 mm is called wing root, and the rod is the axis of the flapping motion. The wing root is attached to the section where the wing is cut (to be parallel to the fuselage direction). Let's look at each developed tailless FWMAV in more detail.

In the case of Fig. 2.5.(a), the left and right wing gearboxes are attached to the rotation part of the servo motor. Depending on the movement of the servo motor, the gearbox can be rotated. The end of the left and right wing roots is not connected to each other and the wing root moves

Component	Value	Unit
Body length	14	cm
Body width	10	cm
Body height	3.5	cm
Wing span	28	cm
Wing area	$110 \cdot 2$	cm^2
Flapping angle	78	degree
Flapping frequency (half biplane-wing)	≈ 25	Hz

Table 2.2: Geometric and physical specification of the platform.

independently. Although the stroke planes on the left and right wings can rotate enough, the periodic flapping motion makes a lot of vibration to the driving part of the servo motor, which puts a burden on the durability of the servo motor. Therefore, this wing mechanism is not suitable.

In the case of Fig. 2.5.(b), the left and right wing gearboxes are connected to the medium-density-fiberboard (MDF) link. Each gearbox is secured to the MDF link so that it cannot be rotated. Therefore, the stroke plane is always maintained in the vertical direction of the fuselage axis. The end of the left and right wing roots are connected to the driving part of the linear servo motor. The forward and backward movements of the linear servo motor cause the wing roots to curve. However, the operation range of the servo motor is so small, so this wing mechanism cannot generate enough control moments.

Fig. 2.5.(c) shows the overall appearance of our final experimental platform. Each power-train (=wing gearbox) driven by DC motor is located in left and right sides, and a pair of wings are connected to each power-train. Therefore, the platform has a biplane-wing configuration. The left and right sides power-train are connected to each other through two plastic spur gears and MDF links. A square-shaped carbon rod with a cross-section of 1mm^2 is used as the fuselage of the platform. A servo motor on the top position of the fuselage is attached to one side of the spur gear as coinciding with the rotation axis. Another servo motor is attached to the bottom position of the fuselage, and a transparent plastic plane is affixed to the rotation part of the servo motor. The left and right-wing roots pass through the plastic plane. The details of the assembled platform

Component	Model	Amount [ea]	Mass [grams]
Frame & Wiring	Carbon rod 0.8 mm & Square 1.5 mm	-	4.56
Battery	Turnigy Nano-Tech 160 mAh	1	4.13
Gearbox	RC-toy	2	3.9
DC Motor	6 mm \times 15 mm [57]	2	3.56
Servo motor	HK-5330S [58]	2	2.87
MCU	Arduino Pro Mini 5V	1	2.1
Biplane wing	RC-toy	2	1.8
Motor driver	DRV8838	2	0.8
Bluetooth module	HC-06	1	0.8
Marker	Sphere with a radius of 3.2 mm	4	0.48

Table 2.3: Details of the components that make up the flight control system.

can also be seen in Fig. 2.4. Table. 2.2 shows geometric and physical specification of the platform.

2.2 Flight control system

Fig. 2.4 shows the platform equipped with flight control system viewed from various directions. A micro control unit (MCU), Arduino Pro Mini, 5V version, is used to generate control inputs (pulse width modulation (PWM) signals) for four actuators, i.e., two DC motors and two servos. Each DC motor operates the left and right gearbox, respectively, and the motor driver delivers current continuously to the DC motor. The platform includes a Bluetooth dongle to communicate with GCS through 2.0 protocol. I use a 160 mAh lithium polymer (lipo) battery to power all electric components. In particular, most of the components of the platform are attached as symmetrically as possible to balance the left-right weight to the direction of the fuselage axis. Fig. 2.6 shows the wiring information of the flight control system (FCS) and I use enamel wire with 0.4 mm diameter to reduce weight. Table 2.3 shows the details of the parts in developed tailless FWMAV and Fig. 2.7 shows weight distribution of the platform.

2.3 Principle of actuator mechanism

As mentioned in the previous Section, our platform is equipped with four actuators, i.e., two DC motors and two servo motors. DC motors interact with servo motors for generating thrust that allows the vehicle to float in the air and control moments that regulate flight attitude by changing the magnitude or the direction of the thrust. Especially, DC motors are involved in rotation on the roll axis of the platform, one servo motor attached to the upper position of the fuselage is related in rotation on the pitch axis, and the other servo motor attached to the bottom position of the fuselage is related in rotation on the yaw axis. Let's look at the principle of force generation and the direction of the behavior of the platform in more detail.

The biplane-wing configuration of tailless FWMAV causes clap and fling effect, and the effect is known to give the advantage to thrust generation. Also, the thrust generated by periodic flapping motions enables the platform to float in the air. The difference in the left and right side propulsive forces creates a control moment that causes rotational motion with respect to the roll axis, i.e., If the frequency of left wings is higher than the right wings, the platform rotates clockwise about the x-axis of body coordination and vice versa. The configuration of wing mechanism for rolling motion is shown in Fig. 2.8.

A servo motor on the top position of the fuselage is attached to one spur gear so that the axis of the servo motor coincides with the axis of the spur gear. Then, two spur gears that are in contact can rotate clockwise or counterclockwise direction by the servo motor. From the rotation of the spur gears, MDF rod connecting between the spur gear and the power-train can rotate 55 degrees upward and 55 degrees downward relative to the y-axis of body coordination. If the configuration of two power-trains and MDF rods makes 'V' shape toward the dorsal side, the position where the left and right thrusts are generated is located above the fuselage axis, which causes the platform to nose-down and vice versa. The configuration of wing mechanism for pitching motion is shown in Fig. 2.9.

A servo motor generating yaw moment is directly attached to the bottom position of the fuselage. The transparent plastic plane on the driving part of the servo motor can rotate 50 degrees clockwise and 50 degrees counterclockwise about the fuselage axis. If the plane rotates any direction about the nominal position, the direction of the thrusts on the left and right sides

tilts, which makes the platform rotate around the z-axis of body coordination and vice versa. The configuration of wing mechanism for yawing motion is shown in Fig. 2.10.

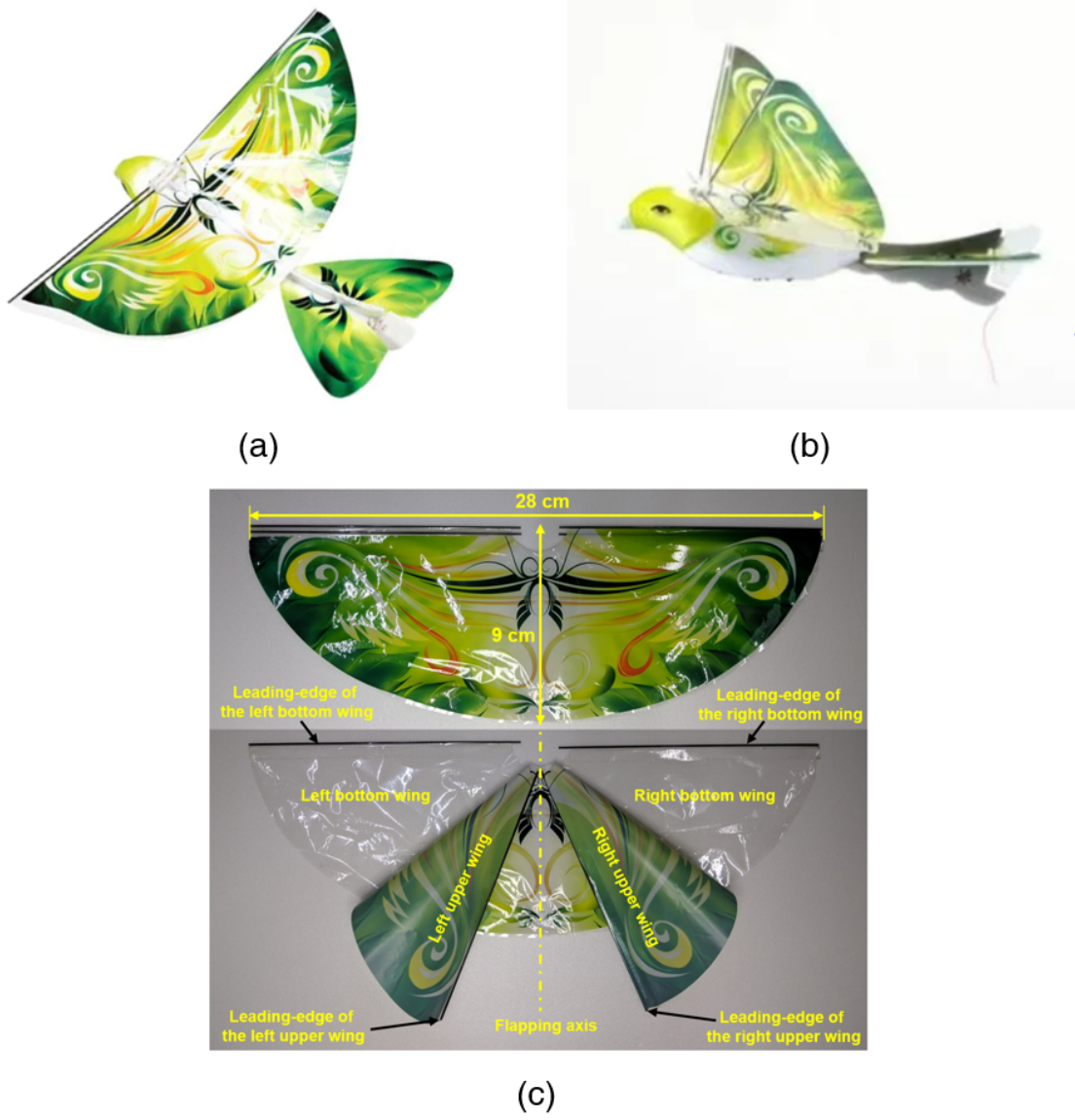


Figure 2.3: Commercially available tailed FWMAV; (a) Top view, (b) Side view, and (c) Biplane-wing structure.

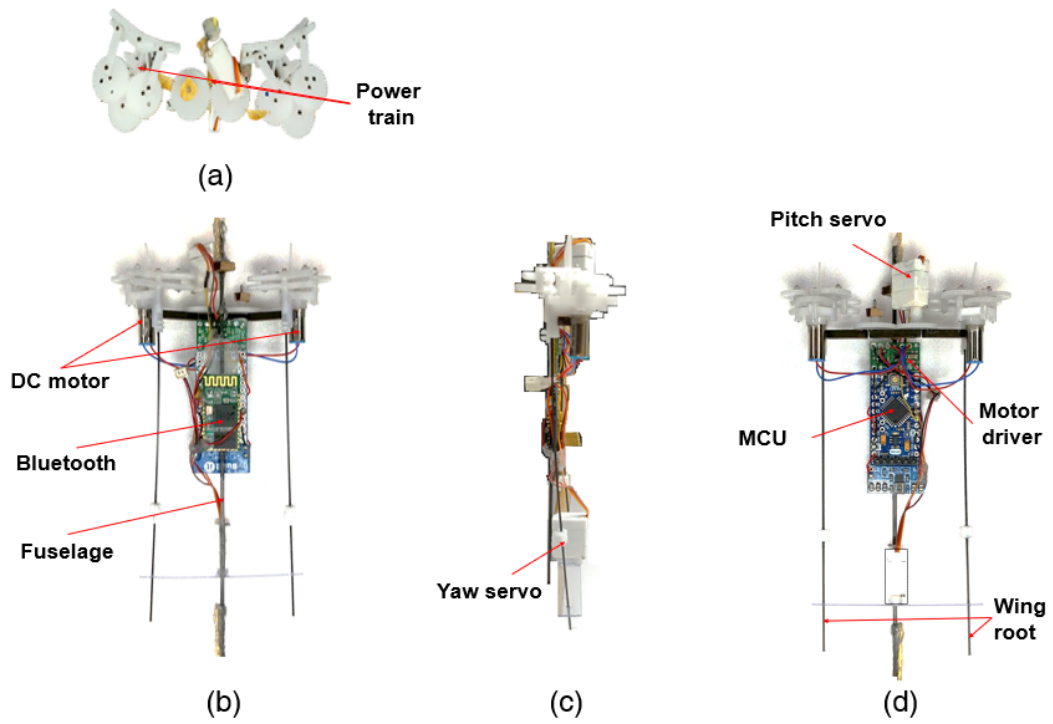
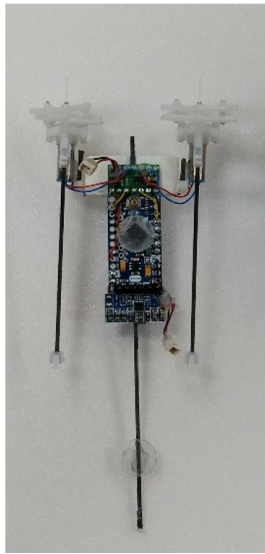
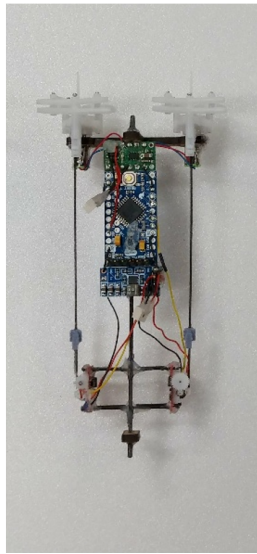


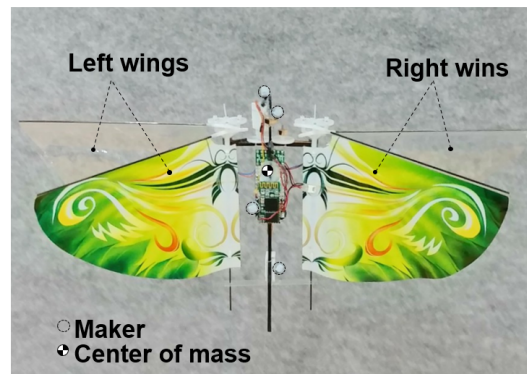
Figure 2.4: Arrangement of the parts constituting the flight control system; (a) Front view, (b) Upper side view, (c) Side view, and (d) Reverse side view.



(a)



(b)



(c)

Figure 2.5: Various types of developed FWMAVs; (a) 1st version (b) 2nd version, and (c) Final version.

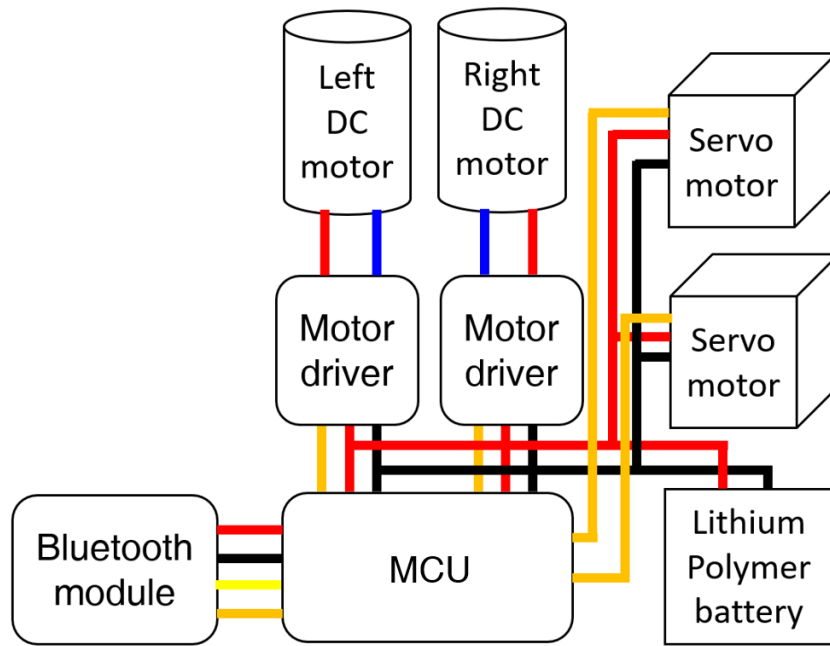


Figure 2.6: Circuit diagram of the detailed elements of the flight control system; The red line is power, black and blue lines are ground, and yellow and orange lines are signal.

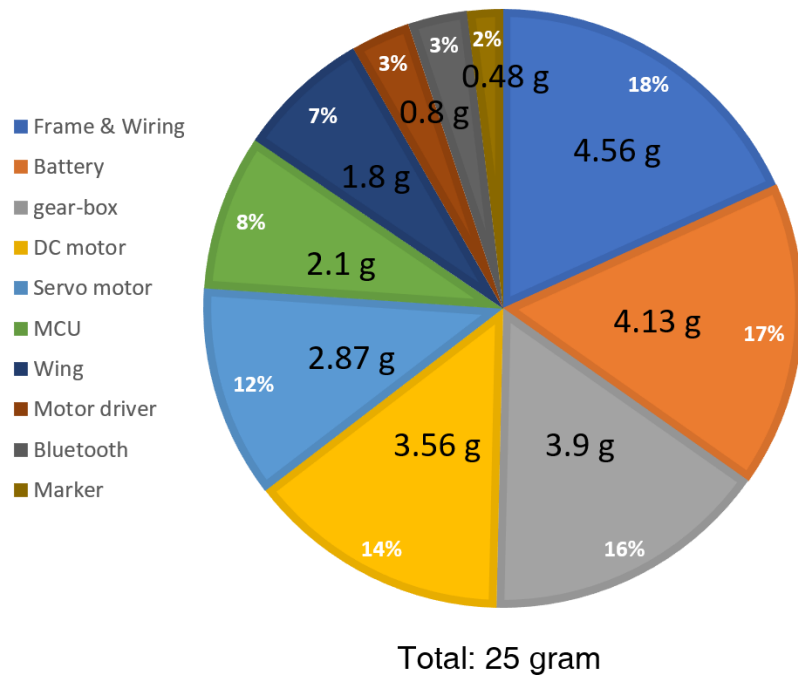


Figure 2.7: Pie chart for the weight distribution of developed tailless FWMAV.

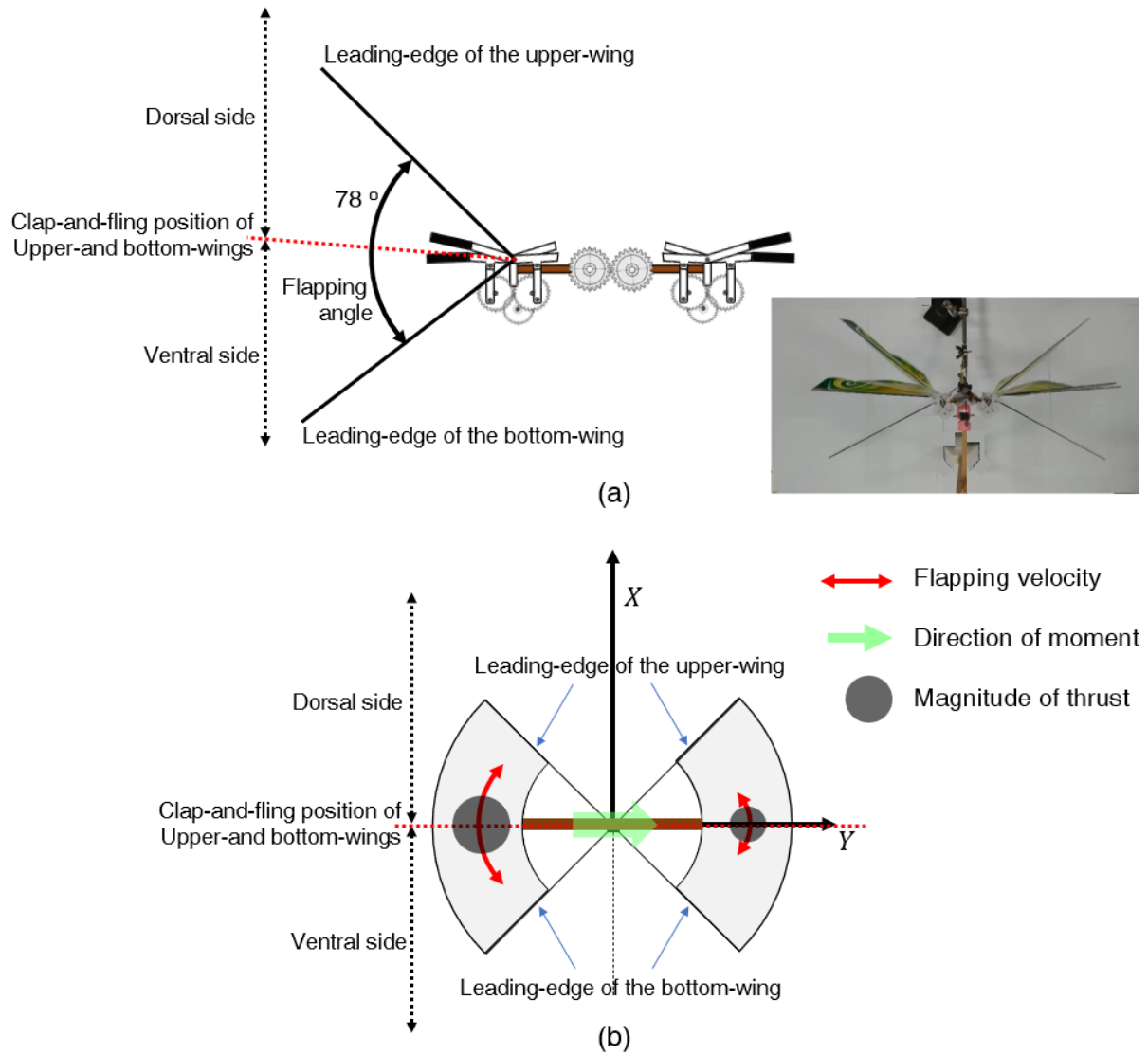


Figure 2.8: Configuration of wing mechanism for rolling motion; (a) The range of motion of gearbox, (b) The principle of generation of the roll moment.

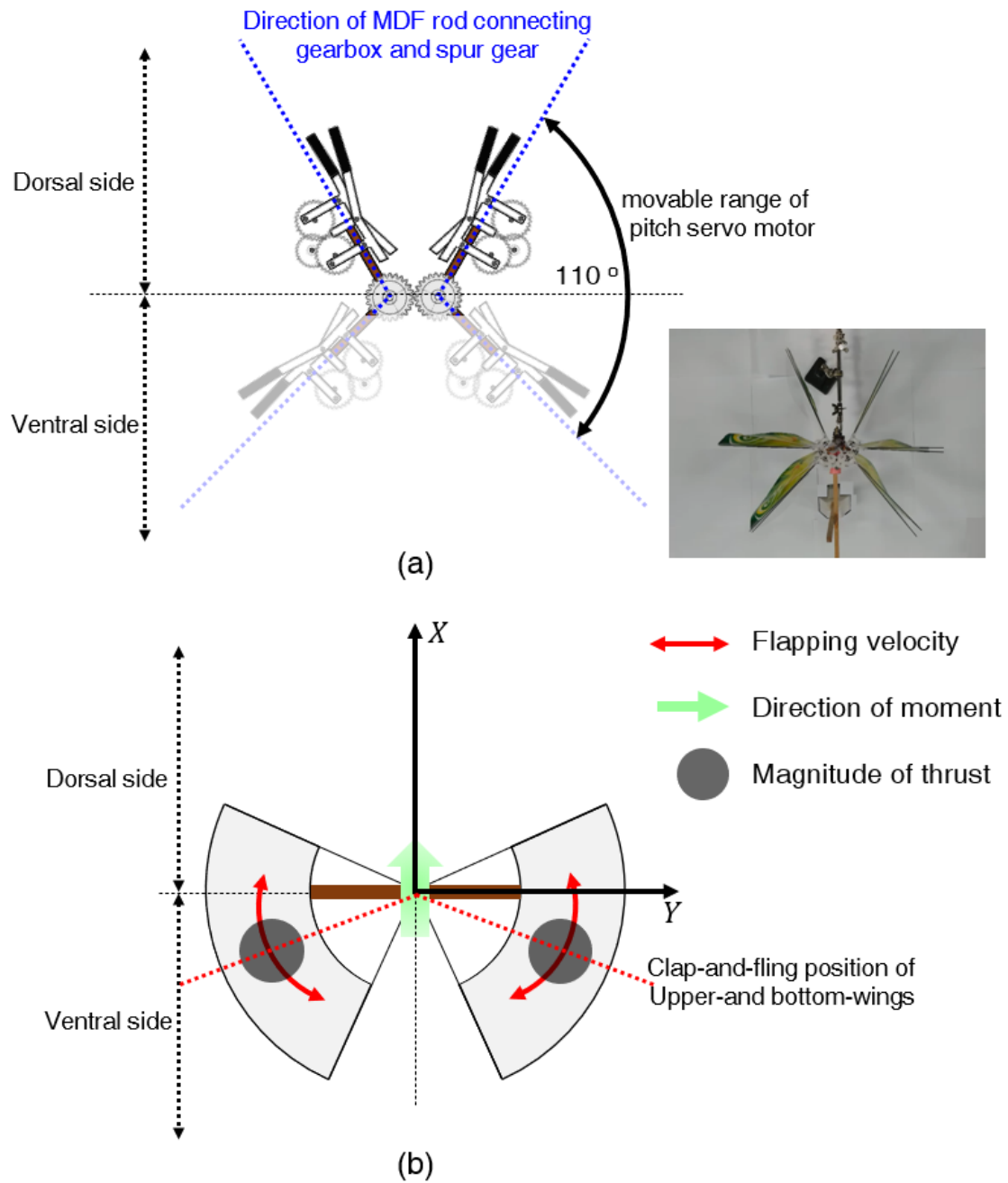


Figure 2.9: Configuration of wing mechanism for pitching motion; (a) The range of motion of servo motor, (b) The principle of generation of the pitch moment.

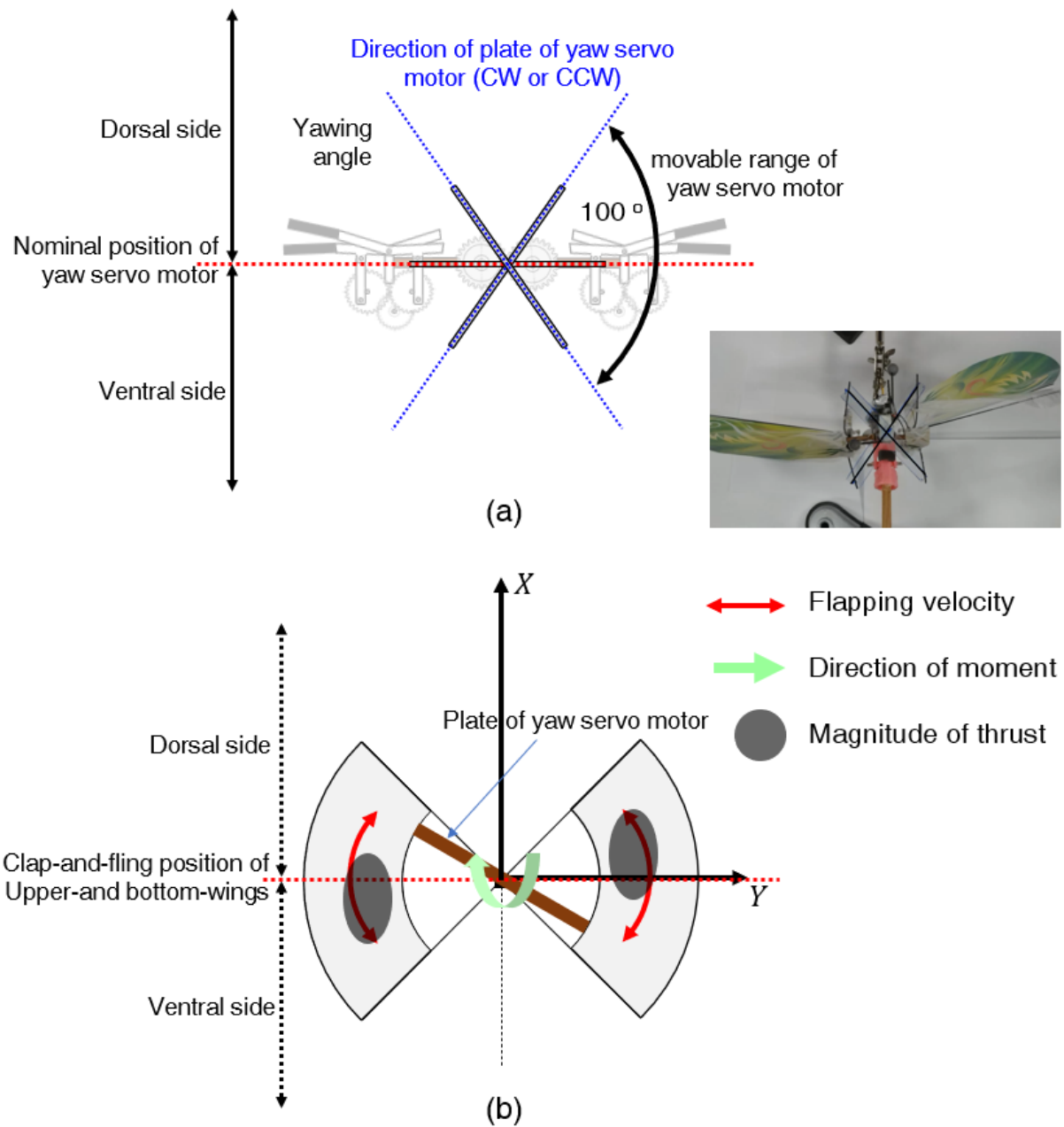


Figure 2.10: Configuration of wing mechanism for yawing motion; (a) The range of motion of servo motor, (b) The principle of generation of the yaw moment.

3

Force measurement experiment

In order to control the attitude of the flight vehicle, quantitative analysis is required to confirm the magnitude and direction of the forces generated by the wing mechanism. In this Section, I explain an experimental setup for measuring the force from the wing mechanism according to the input value of the actuators and analyze the corresponding measurement results. The experimental results of measuring lipo battery duration to estimate flight time are also presented.

3.1 Measurement setup

The weight of the assembled platform including the lipo battery is approximately 25 grams, so sufficient thrust above the weight is required to fly in the air. In addition, the platform should generate enough moments in the 3-axis direction (roll, pitch, and yaw) to compensate for its attitude about various flight maneuvers. To this end, a measurement experiment is conducted to confirm how much thrust and moment are generated in the wing mechanism by the input of actuators.

For this experiment, I design a 3D printed mount that connects the fuselage of the platform and Force & Torque (F/T) sensor. The material of the printed mount is an acrylonitrile butadiene styrene (ABS), so I can prevent the support from absorbing a thrust and moment. The F/T sensor (ATI Industrial Automation - Nano17) used for the experiment can measure all six components

of thrust and moment, and the load cell (FUTEK Advanced Sensor Technology, Inc - LRM200) is also used to measure tension and compression in 1-axis. The high resolution of the sensor and load cell enables accurate measurement of changes in physical quantities with small errors.

Fig. 3.1 shows the experiment environment for the measurement test. One side of the end of the sensor is fixed to the aluminum bracket on the ground, and the module combining the wing mechanism with the 3D printed support is fixed to the other side of the end of the sensor in a direction perpendicular to the ground. An external power supply is used to apply a constant voltage and current to the flight control system. I can upload various PWM signals to operate actuators in MCU and measure corresponding voltage signals generated by the flapping wing motions driven by four actuators. Then, the voltage signals are sent to the ground computer through USB DAQ, and the measured data is saved. The same experiment settings are already employed in [25, 33].

First, assuming that the thrust generated by the left and right wings is the same for the same input, I conduct thrust measurements on only one pair of wings with respect to various inputs of DC motor. I collect data while increasing the inputs of the DC motor at an 8 percent interval from 12 to 100. Second, assuming that the moment in the roll direction is sufficient to generate positive and negative moments by input difference of both DC motors, I conduct moment measurements about pitch and yaw directions, respectively. Second, assuming that the moment in the roll direction is sufficient to generate positive and negative moments by input difference of both DC motors, I conduct moment measurements about pitch and yaw directions, respectively. During the test, 86 percent of the inputs to both DC motors are applied to the wing gearbox. (86 percent of the inputs are for generating thrust corresponding to the weight of the platform, which can be confirmed later in Section 3.2). The rotation part of the yaw servo motor is positioned at the nominal position where the platform does not rotate around the yaw axis while measuring the pitch moment and vice versa.

3.2 Measurement results

For the exact analysis for the collected datasets, I use a low-pass filter (LPF) with a 50 Hz cut-off frequency in order to remove high-frequency noise. 50 Hz is 2.5 times the maximum frequency of the wings and the corresponding value is high enough to capture the characteristics of the periodic wing motion.

Fig. 3.2 shows a thrust graph measured at 100 percent input to DC motor. Generally, the data filtered by LPF has a time delay, So I plot the graph in consideration of the delay factor. In Fig. 3.2.(a), compared to raw data, the filtered data show a smooth curve. A thrust graph measured during two wing strokes at 100 percent input to DC moto is shown in Fig. 3.2.(b). In the graph, there are two peaks. The first peak is a pattern that occurs when the upper and lower wings of the same side meet, and the second peak occurs when the left and right wings are close. Two peaks in one stroke are due to the use of biplane-wing structure. This phenomenon increases the thrust during flapping motion and it is called as a clap-and-fling effect.

Fig. 3.3 shows measurement data related to thrust and wing frequency. To plot the graphs, I measure a thrust while increasing the input of the DC motor from 12 to 100 in 8 percent increments. So, there are a total of 12 experimental groups. The thrust is measured three times per group, and it is measured for 20 seconds at one time. I use the second-order Fourier series to estimate a wing frequency through measured data for 20 seconds because all data have periodic characteristics caused by wing motion. In the case of power, it is calculated by multiplying voltage and current. In Figs. 3.3.(a) and (b), the thrust is proportional to the input of the DC motor and wing frequency. To generate a thrust equal to the weight of the platform, 86 percent of inputs are applied to both DC motors. The value of thrust divided by power is the efficiency of flapping motion, and the factor is also proportional to the frequency of the wing. This result is shown in Fig. 3.3.(c).

When collecting datasets for measuring control moment, the moment is measured three times per each case, and it is measured for 20 seconds at one time. The average value is regarded as the final control moment.

Fig. 3.4 shows the result of pitch moment, yaw moment, and thrust about the normalized position of each actuator. During each test, only 86 percent of inputs are applied to both DC

motors. In Fig. 3.4.(a), regardless of the yaw command, there is a linear relationship between pitch moment and pitch command, and the pitch moment is point symmetry from the nominal position of the pitch servo. This phenomenon is similarly observed in Fig. 3.4.(b). From the measurement results, I can conclude that the use of positive and negative moments allows the platform to rotate sufficiently clockwise and counterclockwise direction with respect to the pitch and yaw axes. The magnitude of thrust is almost constant regardless of the command of pitch and yaw servos, and this result is shown in Fig. 3.4.(c). Based on the results of the control moment measurement, since it can be said that the roll, pitch, and yaw axes are not significantly coupled, independent controllers can be designed for each axis.

The characteristics of a typical secondary battery discharge graph show a sharp change in slope in an initial short period, followed by a gentle slope over some time and then a sharp change in slope again when the battery approaches the point of discharge. Therefore, it is important to use a lipo battery considering the characteristics of voltage drop.

The motor is degraded by heat and voltage drop, which makes thrust generation difficult and has a bad effect on flight performance. So, consistently creating a constant thrust is a necessary factor for a stable flight. An experiment is conducted to measure what type of thrust is produced over time under the condition that a constant input is applied to DC motors using a battery used for actual flight. Fig 3.5 shows a graph of the change in thrust over time. Given that the weight of the platform is 25 grams, it can generate a thrust above its weight for about 40 seconds. However, since no other actuators and communication module are used when measuring a thrust, it is expected to fly for a much shorter time during actual flight.

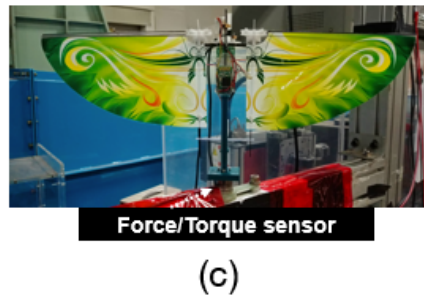
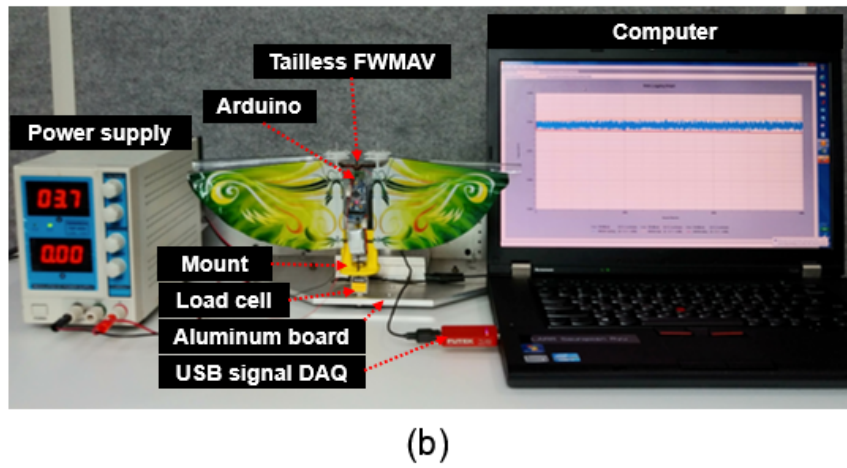
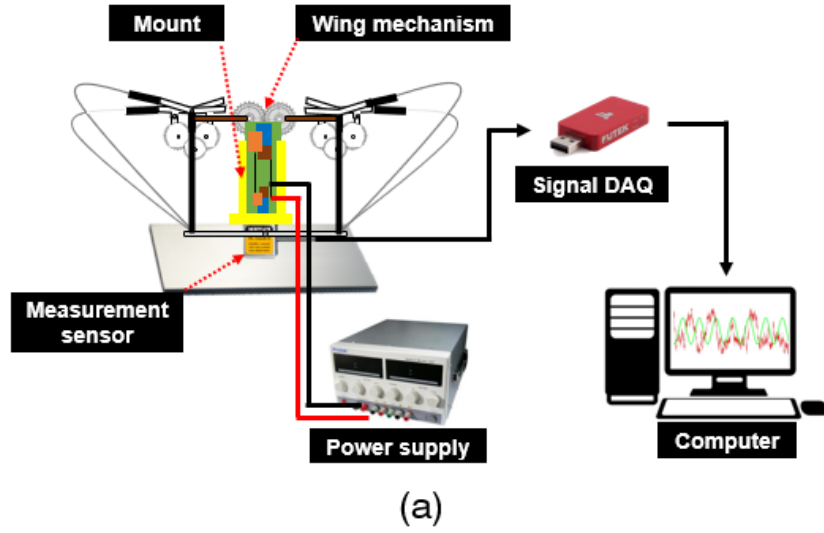
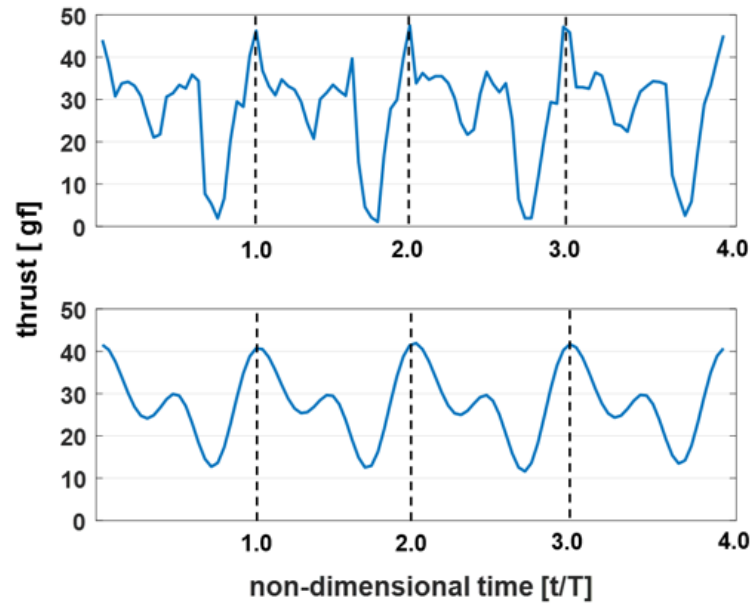
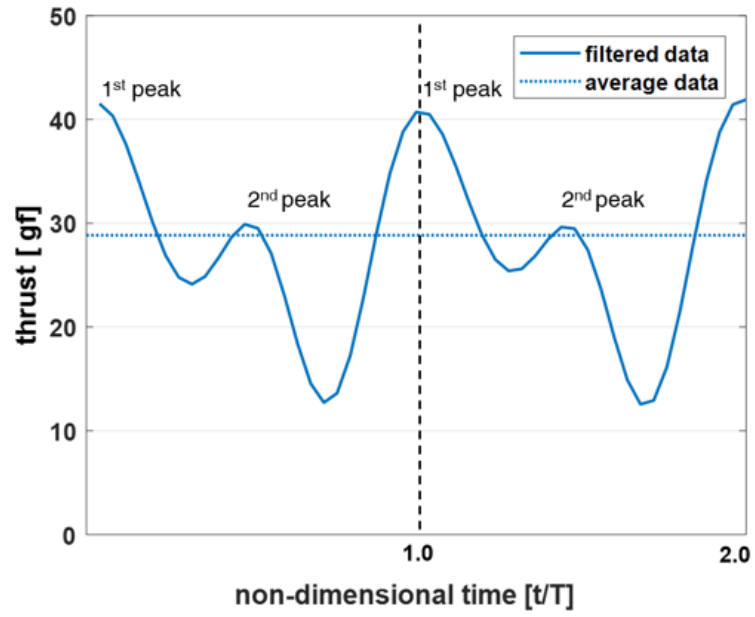


Figure 3.1: Experimental set-up for thrust and moment measurements; (a) Schematic diagram for the measurement experiment, (b) Actual experimental environment using a load cell sensor (LRM200), and (c) a force/torque sensor (Nano-17).

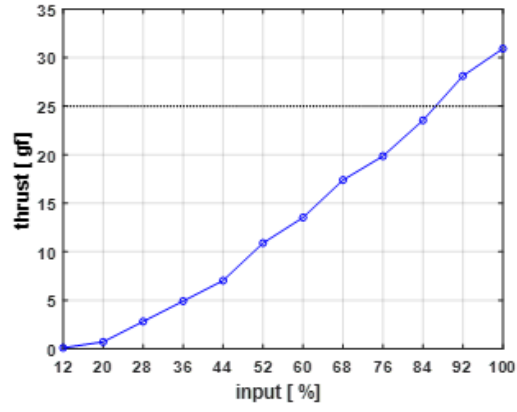


(a)

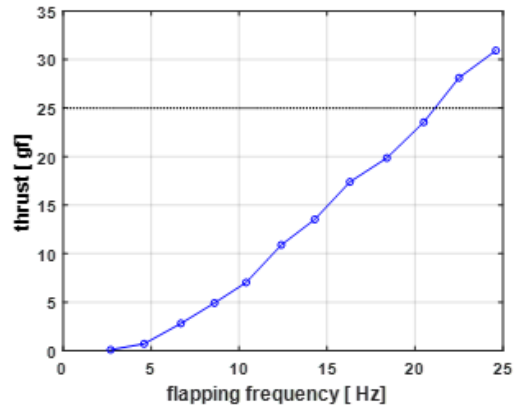


(b)

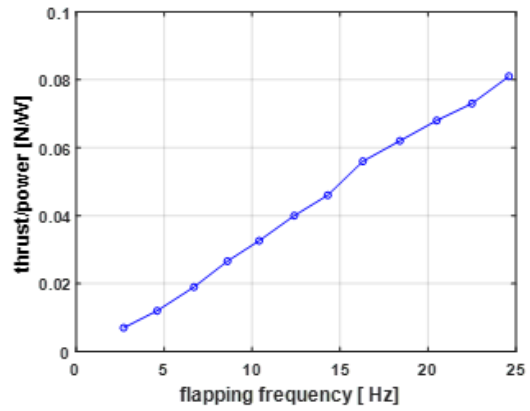
Figure 3.2: Time history of thrust measurement results at 100 percent input to DC motor; (a) During four strokes ([top] raw data, [bottom] filtered data), (b) During two strokes.



(a)

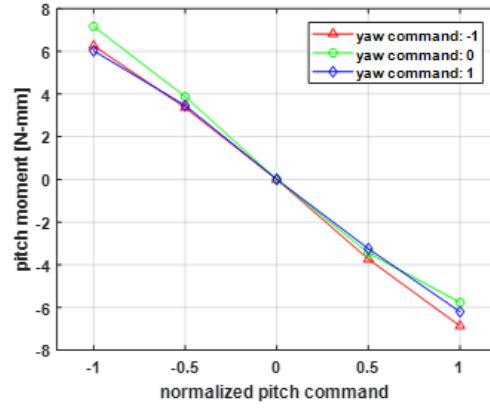


(b)

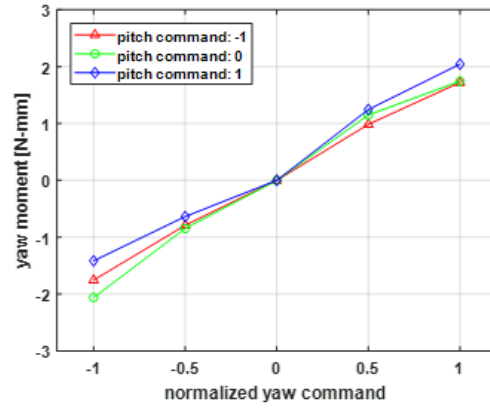


(c)

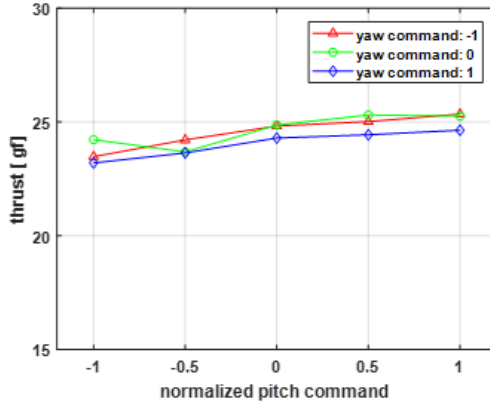
Figure 3.3: Measurement results; (a) DC motor input vs thrust, (b) Wing frequency vs thrust, and (c) Wing frequency vs thrust/power



(a)



(b)



(c)

Figure 3.4: Measurement results; (a) Normalized pitch command vs thrust, (b) Normalized pitch command vs pitch moment, and (c) Normalized yaw command vs yaw moment.

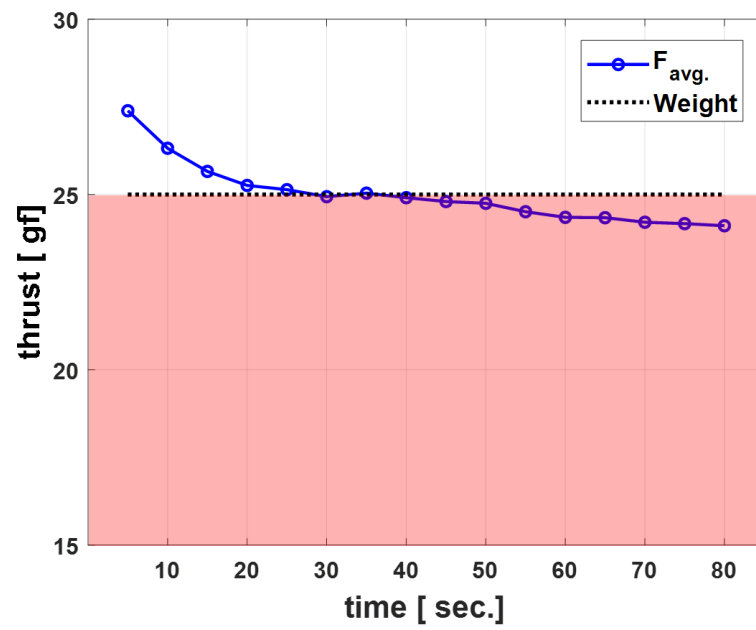


Figure 3.5: Battery duration test during 80 seconds with constant 86 % DC motor inputs.

4

Dynamics & Controller design

In this Section, I explain the process of deriving the model dynamics of tailless FWMAV. Based on the obtained model dynamics, the attitude controller and trajectory tracking controller are designed.

4.1 Preliminary

I estimate the states of an FWMAV during the flight as follows. The coordinates of the four markers are transformed from reference frame (x, y, z) of VICON space to body frame (x_b, y_b, z_b) of the FWMAV, as showed in Fig. 4.1. The unit vectors of the body frame and the reference frame are related to the respective entries of the 3-2-1 rotation matrix sequence described in Eq. (4.1) which is one of the most widely used parameterisations. Before proceeding further, let us use the shorthand notation $S_\psi \equiv \sin \psi$, $C_\psi \equiv \cos \psi$, $S_\phi \equiv \sin \phi$, $C_\phi \equiv \cos \phi$.

$$R_{bi} = \begin{bmatrix} C_\theta C_\psi & -C_\theta S_\psi & S_\theta \\ C_\psi S_\phi S_\theta + C_\phi S_\psi & C_\phi C_\psi - S_\phi S_\theta S_\psi & -C_\theta S_\phi \\ -C_\phi C_\psi S_\theta + S_\phi S_\psi & C_\psi S_\phi + C_\phi S_\theta S_\psi & C_\phi C_\theta \end{bmatrix} \quad (4.1)$$

The absolute velocity $(\dot{x}, \dot{y}, \dot{z})$ and the Euler rates $(\dot{\phi}, \dot{\theta}, \dot{\psi})$ are calculated by differentiating the positions and the Euler angles with respect to time using 1st derivative centered-difference.

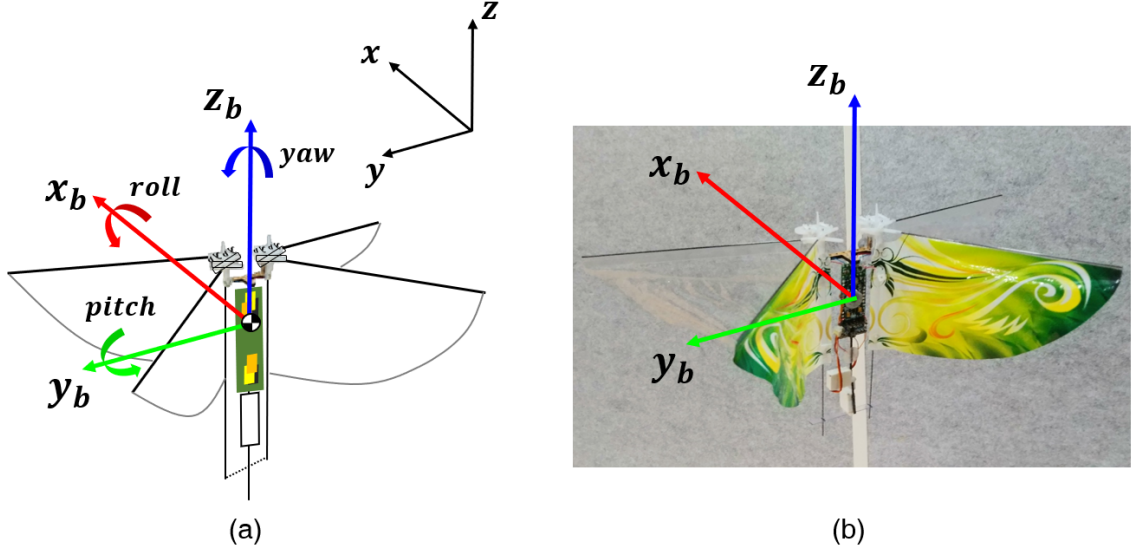


Figure 4.1: Right-handed cartesian coordinate system of the tailless-FWMAV; (a) Configuration, (b) Actual platform with the cartesian coordinate system.

I can determine the relationship between the angular velocities in the body frame (p, q, r) and the Euler rates $(\dot{\phi}, \dot{\theta}, \dot{\psi})$ from Eq. (4.2).

$$\begin{bmatrix} p \\ q \\ r \end{bmatrix} = \begin{bmatrix} 1 & 0 & -S_\theta \\ 0 & C_\phi & C_\theta S_\phi \\ 0 & -S_\phi & C_\theta C_\phi \end{bmatrix} \begin{bmatrix} \dot{\phi} \\ \dot{\theta} \\ \dot{\psi} \end{bmatrix} \quad (4.2)$$

The total 15 states are recalculated: velocity in inertial coordinate $\vec{V}_i = (\dot{x}, \dot{y}, \dot{z})$; velocity in body coordinate $\vec{V}_b = (u, v, w)$; Euler angles (ϕ, θ, ψ) ; Euler rates $(\dot{\phi}, \dot{\theta}, \dot{\psi})$ and angular velocities $\vec{w} = (p, q, r)$.

4.2 Dynamics & Attitude control

I can drive the rigid body equations of motion using Newton's second law based on [47]. The summation of all external forces acting on a body is equal to the time rate of change of the momentum of body and the summation of the external moments acting on the body is equal to the time rate of change of the moment of momentum. Then, Newton's second law can be written in the following equations:

$$\begin{aligned}\frac{d}{dt}(m\mathbf{v}) &= \Sigma\mathbf{F} \\ \frac{d}{dt}\mathbf{H} &= \Sigma\mathbf{M}\end{aligned}\tag{4.3}$$

By assuming that the platform is a rigid body, the motion equation of the rigid body can be expressed with the force and moment act on the center of gravity.

$$\begin{bmatrix} m\mathbf{I} & 0 \\ 0 & I_b \end{bmatrix} \begin{bmatrix} \dot{v}_b \\ \dot{\omega}_b \end{bmatrix} + \begin{bmatrix} \omega_b \times mv_b \\ \omega_b \times I_b \end{bmatrix} = \begin{bmatrix} \Sigma\mathbf{F} \\ \Sigma\mathbf{M} \end{bmatrix}\tag{4.4}$$

where m is the mass, I_b is the body inertia matrix, \mathbf{I} is the identify matrix, and v_b and ω_b ($= p\mathbf{i} + q\mathbf{j} + r\mathbf{k}$) are the linear and angular velocity in body. The scalar equations for the moment of momentum is given by

$$\begin{aligned}H_x &= pI_x - qI_{xy} - rI_{xz} \\ H_y &= -pI_{xy} + qI_y - rI_{yz} \\ H_z &= -pI_{xz} - qI_{yz} + rI_z\end{aligned}\tag{4.5}$$

The mass moments of inertia of the body frame are written as I_x , I_y , and I_z . I_{**} is called the products of inertia. The derivative of a vector \mathbf{X} with respect to rotating body frame having an angular velocity ω_b can be written

$$\left. \frac{d\mathbf{X}}{dt} \right|_I = \left. \frac{d\mathbf{X}}{dt} \right|_B + \omega_b \times \mathbf{X}\tag{4.6}$$

where the subscript I refer to the inertial frame and B means the body fixed frames. Using the identity to the equations of rotation motion,

$$\begin{aligned}
\dot{p}I_x - \dot{q}I_{xy} - \dot{r}I_{xz} - pqI_{xz} + rpI_{xy} + qr(I_z - I_y) + I_{yz}(r^2 - q^2) &= M_x \\
-\dot{p}I_{xy} + \dot{q}I_y - \dot{r}I_{yz} - rqI_{xy} + pqI_{yz} + rp(I_x - I_z) + I_{xz}(p^2 - r^2) &= M_y \\
-\dot{p}I_{xz} - \dot{q}I_{yz} + \dot{r}I_z - prI_{yz} + qrI_{xz} + pq(I_y - I_x) + I_{xy}(q^2 - p^2) &= M_z
\end{aligned} \tag{4.7}$$

I can make the products of inertia $I_{xy} = I_{yz} = I_{zx} = 0$ by proper positioning of the body axis system. Then, the Eq. (4.7) can be written as

$$\begin{aligned}
\dot{p}I_x + qr(I_z - I_y) &= M_x \\
\dot{q}I_y + rp(I_x - I_z) &= M_y \\
\dot{r}I_z + pq(I_y - I_x) &= M_z
\end{aligned} \tag{4.8}$$

By assuming that all axes are decoupled,

$$\begin{aligned}
\dot{p}I_x &= M_x \\
\dot{q}I_y &= M_y \\
\dot{r}I_z &= M_z
\end{aligned} \tag{4.9}$$

The components of the moment acting on the platform are composed of

$$M_{x,y,z} = M_a + M_d + M_g \tag{4.10}$$

where M_a is aerodynamic torques, M_d is rotational damping, and M_g is gravitational torques. M_d is negligible relative to aerodynamic forces even during rapid body rotation and can therefore be neglected from [48, 49]. M_g acts on the COM, so it can be seen as zero. Then, Eq. (4.9) can be expressed as

$$\begin{aligned}
\dot{p}I_x &= M_{a_x} \\
\dot{q}I_y &= M_{a_y} \\
\dot{r}I_z &= M_{a_z}
\end{aligned} \tag{4.11}$$

If flight vehicle is flying near hovering conditions, p, q, r are regarded as ϕ, θ, ψ , respectively.

4.2.1 Roll direction

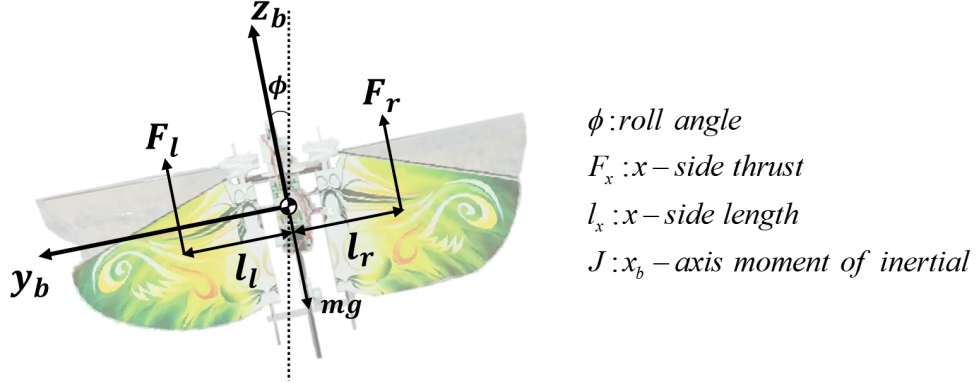


Figure 4.2: Free body diagram (FBD) of tailless FWMAV about roll axis.

Based on the free body diagram (FBD) in Fig 4.2, the working torques by thrusts from the left and right wings are applied to COM of the vehicle. Applying the Newton's second law, the rotation dynamics about roll axis of tailless FWMAV can be simplified to

$$\begin{aligned} J\ddot{\phi} &= F_r l_r - F_l l_l, \quad \text{let } (l_r = l_l = l) \\ \ddot{\phi} &= \frac{l}{J}(F_r - F_l) \end{aligned} \quad (4.12)$$

Let's define system states for the tailless FWMAV as follows:

$$x_1 = \phi, \quad x_2 = \dot{\phi} \quad (4.13)$$

Then, Lyapunov candidate function is represented by the following equations:

$$V(\mathbf{X}) = \frac{1}{2}x_1^2 + \frac{1}{2}x_2^2 \quad (4.14)$$

Derivating Eq. (4.14) with respect to time,

$$\begin{aligned} \dot{V} &= x_1 \dot{x}_1 + x_2 \dot{x}_2 = x_2 \left(x_1 + \frac{l}{J}(F_r - F_l) \right) \quad \text{let } F_r - F_l = -\frac{J}{l}x_1 - \alpha x_2 \\ &= -\frac{l}{J}\alpha x_2^2 \leq 0 \end{aligned} \quad (4.15)$$

With $\alpha > 0$, derivative of V is negative semi-definite for any x_1 and x_2 , so the origin of the system is stable by the *Theorem*.

Theorem: The origin of a system is stable if there is a continuously differentiable positive definite function $V(x)$ so that \dot{V} is negative semi-definite, and it is asymptotically stable if \dot{V} is negative definite [50].

From Eqs. (4.12) and (4.13), closed-loop dynamics is given by

$$\begin{aligned} \dot{x}_1 &= x_2 \\ \dot{x}_2 &= -x_1 - \frac{l}{J}\alpha x_2 \end{aligned} \quad (4.16)$$

In Eq. (4.16), $\dot{V} = 0$ is achieved by $x_2 = 0$ and $x_2 = 0$ means $x_1 = 0$. So, $\dot{V} = 0$ is only achieved at the origin, i.e., $x_1 = 0$ and $x_2 = 0$. By Lasalle's invariance principle, the closed-loop system is asymptotically stable.

From an equilibrium equation between thrusts and the weight of the platform, and Eq. (4.15),

$$\begin{aligned} F_r \cos \phi + F_l \cos \phi &= mg \\ F_r - F_l &= -\frac{J}{l}x_1 - \alpha x_2 \end{aligned} \quad (4.17)$$

I can calculate F_r and F_l as follows:

$$\begin{aligned} F_l &= \frac{mg}{2 \cos \phi} + \frac{J}{2l}\dot{\phi} + \frac{\alpha \dot{\phi}}{2} \\ F_r &= \frac{mg}{2 \cos \phi} - \frac{J}{2l}\dot{\phi} - \frac{\alpha \dot{\phi}}{2} \end{aligned} \quad (4.18)$$

Based on the measurement results of Section 3.2, the actuator inputs that apply to both DC motors are calculated as follows:

$$\begin{aligned} F_{r,l} &= 0.02f_{r,l}^2 + 0.78f_{r,l} - 3.1 \\ f_{r,l} &= 0.24u_{roll} - 0.38 \end{aligned} \quad (4.19)$$

where $f_{r,l}$ is wing frequency and u_{roll} is the input of DC motor.

4.2.2 Pitch direction

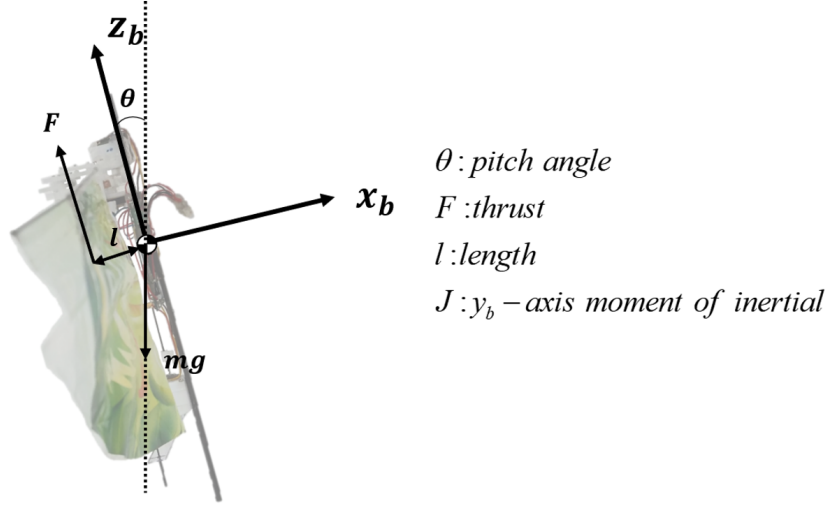


Figure 4.3: FBD of tailless FWMAV about pitch axis.

Based on the free body diagram (FBD) in Fig 4.3, the working torques by thrusts from the left and right wings are applied to COM of the vehicle. Applying the Newton's second law, the rotation dynamics about pitch axis of tailless FWMAV can be simplified to

$$\begin{aligned}
 J\ddot{\theta} &= -Fl \quad \text{let } (F = \frac{mg}{\cos \theta}) \\
 \ddot{\theta} &= -\frac{l}{J} \frac{mg}{\cos \theta}
 \end{aligned} \tag{4.20}$$

Let's define system states for the tailless FWMAV as follows:

$$x_1 = \theta, \quad x_2 = \dot{\theta} \tag{4.21}$$

Then, Lyapunov candidate function is represented by the following equations:

$$V(\mathbf{X}) = \frac{1}{2}x_1^2 + \frac{1}{2}x_2^2 \tag{4.22}$$

Derivating Eq. (4.22) with respect to time,

$$\begin{aligned}
 \dot{V} &= x_1\dot{x}_1 + x_2\dot{x}_2 = x_2(x_1 - \frac{mg}{J \cos \theta}l) \quad \text{let } l = \frac{J \cos \theta}{mg}x_1 + \alpha x_2 \\
 &= -\alpha \frac{mg}{J \cos \theta}x_2^2 \leq 0 \quad \text{where } (0 \leq \cos \theta, -\frac{\pi}{2} \leq \theta \leq \frac{\pi}{2})
 \end{aligned} \tag{4.23}$$

With $\alpha > 0$, derivative of V is negative semi-definite for any x_1 and x_2 , so the origin of the system is stable.

From Eqs. (4.20) and (4.21), closed-loop dynamics is given by

$$\begin{aligned} \dot{x}_1 &= x_2 \\ \dot{x}_2 &= -x_1 - \frac{mg}{J \cos x_1} \alpha x_2 \end{aligned} \quad (4.24)$$

By Lasalle's invariance principle, the closed-loop system is asymptotically stable.

From Eq. (4.23), I can calculate l as follows:

$$l = \frac{J \cos \theta}{mg} \theta + \alpha \dot{\theta} \quad (4.25)$$

Based on the measurement results of Section 3.2, the actuator input that apply to pitch servo is calculated as follows:

$$\begin{aligned} M_y &= l \cdot F = l \cdot (F_l + F_r) \\ &= 0.68u_{pitch}^2 - 6.64u_{pitch} + 0.02 \end{aligned} \quad (4.26)$$

where u_{pitch} is the input of pitch servo.

4.2.3 Yaw direction

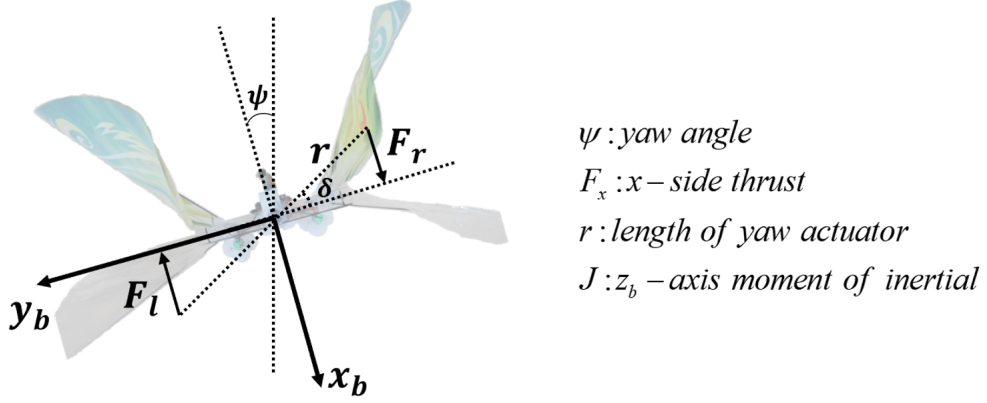


Figure 4.4: FBD of tailless FWMAV about yaw axis.

Based on the free body diagram (FBD) in Fig 4.4, the working torques by thrusts from the left and right wings are applied to COM of the vehicle. Applying the Newton's second law, the rotation dynamics about yaw axis of tailless FWMAV can be simplified to

$$\begin{aligned}
 J\ddot{\psi} &= -F_r r \cos \delta - F_l r \cos \delta, \quad \text{let } (F_r = F_l = F) \\
 &= -2Fr \cos \delta \\
 \ddot{\psi} &= -2\frac{Fr}{J} \cos \delta
 \end{aligned} \tag{4.27}$$

Let's define system states for the tailless FWMAV as follows:

$$x_1 = \psi, \quad x_2 = \dot{\psi} \tag{4.28}$$

Then, Lyapunov candidate function is represented by the following equations:

$$V(\mathbf{X}) = \frac{1}{2}x_1^2 + \frac{1}{2}x_2^2 \tag{4.29}$$

Derivating Eq. (4.29) with respect to time,

$$\begin{aligned}
 \dot{V} &= x_1 \dot{x}_1 + x_2 \dot{x}_2 = x_2 \left(x_1 - \frac{2}{J} Fr \cos \delta \right) \quad \text{let } \cos \delta = \frac{J}{2Fr} x_1 + \alpha \frac{J}{2Fr} x_2 \\
 &= -\alpha x_2^2 \leq 0
 \end{aligned} \tag{4.30}$$

With $\alpha > 0$, derivative of V is negative semi-definite for any x_1 and x_2 , so the origin of the system is stable. From Eqs. (4.27) and (4.28), closed-loop dynamics is given by

$$\begin{aligned} \dot{x}_1 &= x_2 \\ \dot{x}_2 &= -x_1 - \alpha x_2 \end{aligned} \tag{4.31}$$

By the Lasalle's invariance principle, the origin of the system is asymptotically stable.

From Eq. (4.30) I can calculate l as follows:

$$l = r \cos \delta = \frac{J}{2F} \psi + \alpha \frac{J}{2F} \dot{\psi} \tag{4.32}$$

Based on the measurement results of Section 3.2, the actuator input that apply to yaw servo is calculated as follows:

$$\begin{aligned} M_z &= l \cdot F = l \cdot (F_l + F_r) \\ &= -0.26u_{yaw}^2 + 1.92u_{yaw} + 0.13 \end{aligned} \tag{4.33}$$

where u_{yaw} is the input of yaw servo.

4.2.4 PID control

The motion capture system, VICON, provides 3D positions and attitude information. I only use attitude information for the attitude regulation, and it is transmitted from GCS to the tailless-FWMAV via Bluetooth communication. Details can be found in Section 5.2.

In Eqs 4.18, 4.25, and 4.32, the control inputs to the three axes direction are similar to PD controller structure. Therefore, by adding the integral term, I design simple PID controllers in parallel structure, assuming that three controllers for roll, pitch, and yaw work independently.

Two PID controllers for roll direction are written in the following form:

$$\begin{aligned} u^l &= u_0^l + (k_p^l e + k_i^l \int e dt + k_d^l \frac{d}{dt} e) \\ u^r &= u_0^r - (k_p^r e + k_i^r \int e dt + k_d^r \frac{d}{dt} e) \\ e &= (\phi_r - \phi) \end{aligned} \tag{4.34}$$

In Eq. (4.34), $u^{\{l,r\}}$ represent the control inputs for the left and right motors, respectively, and $u_0^{\{l,r\}}$ are the offsets for supporting the weight of the FWMAV. ϕ_r is the reference roll angle and ϕ is the measured roll angle.

In the case of pitch and yaw directions, a PID control can be also simplified to

$$\begin{aligned} u^{servo} &= u_0^{servo} + (k_p^{servo} e + k_i^{servo} \int e dt + k_d^{servo} \frac{d}{dt} e) \\ e &= (\theta_r - \theta), (\psi_r - \psi) \end{aligned} \tag{4.35}$$

In Eq. (4.35), u^{servo} is a control input for the servo and u_0^{servo} is the nominal input. θ_r and ψ_r are the reference pitch and yaw angles, and θ and ψ are the measured pitch and yaw angles. In Eqs. (4.34) and (4.35), $k_p^{\{l,r,servo\}}$, $k_i^{\{l,r,servo\}}$, and $k_d^{\{l,r,servo\}}$ are proportional, integral, and derivative gains, respectively. The gains, offsets, and nominal inputs are determined by trial-and-error.

4.3 Trajectory tracking control

In order to move along a given trajectory, it is necessary to change the Euler angles of the platform according to the desired attitudes. Especially, pitch and roll angles are directly related to x-and y-directional movements, so the flight platform needs the desired pitch and yaw angles to move X and Y positions. The yaw angle is not related to the movement of the platform, so always maintain zero degrees.

The reference roll and pitch angles can be written

$$\begin{aligned}\theta_r &= k_p^x e_x - k_d^x \frac{d}{dt} e_x, \quad e_x = (x_r - x) \\ \phi_r &= k_p^y e_y - k_d^y \frac{d}{dt} e_y, \quad e_y = (y_r - y)\end{aligned}\tag{4.36}$$

In Eq. (4.36), x_r and y_r are the reference x-and y-positions, and x and y are the measured positions. $k_p^{\{x,y\}}$ and $k_d^{\{x,y\}}$ are proportional and derivative gains, respectively, which are chosen by trial-and-error. When θ_r and ϕ_r are calculated according to the given trajectory information, the reference angles are reflected in Eqs. (4.34) and (4.35) to calculate the control inputs for DC motors and servo motors.

To control the altitude of the flight vehicle, a PID controller based on height error is used, and the calculated input terms are summed up with the inputs of Eq. (4.34). Table 4.5 shows a double-loop control structure for regulating an attitude and tracking a trajectory.

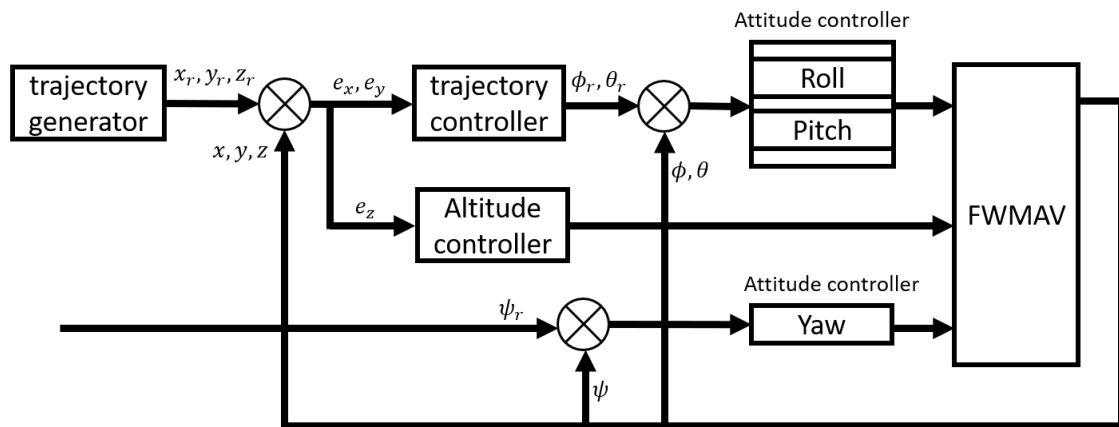


Figure 4.5: Signal flow for the closed-loop feedback control to regulate the attitude of the platform and for trajectory tracking flight. Euler angles are provided by the external system (VICON). (signal-loop and double-loop structure).

5

Attitude regulation experiments

In order for a tailless FWMAV to fly, it needs control to maintain a stable attitude in real-time from the wing mechanism. I use an external mechanical device for attitude regulation of the platform because there is a high risk of damage if the vehicle falls. In this Section, I describe a gyroscope and universal joint testbeds for attitude regulation experiments and explain the experimental environment. Also, I present simulation and experimental results based on the designed control scheme. The corresponding results consist of two parts: considering the situation where 1) only one Euler angle is compensated and the other angles are fixed, and 2) three Euler angles are free simultaneously.

5.1 Design of gyroscope testbed

A tailless-FWMAV is known as an inherently unstable flight platform rather than general FWMAVs whose tail wing plays a role as passive control surfaces. Therefore, real-time active control of the wing mechanism is necessary to regulate the platform's attitude nimbly. Platforms developed for flight need to carry out various flight experiments in the air. Any designed controller, however, cannot guarantee flight stability in physical environments, so much time and effort are required to attain suitable control parameters. In addition, the platform is easily broken when it collides with the external environment. To overcome the above issues, I plan an experiment to regulate

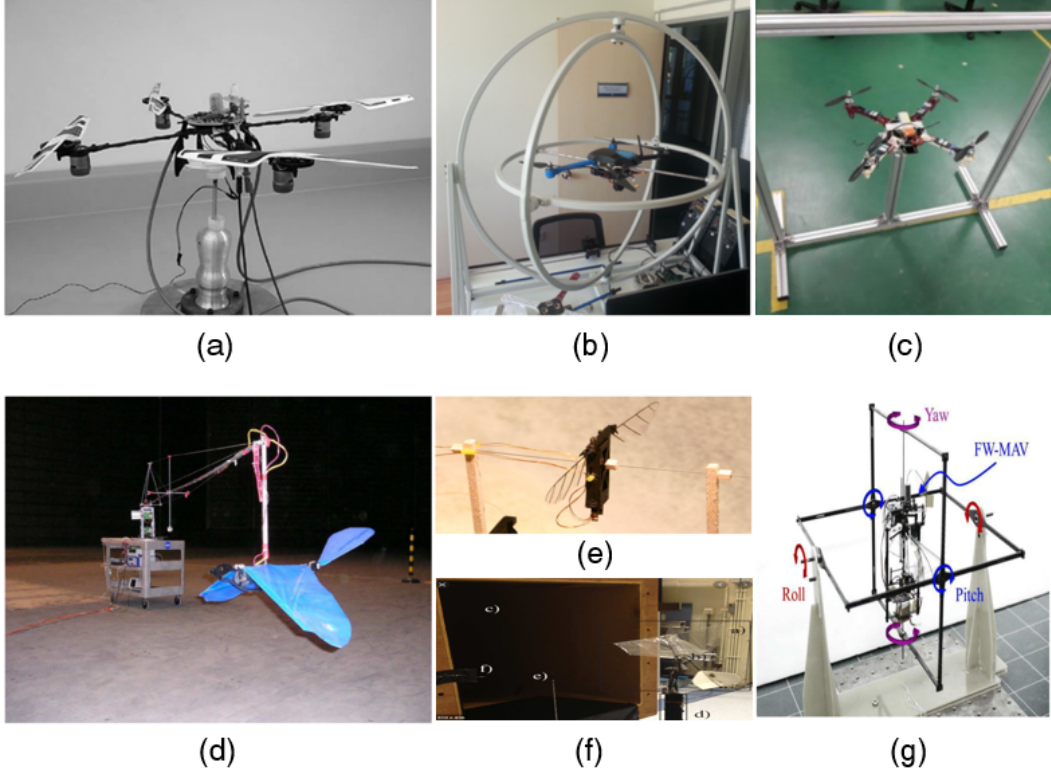


Figure 5.1: Examples of using an external device; (a) [51], (b) [52], (c) [53], (d) [54], (e) [55], (f) [56], and (g) [39].

the attitude of the vehicle by using a gyroscope testbed. The use of an external mechanical device for attitude control has been tried in a number of papers, and Fig 5.1 shows various examples of experimental environment.

Fig. 5.2 shows the tailless-FWMAV installed inside the gyroscope apparatus, and the direction of Euler angles is marked on the figure. Both white colored-brackets which support pillars are printed by a 3D printer. The lengths of the pillars and brackets are long enough so that the core part of the gyroscope testbed does not hit the ground during rotation. In addition, the core part of the testbed must be at a sufficient height from the ground to reduce the ground effect. The frames of the apparatus are made of MDF material to reduce its weight and are cut by a laser cutting machine. The total weight of the frames is about 85 grams, which is less than 3.5 times the weight of the platform. The metal rods with a diameter of 1 mm are used as shafts in every

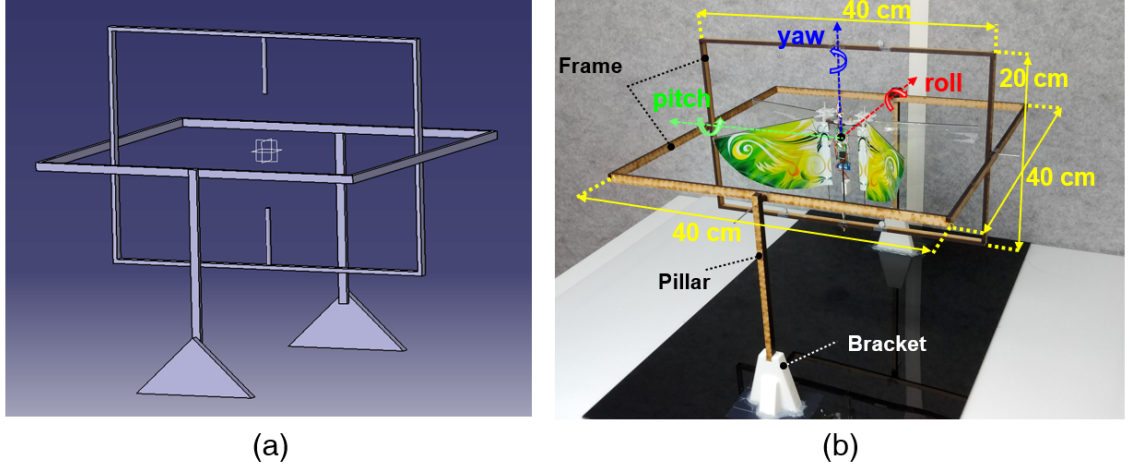


Figure 5.2: Designed gyroscope testbed. Most of the frames are made by MDF materials except for the brackets; (a) 3D image by CATIA program, (b) Actual testbed with tailless FWMAV.

rotating area such as pillar/frame and frame/frame, and the rods have sufficient rigidity, so they are not bent by the weight of the combined system. For reducing rotating friction, I use ball bearings at all the joints. The inner space of the rig is about $40 \times 40 \times 20 \text{ cm}^3$, which is enough to prevent the platform from bumping into the frames in any direction. The center of mass (COM) of the platform is set as close to the center of the testbed to alleviate the loss of force generated by the offset of the center of rotation. The apparatus can rotate simultaneously on three axes, and I can also fix a specific axis for a piece-wise test.

5.2 Experimental environment

The motion capture system is a global positioning system (GPS) that can be used in indoor environments. The system provides real-time information on the location and attitude of objects within a defined space, so it is widely used for research areas about robot guidance, navigation, control, and application. In this thesis, I use VICON system, a type of motion caption system, to obtain location and attitude information.

Fig. 5.3 shows the experimental environment. It is a space where ten cameras are installed, and a $5 \times 7 \times 2 \text{ m}^3$ (*width* \times *length* \times *height*) volume can be used as an activity area. The equipment

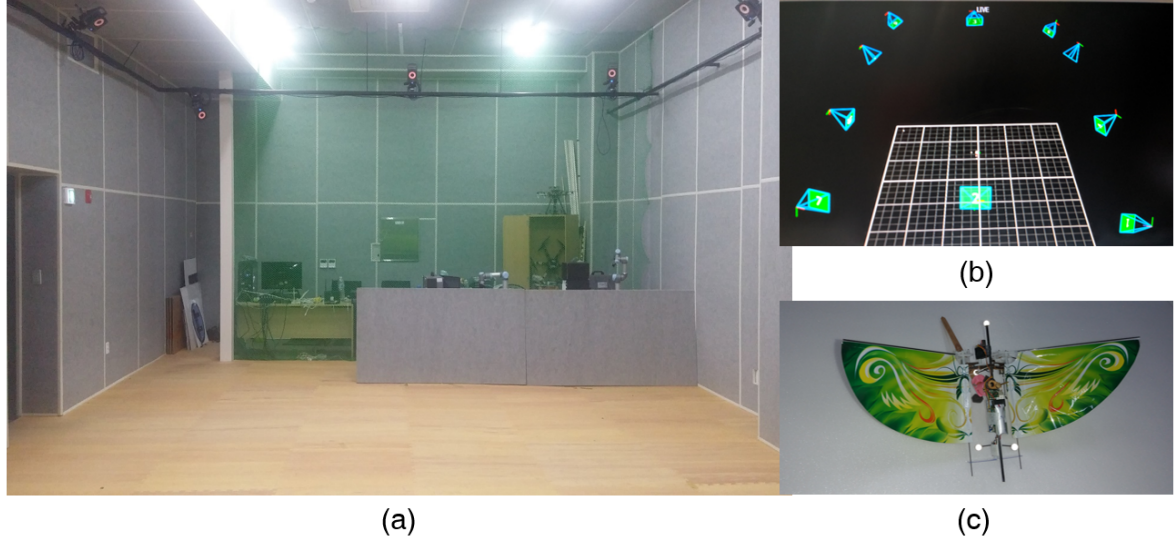


Figure 5.3: Indoor experimental environment; (a) VICON cameras are located on the upper edge of the room, (b) VICON software, and (c) Tailless FWMAV with four reflective markers.

can provide real-time information at a maximum speed of 150 Hz. In order to maintain the stability of the communication connection between the platform and ground computer, I conduct all experiments by setting the speed of the Bluetooth communication module mounted on the robot and VICON to 100 Hz.

5.3 Roll axis free

First, I focus on regulating a roll angle, so I secure the other axes, i.e. pitch and yaw angles. Since the pitch and yaw axes are not regulated, a control input corresponding to the nominal value is applied to each servo motor. In the case of roll axis, PID type control inputs derived in Section 4.2.1 are used to two DC motors. Let's look at the simulation results and the actual experiment results in the sections below.

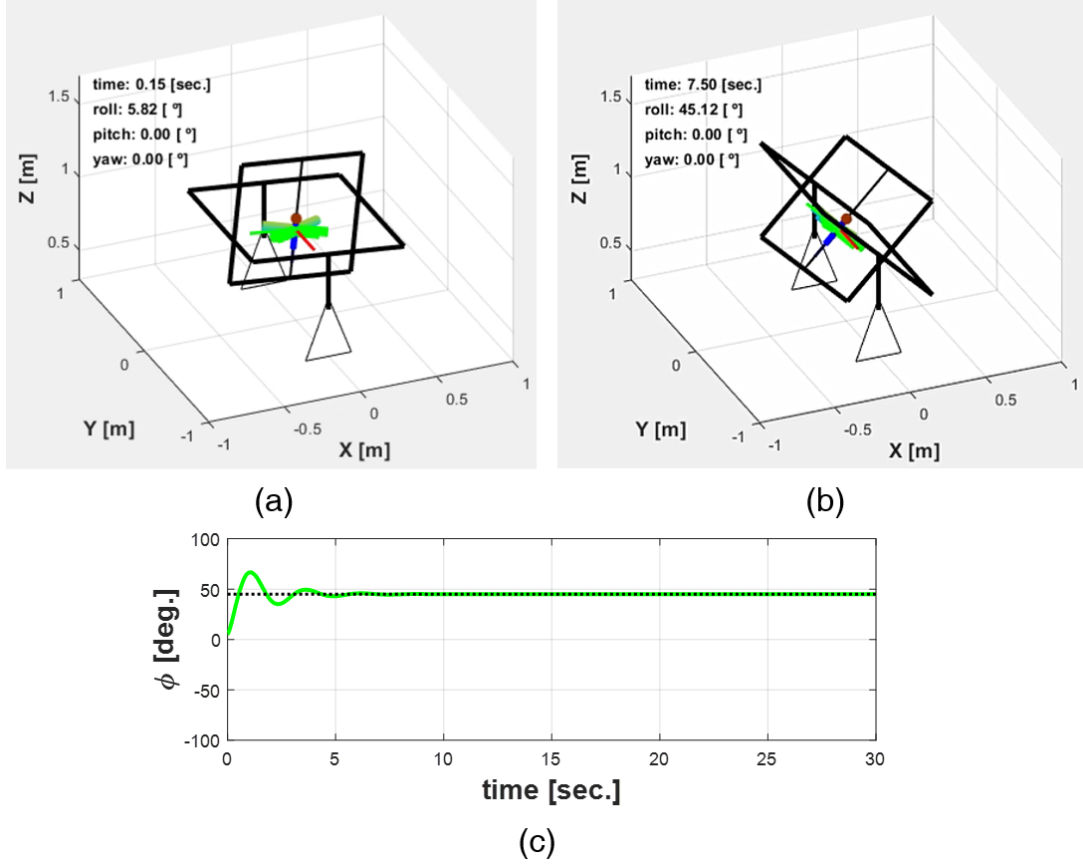


Figure 5.4: Simulation results of roll angle regulation. Reference angle is $+45$ degrees. (a) Initial state, (b) The point in time after 7.5, seconds, and (c) Time history graph of roll angle regulation.

5.3.1 Simulation

Fig. 5.4 shows the simulation results of the regulation of roll angle. Since pitch and yaw axes are fixed, two angles keep 0 degrees during the whole time. The initial roll angle starts at 5.82 degrees. It can be seen that the initial roll value vibrates, but converges to the reference angle of 45 degrees within 5 seconds. The reaction in the transition state can be changed by adjusting the gain of the controller that controls the DC motors.

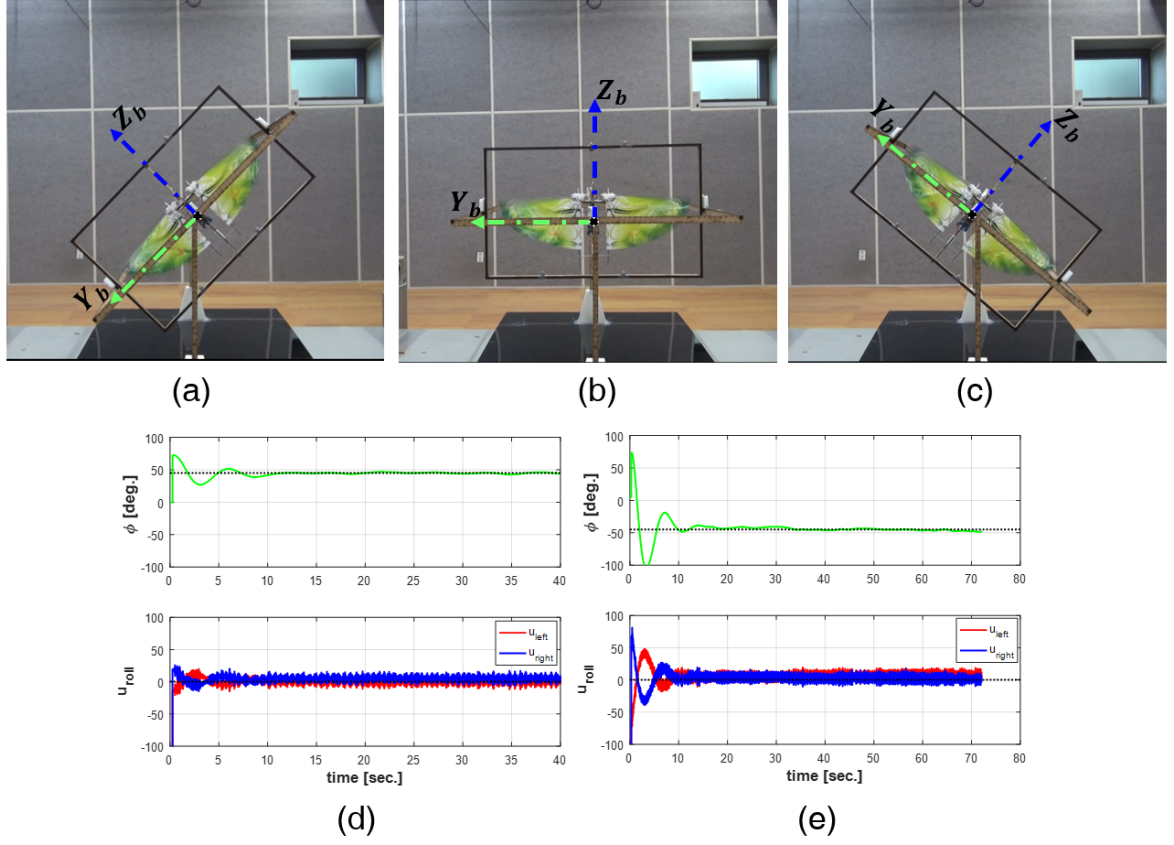


Figure 5.5: Experiment results of roll angle regulation. Captured images at various reference angles; (a) -45° , (b) 0° , (c) $+45^\circ$, and (d-e) Time history of roll angle and control input of two DC motors.

5.3.2 Experiment

Fig. 5.5 shows captured images at three different reference roll angles and the corresponding experimental results. In all of the trials, the initial angle of the platform to the roll axis begins at the point that it is not zero degrees and it takes 15 seconds to converge to the reference roll angle from the initial state. In Fig. 5.5. (d) where the reference roll angle is 45 degrees, and the control input graph of DC motors shows that the value of the right motor is greater than the left motor. The corresponding pattern on the graph also shows that the output of the right motor must be greater to maintain the reference angle of 45 degrees. In the opposite case where the reference roll angle is -45° , it can be confirmed that the value of the left motor is greater than the value of the

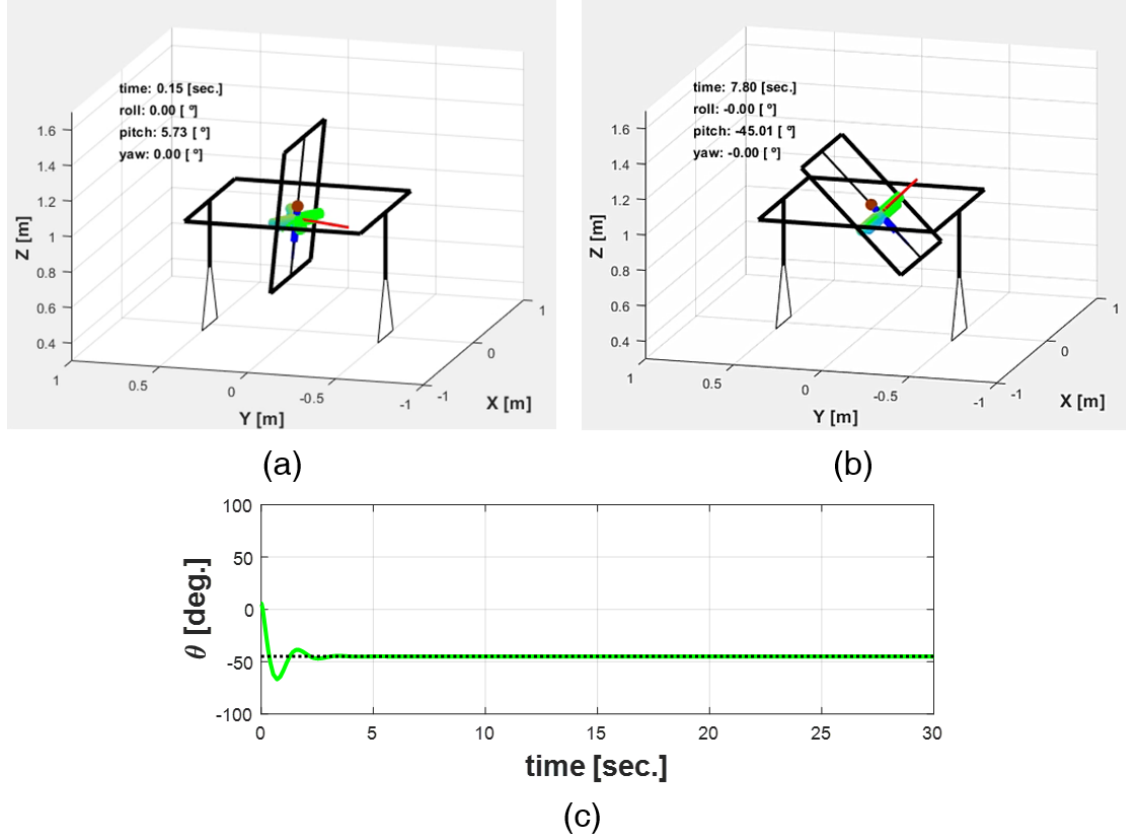


Figure 5.6: Simulation results of pitch angle regulation. Reference angle is -45 degrees. (a) Initial state, (b) The point in time after 7.8 seconds, and (c) Time history graph of pitch angle regulation.

right motor. The actual experimental results and simulation results show similar aspects.

5.4 Pitch axis free

Securing the other axis, i.e. yaw and roll directions, I try to control a pitch angle. Since the yaw and roll axes are not regulated, a control input corresponding to the nominal value is applied to DC motors and servo motor which controls the yaw angle. In the case of pitch axis, a PID type control input derived in Section 4.2.2 is used to a servo motor which controls the pitch angle. Let's look at the simulation results and the actual experiment results in the sections below.

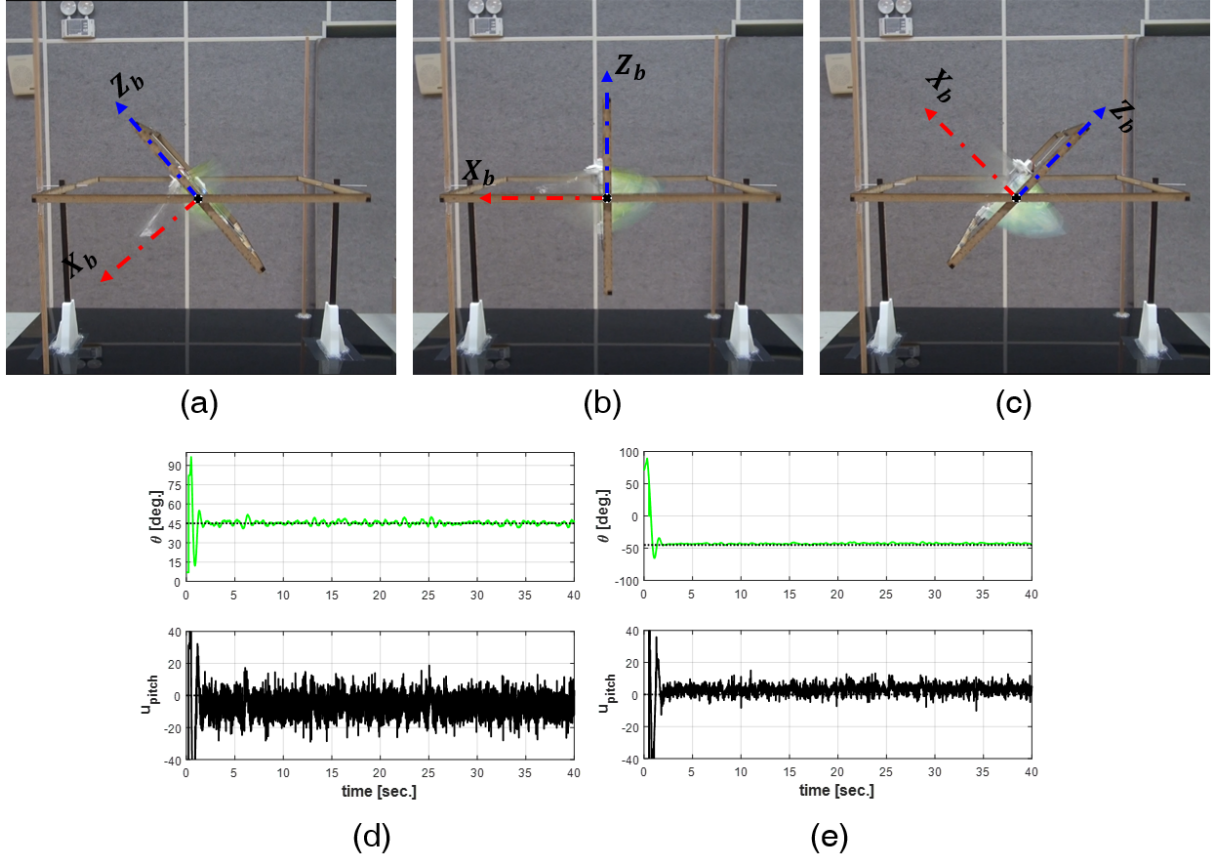


Figure 5.7: Experiment results of pitch angle regulation. Captured images at various reference angles; (a) -45, (b) 0, (c) +45, and (d-e) Time history of pitch angle and control input of pitch servo motor.

5.4.1 Simulation

The simulation results of the regulation of pitch angle are shown in Fig. 5.6. Since I fix yaw and roll axes, two angles keep 0 degrees during the whole time. The initial pitch angle starts at 5.73 degrees. It can be seen that the initial pitch value vibrates, but converges to the reference angle of -45 degrees within 4 seconds. Adjusting the gain of the controller that controls the servo motor, I can change the reaction in the transition state.

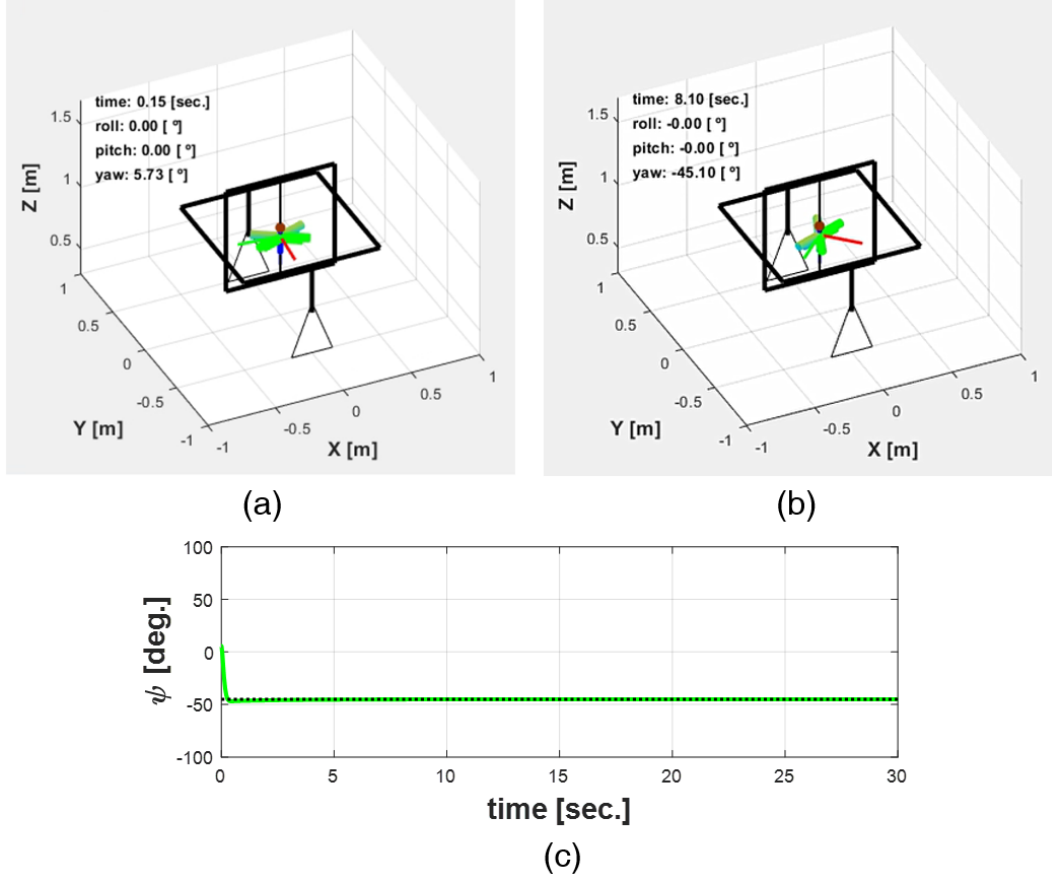


Figure 5.8: Simulation results of yaw angle regulation. Reference angle is -45 degrees. (a) Initial state, (b) The state after 8.1 seconds, and (c) Time history graph of yaw angle regulation.

5.4.2 Experiment

The captured images at three different reference pitch angles and the corresponding experimental results are shown in Fig. 5.7. The initial pitch angle of the platform starts at a nonzero degree in all cases and it takes less than five seconds to reach the reference pitch angle from the initial state. In the case of the experiment of the pitch axis, the time taken to reach the reference angle is less than the experimental of the roll axis and the responsiveness could be adjusted by tuning the gain of the controller. The actual experimental results show a similar pattern to the simulation results.

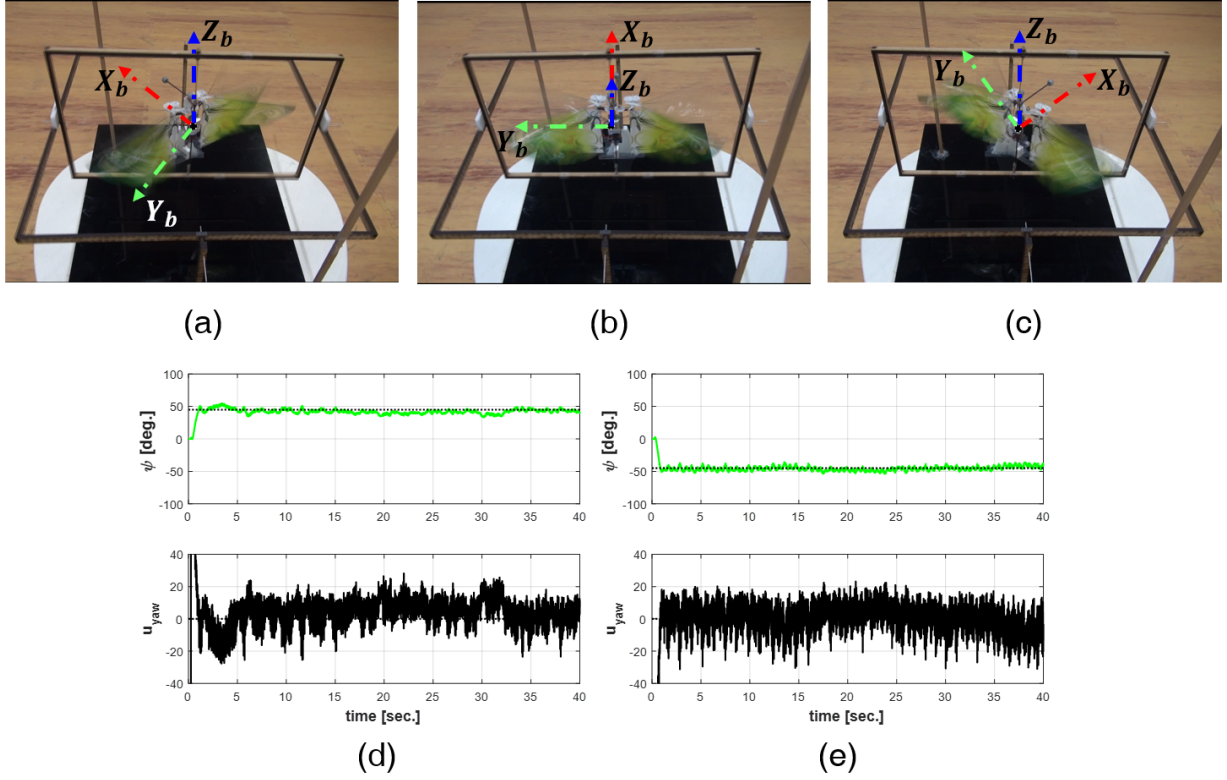


Figure 5.9: Experiment results of yaw angle regulation. Captured images at various reference angles; (a) -45, (b) 0, (c) +45, and (d-e) Time history of yaw angle and control input of yaw servo motor.

5.5 Yaw axis free

In the case of regulating a yaw angle, I only allow the yaw axis to rotate freely. DC motors and servo motor which controls pitch angle are provided with nominal control inputs, and a PID type control input derived in Section 4.2.3 is used to a servo motor which controls yaw angle. Let's look at the simulation results and the actual experiment results in the sections below.

5.5.1 Simulation

Fig. 5.8 shows the simulation results of the regulation of yaw angle. Since roll and pitch axes can not rotate, both angles are always 0 degrees during the entire time. The initial yaw angle starts at 5.73 degrees. It can be seen that the initial yaw value vibrates, but converges to the reference

angle of -45 degrees within 2 seconds. The reaction in the transition state can be changed by adjusting the gain of the controller that controls the servo motor.

5.5.2 Experiment

Fig. 5.9 shows the results captured during the experiment for various reference yaw angles and the initial yaw angle starts at 0 degrees. It does not take five seconds to reach the reference angle. Although there is a little chattering phenomenon near the reference angle, the platform continues to maintain the reference angle without deviating the desired angle significantly. As in roll and pitch experiments, the actual experimental results are similar to the simulation results.

5.6 All axes free

The convergence rate and response for setpoint depend on the control gains and I can determine gain parameters according to experiment purpose. In order to maintain hover flight of tailless FWMAV, all Euler angles should be kept close to zero degrees. To this end, the platform actively controls four actuators such as two DC motors for roll angle and two servo motors for pitch and yaw angles.

In the previous Section, I talked about situations where the three axes of the platform are not considered simultaneously. From now on, I talk about the results of controlling the three axes at the same time. Let's look at the simulation results and the actual experiment results in the Sections below. For regulating each axis, three independent controllers derived in Section 4.2 are used.

5.6.1 Simulation

Fig. 5.10 shows the simulation results for regulating Euler angles. The initial roll, pitch, and yaw angles are 81.52, 80.21, and 80.21 degrees, respectively. It can be seen that all three axes converge to a reference angle of 0 degrees within ± 2 degrees within 10 seconds.

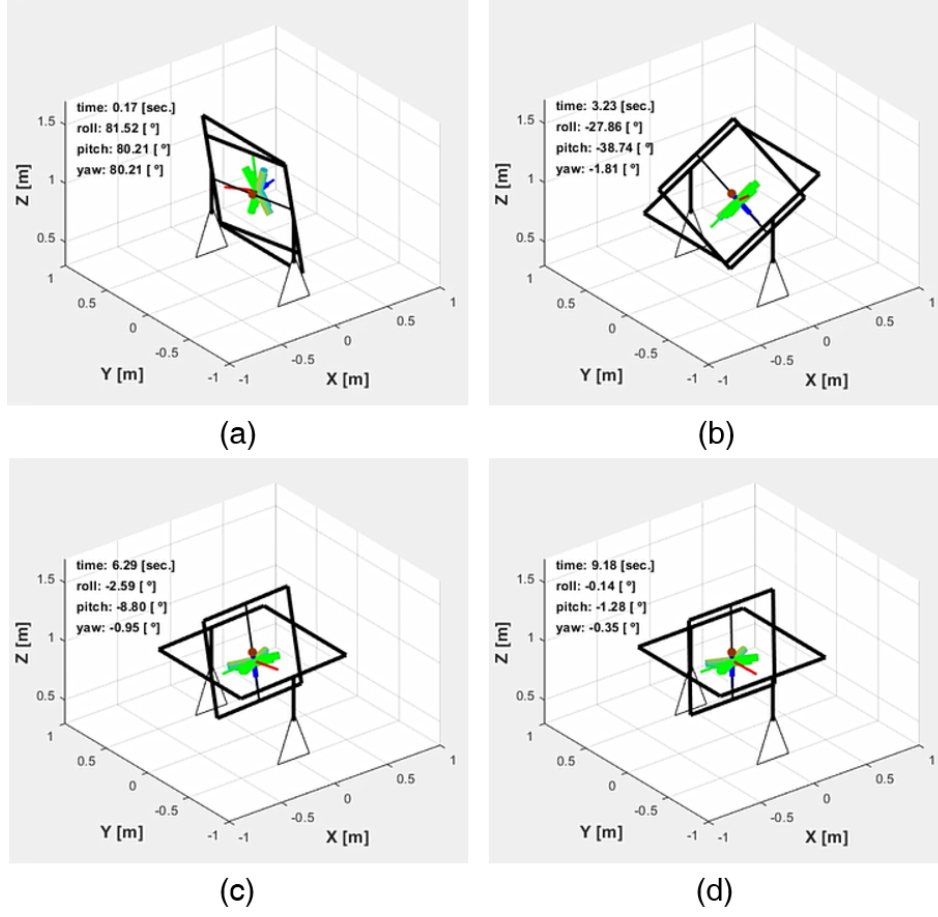


Figure 5.10: Hovering situation to regulate all Euler angles; (a) Initial state, (b) The state after 3.23 seconds, (c) The state after 6.29 seconds, and (d) The state after 9.18 seconds.

5.6.2 Experiment

For hovering flight, a flight vehicle keeps zero degrees with respect to all Euler angles. Fig. 5.11 shows the results of using feedforward control for attitude regulation. Without feedback control, the platform maintains an undesired attitude or rotate randomly. If there is no gyroscope testbed, the platform must be dropped on the ground as soon as it takes off.

Fig. 5.12 shows the experimental results under the condition that all rotational axes are not fixed. To regulate attitudes for three axes simultaneously, I use control gains in Section 5.3 for roll direction, Section 5.4 for pitch direction, and Section 5.5 for yaw direction. The gain values

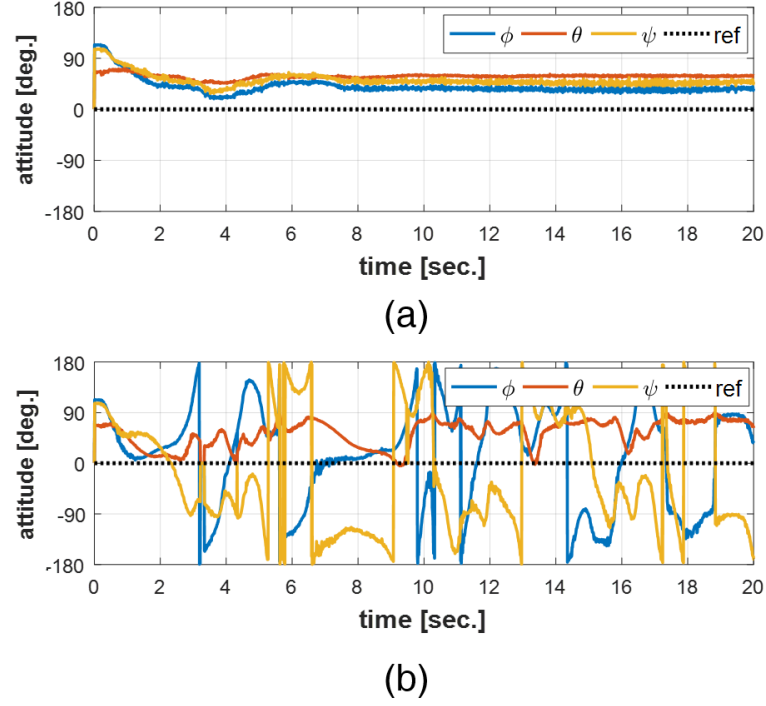


Figure 5.11: Without feedback control; (a) Euler angles stay at a non-zero meaningless value, (b) Euler angles vary randomly.

of the controller for all axes are summarized in Table 5.1. In Fig 5.12.(c), the platform reaches a reference angle (zero degrees) within four seconds and keeps the angles until 20 seconds. As soon as the controllers are turned off at 20 seconds, the vehicle loses its attitudes and rotates randomly for 10 seconds when the controllers are not working. After the controllers are turned on at 30 seconds, the platform controls its attitude to desired angles again within four seconds and keeps reference angles until 60 seconds. Based on the experimental results, the control strategy I designed guarantees the hovering flight of tailless FWMAV.

For the platform to move, it is necessary to change the flight attitude, especially roll and pitch angles (For attitude stability, roll and pitch angles are more critical than yaw angle.). So, I conduct an experiment on how well tailless FWMAV follows a sinusoid reference angle, and Fig 5.13 shows the experimental results about roll and pitch axes, respectively. I set the maximum amplitude of the reference sinusoid signal about the roll axis to ± 10 degrees and set about the pitch axis to ± 30

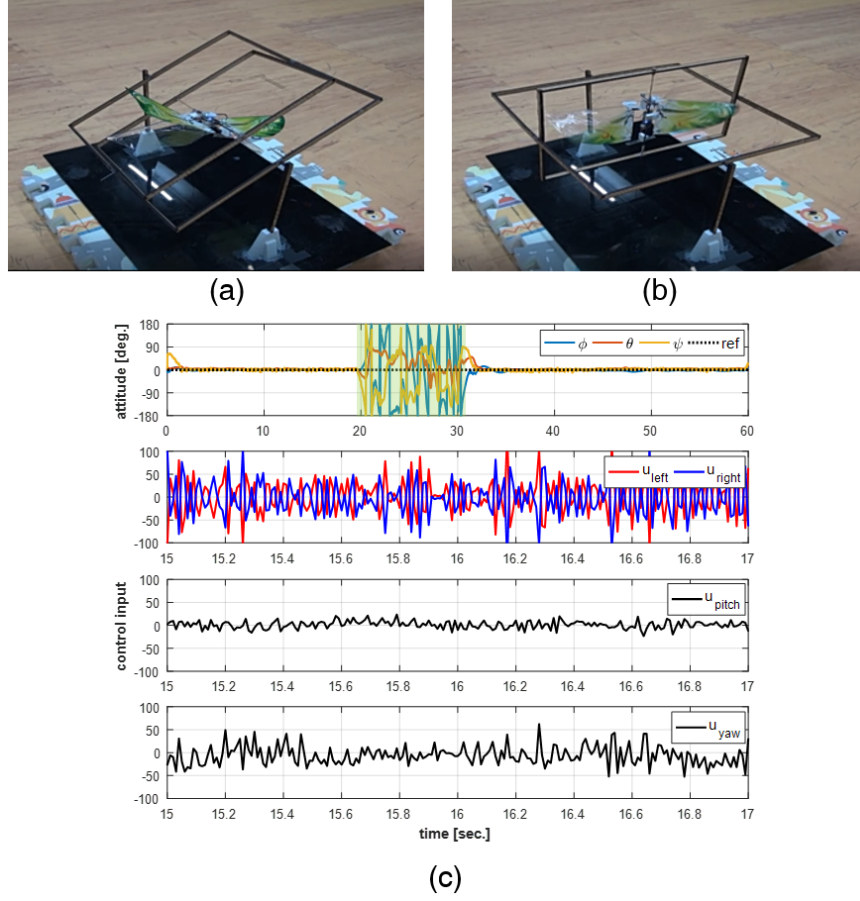


Figure 5.12: Hovering situation to regulate all Euler angles; (a) Initial state, (b) Hovering state, and (c) Time history of Euler angles and control inputs of DC motors and servo motors.

degrees. In all cases, I confirm that the roll and pitch angles follow well the changing reference angles without long delay and considerable variation.

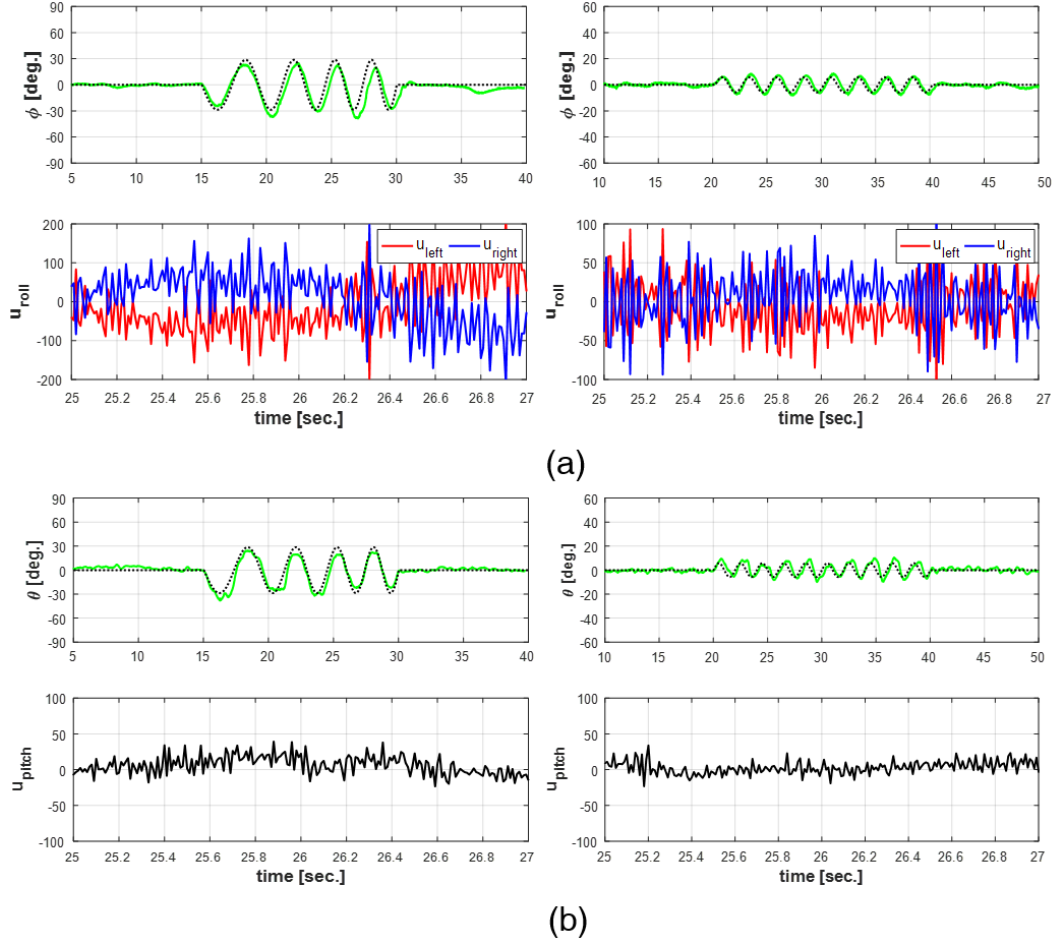


Figure 5.13: Time history of measurement results about sinusoid reference angle; (a) The results of roll angle tracking, (b) Pitch angle tracking.

5.7 Design of universal joint testbed & Experiment

The weight of the gyroscope testbed is approximately 85 grams, which is about 3.5 times the weight of the platform. Therefore, the movement of the vehicle within the rig is bound to be limited due to the effect of the inertia of the device. This leads to using a high gain of the controller and may cause an excessive reaction to the attitude control of the tailless FWMAV in the absence of the gyroscope testbed. Therefore, I conduct an additional experiment using a universal joint that could have less effect on the movement of the vehicle than the gyroscope.

Axis	Gain	Gyroscope testbed	Universal joint testbed
Roll	P	± 0.5	± 0.2
	I	± 0.05	± 0.05
	D	± 0.4	± 0.1
Pitch	P	0.7	0.02
	I	0.04	0.03
	D	0.3	0.03
Yaw	P	-4.5	-2
	I	-0.01	-0.01
	D	-0.04	-0.03

Table 5.1: PID control gains for attitude regulation in two testbeds.

To reduce the effect of the inertia of the universal joint on the behavior of the platform, like the mount that was made during force and torque measurements, I use a 3D printer to make the joint using plastic filament materials. The printed joint weights 10 grams, which is about 0.4 times the weight of the vehicle. The rotation range of motion is smaller than that of the gyroscope testbed, but it can also be rotated in three axes simultaneously.

Fig. 5.14 shows the platform attached to the universal joint testbed and experimental results. About 15 seconds after the control inputs are generated, Euler angles converge to 0 degrees to achieve hover flight condition. The reason it takes time to converge is because of the asymmetry of the shape of the platform that occurs during the manufacturing process. The convergence rate can be adjusted by using different control gains. Table. 5.1 shows the gain values of the attitude controller used in the universal joint testbed, and the gain values of the universal joint experiment are relatively smaller than the gyroscope testbed. This is the effect of the difference in the weight of two testbeds.

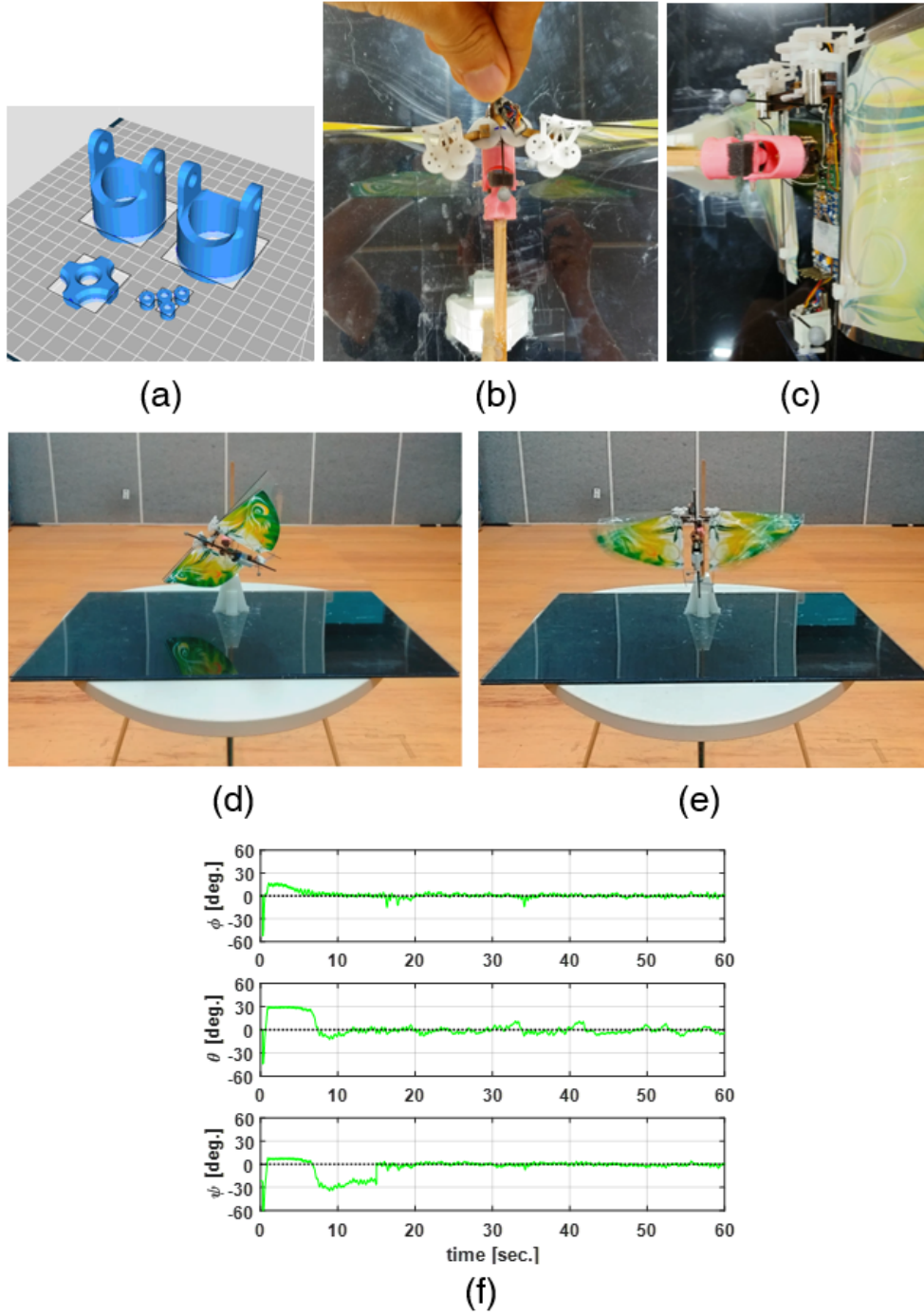


Figure 5.14: Universal joint testbed for attitude regulation; (a) CAD design of universal joint, (b) View from above, (c) View from side, (d) Initial attitude, (e) Hovering state, and (f) Time history of Euler angles.

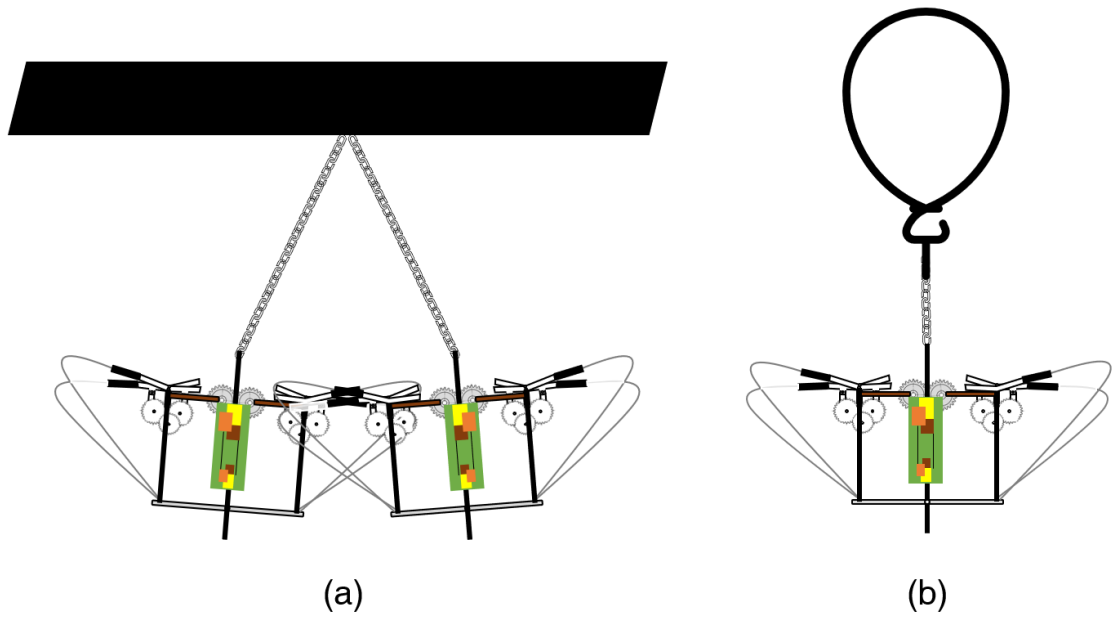


Figure 5.15: Tethered flight environment for trajectory tracking control environment; (a) Tied-to-the-ceiling, (b) Hung-to-a-balloon.

6

Trajectory tracking

In this Section, I explain the research on the trajectory tracking of a tailless FWMAV. First, simulation results about various trajectories are presented. Second, two experimental environments (tethered-flight situation) and the corresponding experimental results are described. Finally, I cover the experimental result of the autonomous hovering flight of the platform without external assistance.

6.1 Simulation

In order to track a trajectory of an aerial vehicle, position information with time history must be transmitted to the platform in real-time. For moving in the X and Y axes, there only exist the change of the roll and pitch angles. The yaw angle is always controlled to maintain 0 degrees.

Using the attitude dynamics of the tailless FWMAV covered in Section 4.2, a simulation is performed to follow three trajectories using the double-loop control structure mentioned in Section 4.3. Table 6.1 summarizes the simulation parameters and the simulation results are shown in Fig. 6.1. In all cases, the reference height is 1 *m*, and the platform starts at (0,0) in XY-plane. At the initial phase, the platform approaches the target point to follow the reference trajectory and then follows it with a small error.

	Parameter value & Trajectory information
Velocity [m/s]	$V_x = 1, V_y = 1, V = \sqrt{V_x^2 + V_y^2}, \omega = V/r$
Straight line	$X_{ref.} = 0, Y_{ref.} = V_y \cdot time$
Circle shape	$r = 2, X_{ref.} = r \cdot \cos(\omega \cdot time), Y_{ref.} = r \cdot \sin(\omega \cdot time)$
Number eight shape	$r = 4, X_{ref.} = r \cdot \cos(\omega \cdot time), Y_{ref.} = r \cdot \sin(2\omega \cdot time)/2$

Table 6.1: Simulation parameters for trajectory tracking.

6.2 Preliminary

As a preliminary research stage for free flight, experiments are conducted by attaching an external structure such as a thread or a sail to the flight vehicle. The main reason for the aid of external devices is to increase the additional passive stability of the vehicle.

Two experimental environments are considered. In the first case, it is an environment where the fishing line connects the top of the platform to the ceiling. Although the vehicle is fastened to the fishing line, it can rotate in three axes around a knot connected to the upper part of the platform. The purpose of the experiment in the first environment is to confirm that the tailless FWMAV moves well along the trajectory on the 2D plane. In order not to change the altitude of the platform, the control inputs calculated by altitude error are not considered for controlling both DC motors.

In the second case, it is an environment where a balloon containing helium gas is connected to the top of the platform. Since the balloon is less dense than the surrounding air, the balloon provides extra lift to the vehicle. So, the platform minimizes power consumption, saving battery power, and can increase flight time. In addition, the volume of the balloon increases passive stability because it resists the movement of the vehicle. The purpose of the experiment in the second environment is to confirm that the tailless FWMAV moves well along the trajectory on the 3D space. Unlike the first case, attitude and altitude controllers operate for tracking the trajectory. Fig. 5.15 shows two experimental environments described above.

I consider three trajectories such as moving toward 1) X-direction, 2) Y-direction, and 3) Square shape. The detailed trajectory information is shown in Tables 6.2, 6.3, and 6.4.

	Tied-to-the-ceiling	Hung-to-a-balloon
Time [sec.]	V_x [m/s]	V_x [m/s]
0-10	0	0
10-20	0.06	0.1
20-30	0	0
30-50	-0.06	-0.1
50-60	0	0
60-70	0.06	0.1
70-80	0	0

Table 6.2: Moving toward X-direction; ($V_y = 0$).

6.3 Experiment: Tied-to-the-ceiling

Figs. 6.2, 6.3, and 6.4 show the tracking results about three different trajectories. Each figure shows how the aircraft moved over time on the XY plane. Then, let's look at the details more each result.

Fig. 6.2 shows the experimental results of the vehicle moving in the x-axis direction. It can be seen that there is no much movement on the y-axis. On the other hand, the platform follows well along the provided trajectory in the x-axis direction while maintaining the reference speed. Since the height is not controlled, the height slightly increases in the z-direction at both ends of the x-axis due to the constant length of the string. In addition, there exists shaking in the trajectory on the XY-plane due to the tension of the string.

The experimental results of the vehicle moving in the y-axis direction is shown in Fig. 6.3. There is no much movement on the x-axis direction. On the other hand, the platform follows well along the provided trajectory in the y-axis direction while maintaining the reference speed. As shown in the previous case, since the altitude is not controlled, the altitude increases in the z-direction at both ends of the y-axis due to the constant length of the string. In addition, there exists shaking in the trajectory on the XY-plane due to the tension of the string.

Fig. 6.4 shows the experimental results of the vehicle moving toward a square trajectory. Starting from (0, 0), the platform passes through four vertices, i.e., (0.6, 0), (0, 0.6), (-0.6, 0), and (0,

	Tied-to-the-ceiling	Hung-to-a-balloon
Time [sec.]	V_y [m/s]	V_y [m/s]
0-10	0	0
10-20	0.06	0.1
20-30	0	0
30-50	-0.06	-0.1
50-60	0	0
60-70	0.06	0.1
70-80	0	0

Table 6.3: Moving toward Y-direction; ($V_x = 0$).

-0.6) exactly. The altitude increased slightly in the z-axis direction from the four vertex positions due to the constant length of the string. Although there are small variations in trajectories and attitudes, the platform follows three reference trajectories well while maintaining attitude stably.

6.4 Experiment: Hung-to-a-balloon

Figs. 6.5, 6.6, and 6.7 show the tracking results about three different trajectories. Each figure shows how the aircraft moved over time on the XYZ space.

In all cases, since the departure of the trajectory begins at $(0, 0)$, the platform heads to $(0, 0)$ as soon as it takes off from the human hand. After arriving at $(0, 0)$, a little overshoot on the z-axis occurs while controlling the reference altitude. As time goes on, the vehicle moves accurately along the 3D trajectory. Because it is less affected by the tension of the string, there is less shaking in the trajectory than in the previous cases.

Fig. 6.8 shows the result of rotating a circle with a radius of 1 m every 20 seconds. Because the yaw angle is always kept at zero degrees, the velocity drops whenever the vehicle changes direction, causing the altitude to fluctuate.

	Tied-to-the-ceiling		Hung-to-a-balloon
Time [sec.]	V_x, V_y [m/s]	Time [sec.]	V_x, V_y [m/s]
0-5	0, 0	0-10	0, 0
5-10	0.12, 0	10-20	0.1, 0
10-15	-0.12, 0.12	20-30	-0.1, 0.1
15-20	-0.12, -0.12	30-40	-0.1, -0.1
20-25	0.12, -0.12	40-50	0.1, -0.1
25-30	0.12, 0.12	50-60	0.1, 0.1
30-35	-0.12, 0	60-70	-0.1, 0
35-45	0, 0	70-80	0, 0

Table 6.4: Moving toward square shape.

	Tied-to-the-ceiling			Hung-to-a-balloon		
Error	X-direction	Y-direction	Square	X-direction	Y-direction	Square
X	0.0795	0.0385	0.0937	0.0419	0.0735	0.0356
Y	0.0453	0.0397	0.0883	0.0785	0.0441	0.0305
Z	-	-	-	0.0512	0.0488	0.0654

Table 6.5: RMSE of trajectory tracking experiments.

6.5 Summary

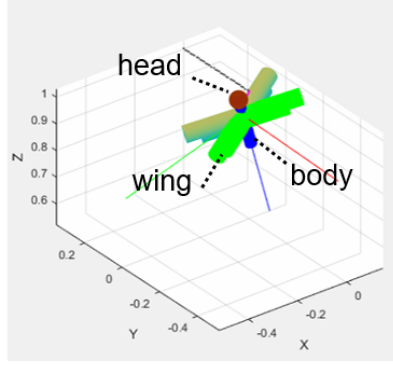
Table 6.5 shows the root mean square error (RMSE) between the reference trajectory and actual travel distance in two experimental environments for three different trajectories. RMSE is given by

$$RMSE = \sqrt{\frac{\sum_{i=1}^n (x_i - \hat{x}_i)^2}{n}} \quad (6.1)$$

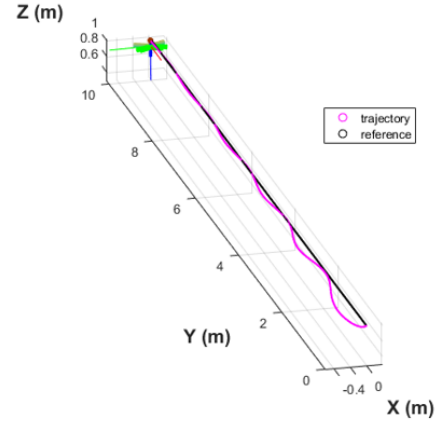
where x_i is a actual value, \hat{x}_i is a measured value, and n is the number of samples. It is difficult to say which of the two environments has smaller errors, but both cases have errors within 10 *cm* in all directions.

6.6 Hovering flight

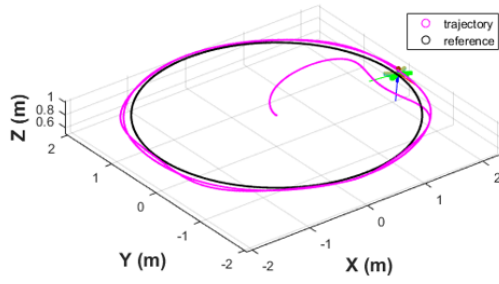
As a condition for hovering maneuvers in place, the flight vehicle stays in a certain area, and the flight altitude must be maintained. Fig. 6.9 shows the experimental results of autonomous hovering flight without the aid of the external environmental factors that help with the flight I used the previous Section. For the flight experiment, I set the flight height as 2 m. In Fig. 6.9.(b), the flight altitude gradually decreases after maintaining the height for about 6 seconds after reaching the reference altitude of 2 m within five seconds without overshoot. If I use a large gain for the altitude controller, the platform can approach the reference height in a shorter time, but there is a possibility of overshoot, so trade-off exists. The trajectory of the platform is maintained within a circle within 1m shown in Fig. 6.9.(d) and the error on the y-axis is relatively larger than the x-axis. Especially, The area outside the circle with a radius of 1 m is the trajectory of the vehicle as it descends after 11 seconds. The attitude of the platform remains within ± 45 degrees during flight. In order to fly in place, it is theoretically correct for all Euler angles to converge to zero degree, but since a position error occurs, and the reference attitude changes based on the position error, so the flight attitude changes over time.



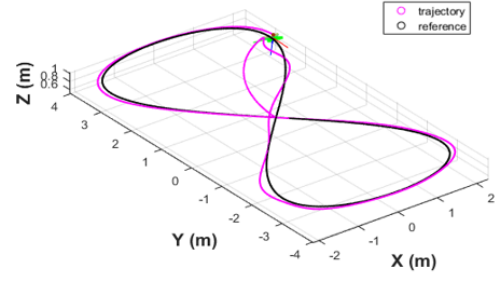
(a)



(b)



(c)



(d)

Figure 6.1: Simulation results of trajectory tracking; (a) Animation of tailless FWMAV, (b) Straight forward trajectory, (c) Circle trajectory, and (d) Number eight shape trajectory.

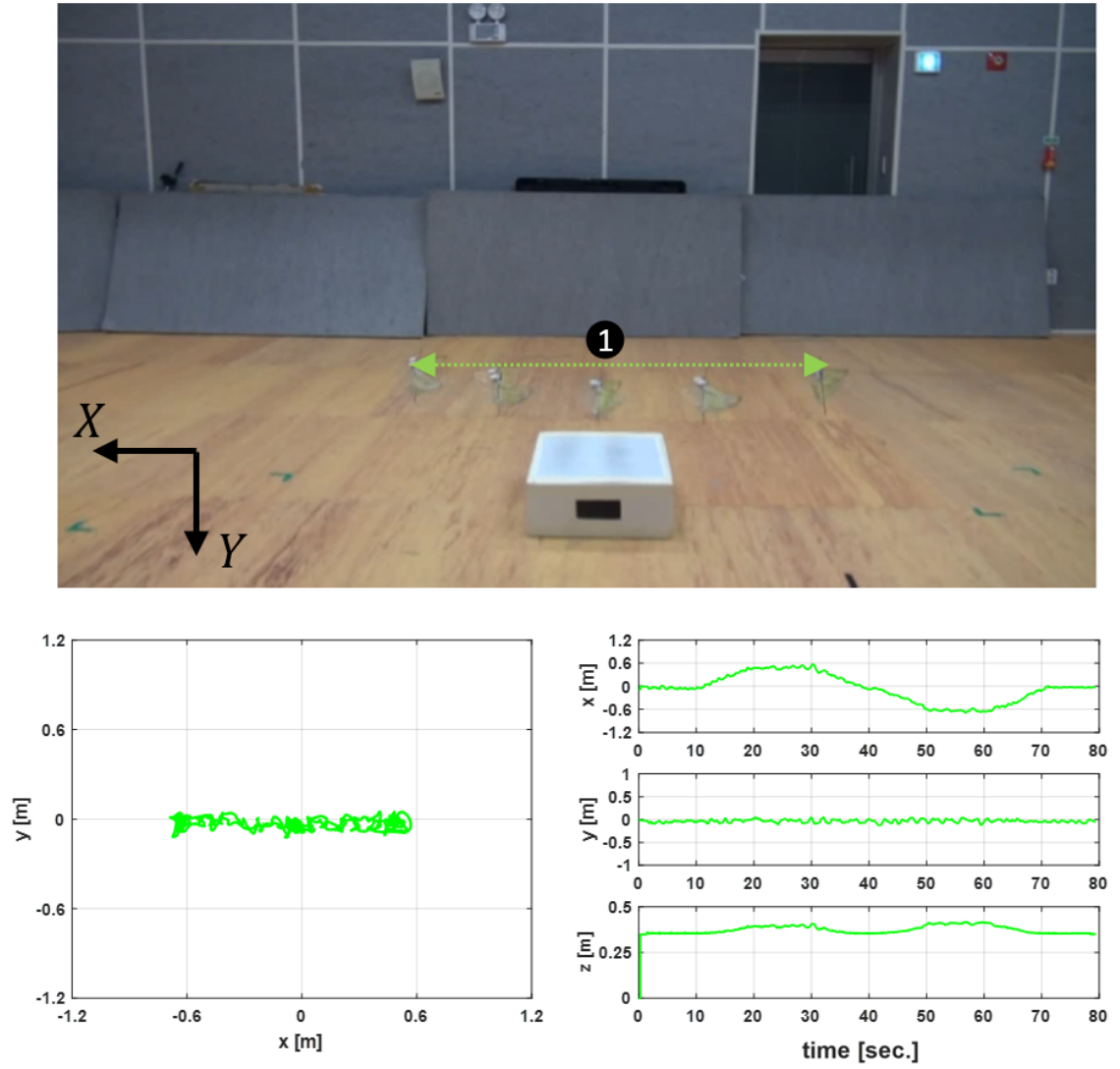


Figure 6.2: Tied-to-the-ceiling test: experimental results of moving toward \pm X-direction, (top) Overlaid sequence of snapshots of the platform during the experiment, (bottom-left) Trajectory in XY-plane, and (bottom-right) Time history of the position.

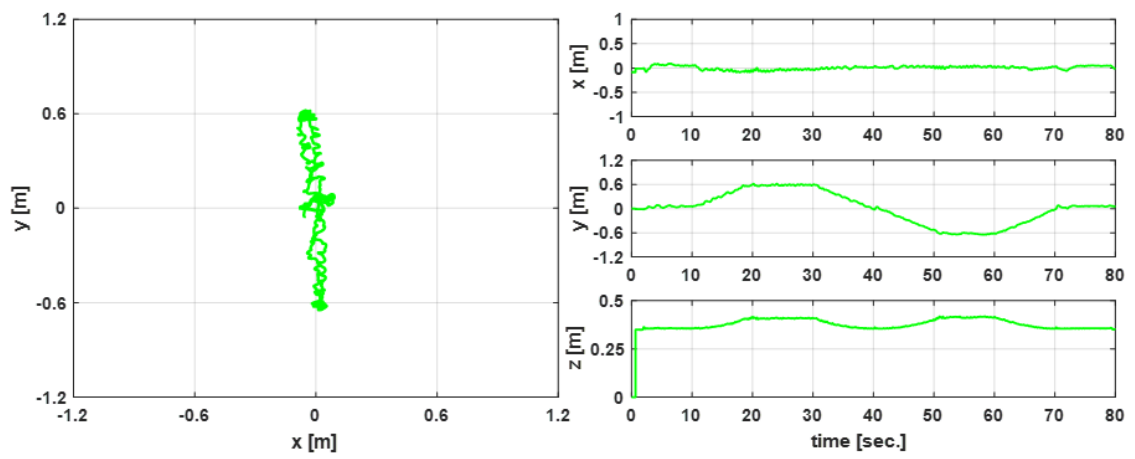
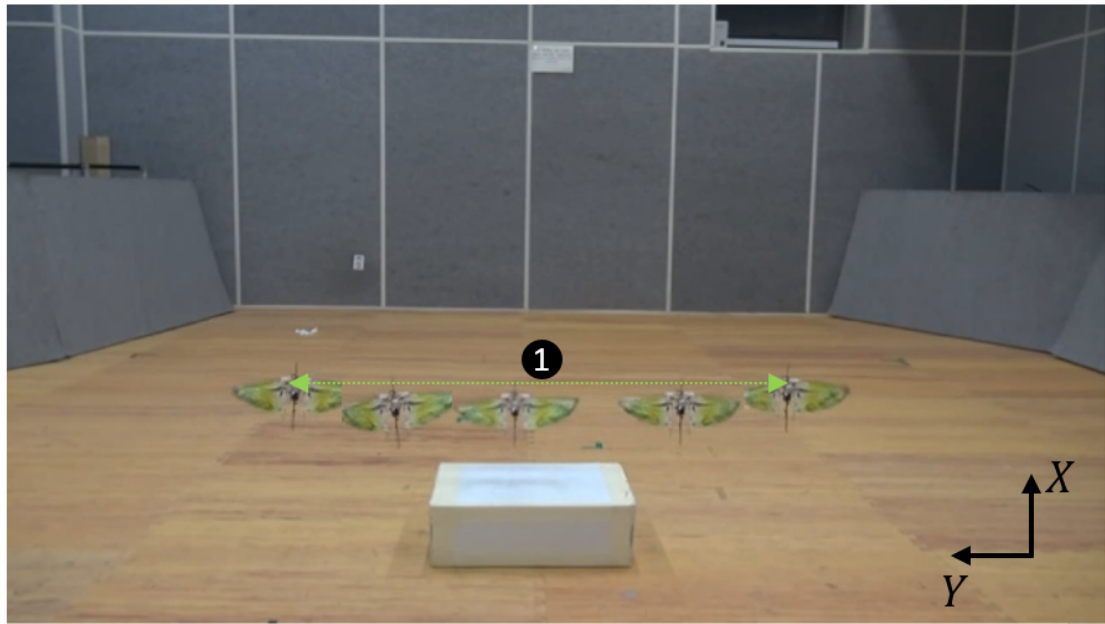


Figure 6.3: Tied-to-the-ceiling test: experimental results of moving toward $\pm Y$ -direction, (top) Overlaid sequence of snapshots of the platform during the experiment, (bottom-left) Trajectory in XY-plane, and (bottom-right) Time history of the position.

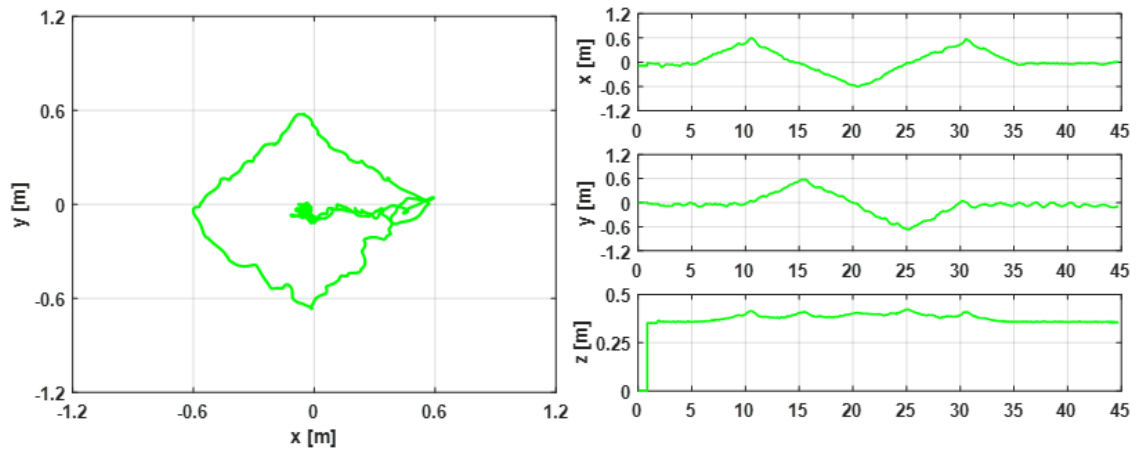
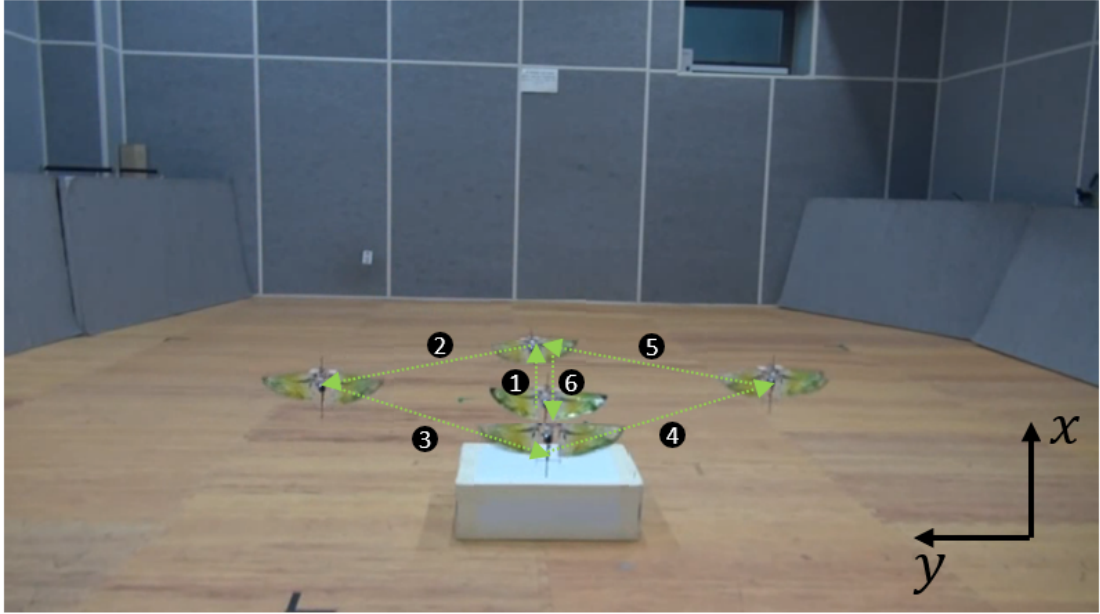


Figure 6.4: Tied-to-the-ceiling test: experimental results of moving toward square trajectory, (top) Overlaid sequence of snapshots of the platform during the experiment, (bottom-left) Trajectory in XY-plane, and (bottom-right) Time history of the position.

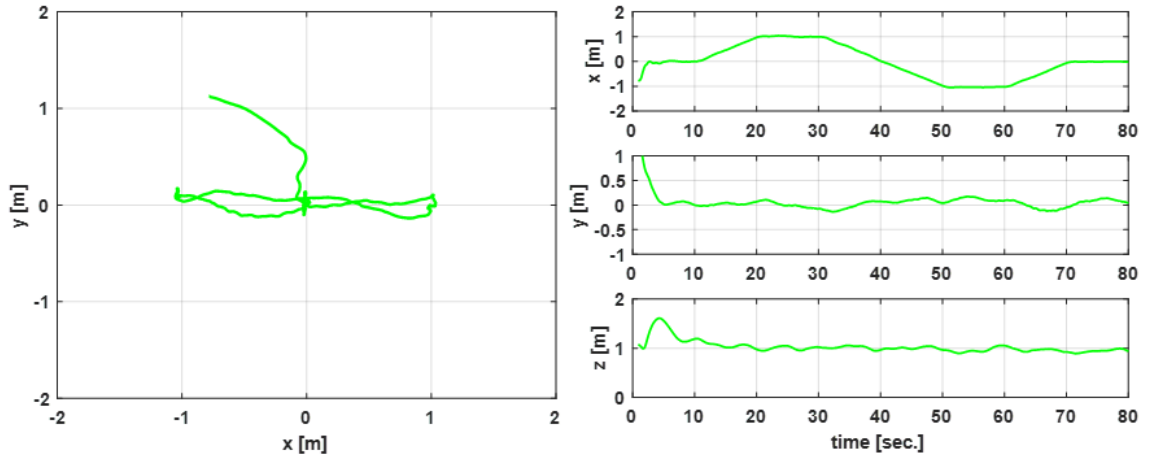
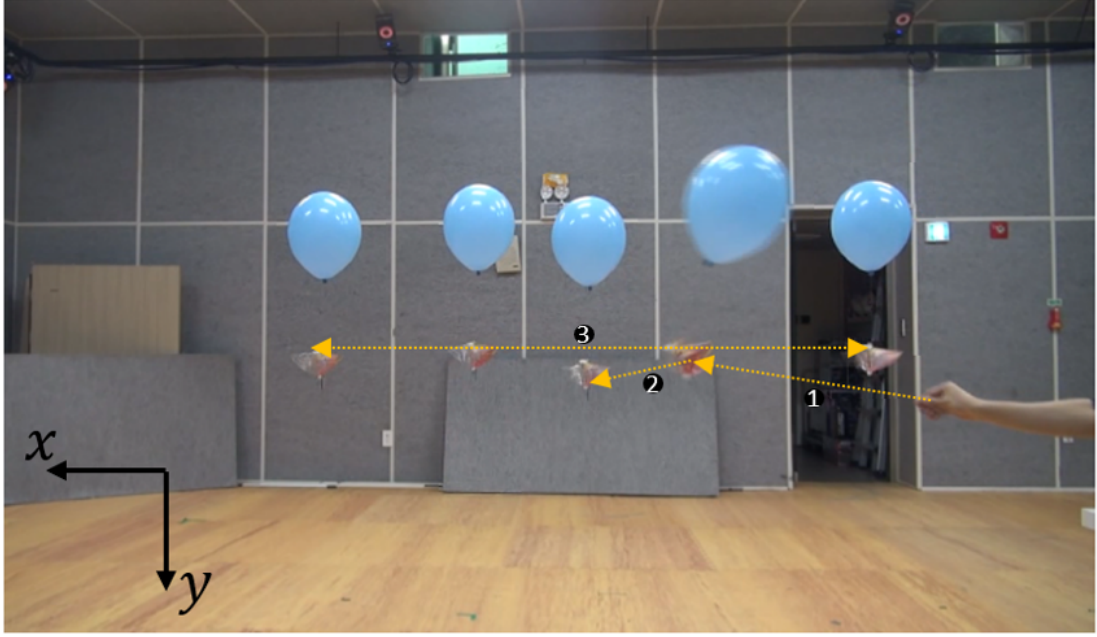


Figure 6.5: Hung-to-a-balloon test: experimental results of moving toward $\pm X$ -direction, (top) Overlaid sequence of snapshots of the platform during the experiment, (bottom-left) Trajectory in XY-plane, and (bottom-right) Time history of the position.

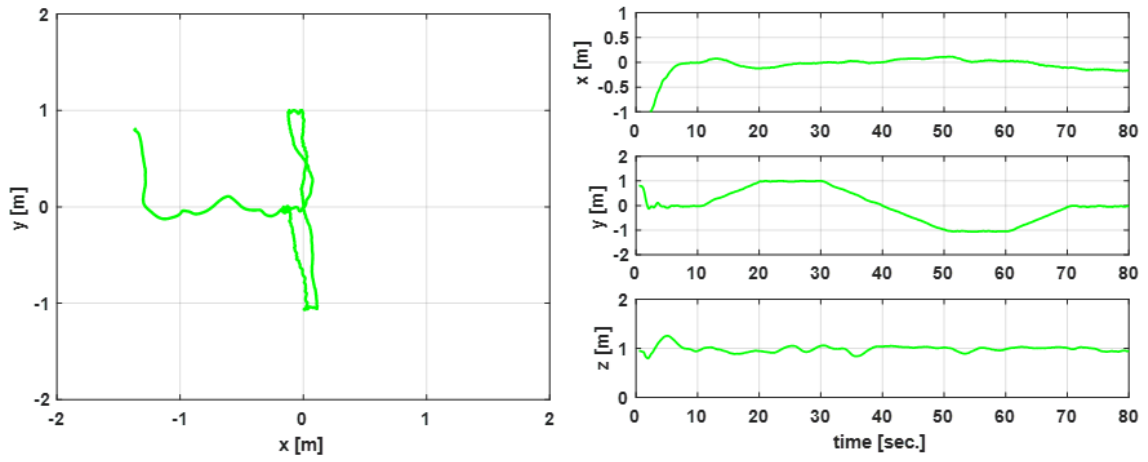
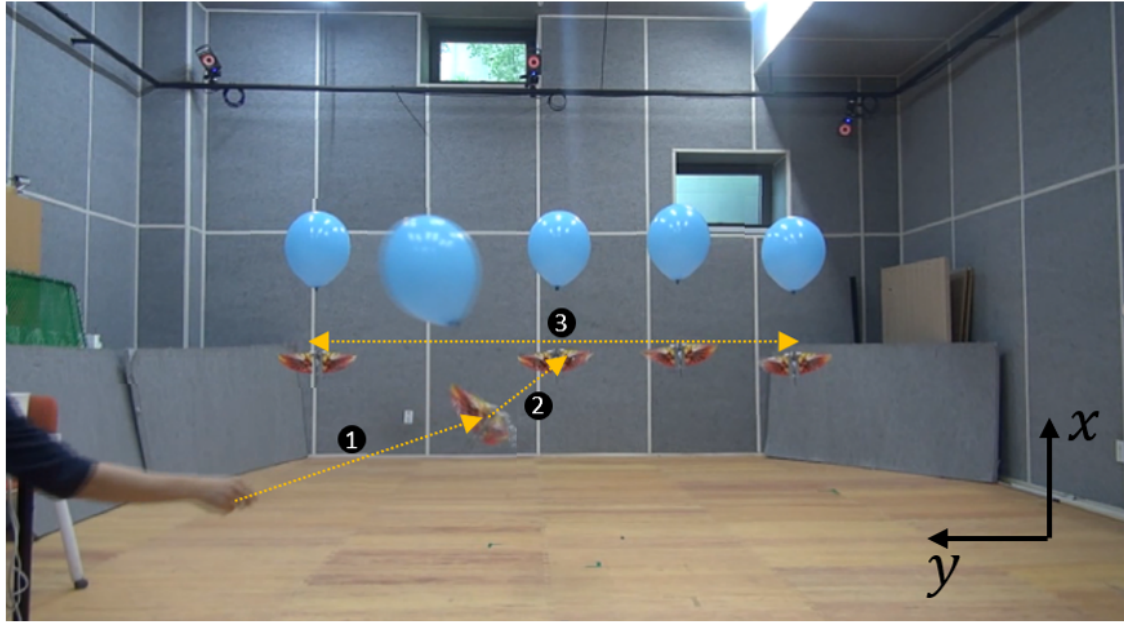


Figure 6.6: Hung-to-a-balloon test: experimental results of moving toward $\pm Y$ -direction, (top) Overlaid sequence of snapshots of the platform during the experiment, (bottom-left) Trajectory in XY-plane, and (bottom-right) Time history of the position.

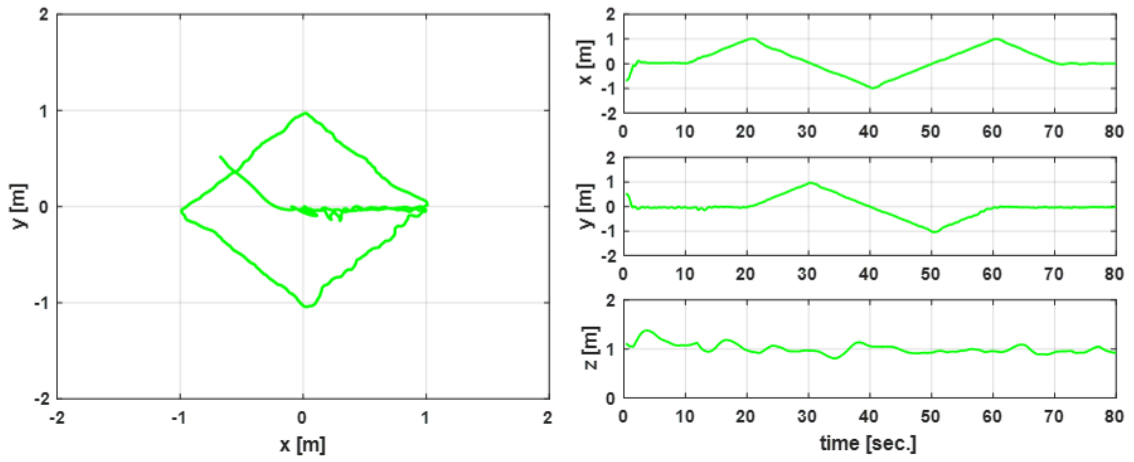
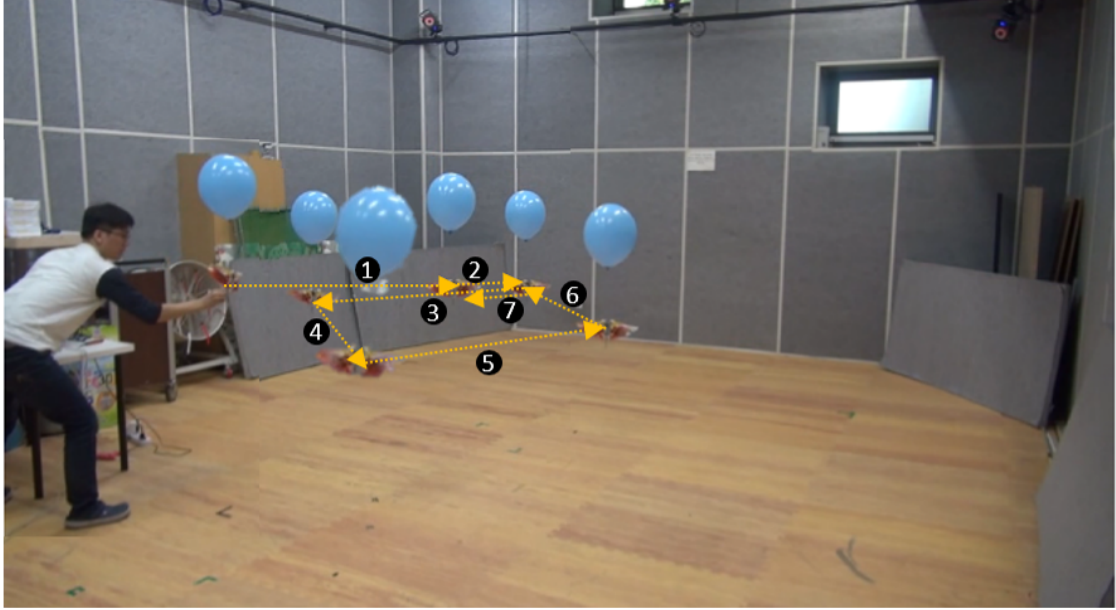


Figure 6.7: Hung-to-a-balloon test: experimental results of moving toward square trajectory, (top) Overlaid sequence of snapshots of the platform during the experiment, (bottom-left) Trajectory in XY-plane, and (bottom-right) Time history of the position.

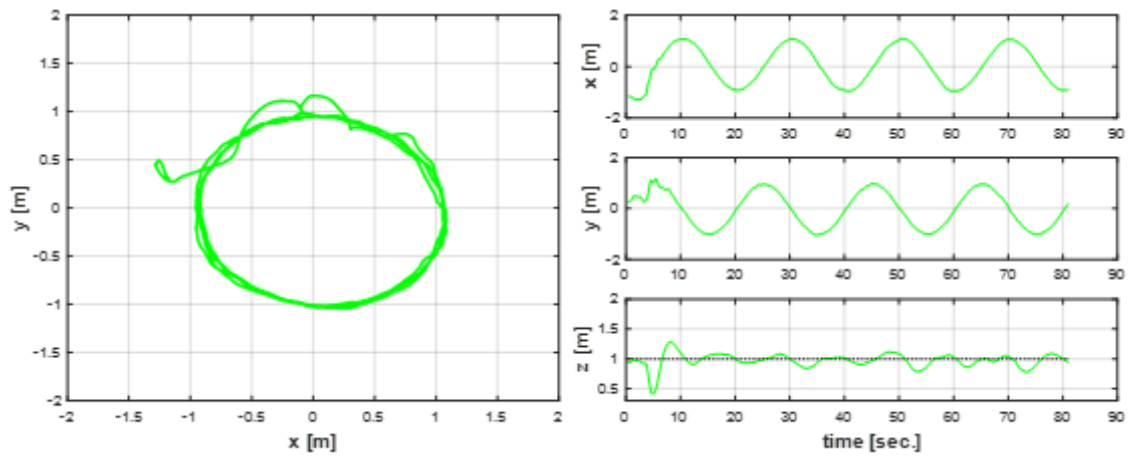
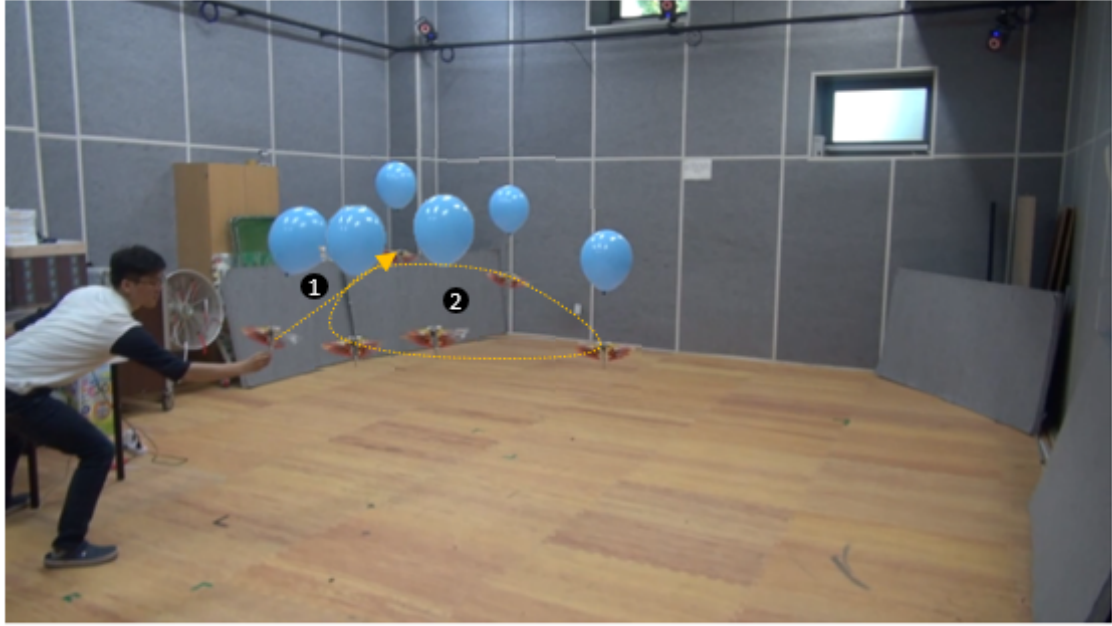
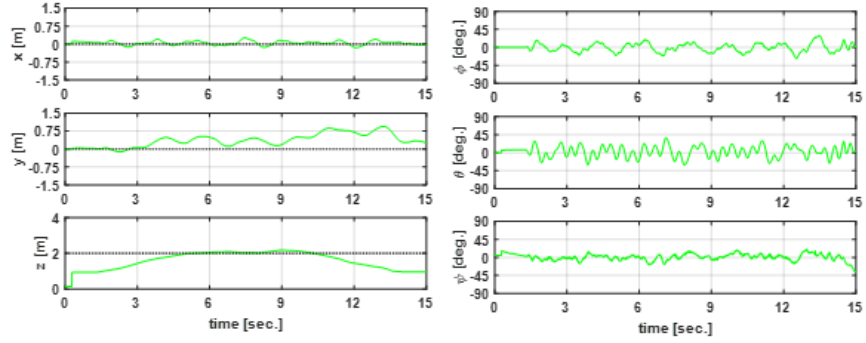


Figure 6.8: Hung-to-a-balloon test: experimental results of moving toward circle trajectory, (top) Overlaid sequence of snapshots of the platform during the experiment, (bottom-left) Trajectory in XY-plane, and (bottom-right) Time history of the position.

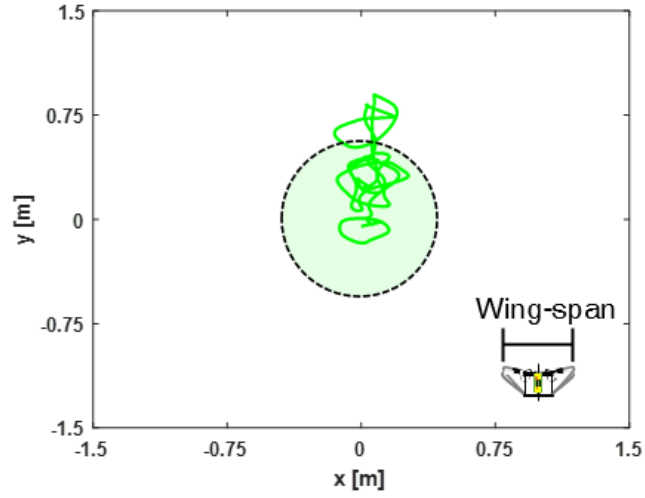


(a)



(b)

(c)



(d)

Figure 6.9: Experimental results of hovering flight, (a) Overlaid sequence of snapshots of the platform during the experiment, (b) Time history of the position, (c) Time history of the attitude, and (d) Trajectory in XY-plane.

7

Conclusion

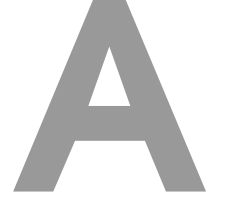
In this thesis, I developed a tailless FWMAV, after modification to a commonly available RC-toy with off-the-shelf electronic components. The designed aerial-platform was 25 grams in mass and $38 \times 14 \times 3.5 \text{ cm}^3$ in size, so it is able to meet the initial design targets. The result of thrust and moment measurement showed that the platform can generate enough force to support its weight as well as the control moments to rotate in the three axes. In addition, I validated that the PID type controller, which is derived by dynamic equations in parallel structure, is useful for attitude regulation through the gyroscope testbed and universal joint testbed. Based on the results, I conducted an autonomous flight test for tracking diverse trajectories in two situations such as tied-to-the-ceiling and hung-to-a-balloon, and hovering flight without external assistance. I achieved the goal with a well-regulated attitude and trajectory in all cases.

Although I used external assistance during trajectory tracking flight in a tethered environment and the flight time of the platform is not long enough during hover flight, the attainment of this thesis is a foothold for the related research areas as an early attempt to follow a trajectory using a tailless FWMAV equipped with a power source. In addition, my experiences with comprehensive consideration of structure design, power supply, and control strategy provide a stepping stone for research about autonomous tailless FWMAVs.

Software and hardware need to be further improved to increase sufficient flight time and

design a controller based on the identification of longitudinal and lateral dynamics of the tailless FWMAV. Details are as follows:

- Mass reduction is essential to increase the flight time of a tailless FWMAV. For this, FCS board, which is 14 percent of the total weight, should be integrated into one printed circuit board (PCB). In addition, the platform's frames and wires, which account for 18 percent of the total weight, should be revised to save mass and use less thrust.
- I will devise a new type of wing mechanism to reduce the mass of the platform and propose a tailored control method for the mechanism.
- By reducing the mass of the platform, it will be able to secure sufficient payload. After then, I will mount a FPV camera on the tailless FWMAV to study the application area such as obstacle avoidance and object tracking.



Appendix: Wing gearbox

A.1 4-bar linkage structure

4-bar linkage structures consist of ‘slider-crank linkage’ and ‘planar quadrilateral linkage’. They have only 1-degrees of freedom (DOF) according to ‘Grueble rule’ in Eq. (A.1) where n is the total number of links and j is the total number of joints. i.e., both cases have $n = 4$ and $j = 4$.

$$F = 3(n - 1) - 2j = 1 \quad (\text{A.1})$$

Depending on whether at least one link can be fully rotated or not, the planar quadrilateral linkage can be divided again into ‘Grashof structure’ and ‘non-Grashof structure’. If Eq. (A.2) is satisfied, it is ‘Grashof structure’, otherwise it is ‘non-Grashof structure’.

$$S + L < l_1 + l_2 \quad (\text{A.2})$$

where S is the length of the shortest link, L is the length of the longest link, l_1 and l_2 are the lengths of remaining two links.

There are three groups of ‘Grashof structure’, i.e., a double-rocker, double-crank, and crank-rocker. Table A.1 shows how the input and output links move respectively on each linkage structure.

Type	Input link	Output link
Double-rocker	partial rotation	partial rotation
Double-crank	full rotation	full rotation
Crank-rocker	full rotation	partial rotation

Table A.1: The movement of the links according to the ‘Grashof structure’.

B

Appendix: Disturbance observer (DOB)

B.1 DOB controller

It is not easy to respond effectively to modeling errors and disturbances, which are always a problem in the control system, using only the general controller design method. Therefore, proper application of advanced control methods such as adaptive control and optimal control is required, but these techniques have a disadvantage in that they are complicated to implement.

Designing a disturbance observer (DOB)-based controller is known to be able to compensate for modeling errors and effectively suppress the effects of disturbances while being relatively simple to implement compared to other control techniques. The corresponding method is used to control the flight attitude of FWMAs in [63, 64].

Fig. B.1 shows the block diagram of DOB structure. $C(s)$ is a general controller. $P(s)$ represents the actual plant and $P_n(s)$ is a nominal plant. $Q(s)$ is the transfer function of Q-filter which is a low-pass filter. r is reference signal and u_c is the control input signal that is generated by an outer-loop controller, d is disturbance, \hat{d} represents estimated disturbance, and y is system output. The output y is written in the following form:

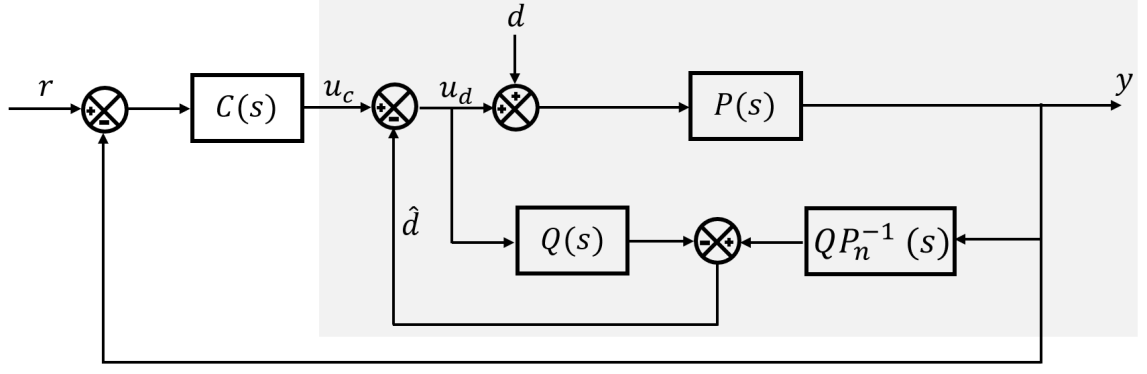


Figure B.1: Disturbance observer (DOB) signal flow.

$$\begin{aligned}
 y(s) &= P_{yr}(s)u(s) + P_{yd}d(s) \\
 \text{where } P_{yr} &= \frac{PP_n}{P_n + (P - P_nQ)}, \quad P_{yd} = \frac{PP_n(1 - Q)}{P_n + (P - P_nQ)} \\
 Q(s) &= \frac{\sum_{i=0}^n C_i(\tau s)^i}{(\tau s + 1)^m}, \quad Q(0) = 0
 \end{aligned} \tag{B.1}$$

and estimated disturbance is given by

$$\hat{d}(s) = QP_n^{-1}(y - QP_nu_d), \text{ where } u_d = u_c - \hat{d} \tag{B.2}$$

In low frequency range, $Q(s) \approx 1$, $P_{yr} \approx P_n$ and $P_{yd} \approx 0$. Therefore, the output y can be simplified to

$$y(s) = P_nu(s) \tag{B.3}$$

From Eq. (B.3), 1) the input disturbance d does not affect the output of the system and 2) the output of the system is determined by the nominal model P_n . Therefore, it is important to determine proper Q and P_n to achieve good control performance using DOB-based control.

The following conditions must be satisfied to stabilize the disturbance observer-based control system [63].

- $P_nC/(1 + P_nC)$ is stable.
- Ps is minimum phase system.

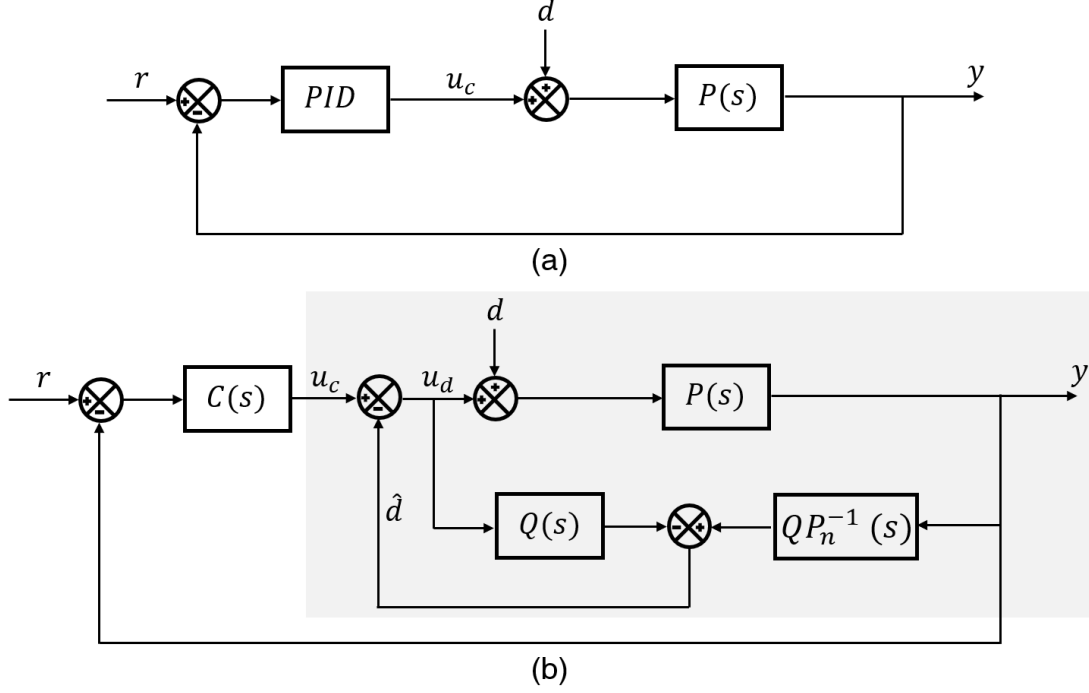


Figure B.2: Block diagram of control-loop; (a) PID, (b) PID+DOB.

B.2 Simulation

To confirm the responsiveness of DOB structure in an environment with disturbance, the simulation is conducted by considering roll and pitch axes independently about two reference angles such as step input and sine input. Table B.1 shows the parameters of the simulation environment and the parameters of the tailless FWMAV are shown in Table B.2. For the model transfer function of each axis, the dynamics derived in Section 4.2 is used and the same type of Q-filter is used to both cases. I assume that the frequency of disturbance to the roll axis is smaller than the pitch axis.

B.2.1 Step input

Fig. B.3 shows the simulation result of the PID controller and DOB+PID controllers about the step input, where the reference input starts from the initial 0 degree and changes to 10 degrees at 5 seconds. At the disturbance frequency of 0.25, the pitch angle is divergent when using only

	Roll direction	Pitch direction
Plant $P(s)$	$\ddot{\phi} = \frac{l}{J_x}(F_r - F_l)$	$\ddot{\psi} = -\frac{F}{J_y}l$
Controller $C(s)$	$K_p : 0.005, K_I : 0.0002, K_D : 0.03$	$K_p : -0.015, K_I : -0.001, K_D : -0.005$
Q-filter	$m : 4, n : 2, \tau : 0.01$	$m : 4, n : 2, \tau : 0.01$
Disturbance	$1.5 \cdot \sin(2\pi \cdot 0.25 \cdot t) + 0.25$	$2 \cdot \sin(2\pi \cdot 1.5 \cdot t) + 2$
Reference 1	$10 \cdot \text{step}(t - 5)$	$10 \cdot \text{step}(t - 5)$
Reference 2	$10 \cdot \sin(2\pi \cdot 0.5 \text{ or } 1 \cdot t)$	$10 \cdot \sin(2\pi \cdot 0.5 \text{ or } 1 \cdot t)$

Table B.1: Parameters of the simulation environment.

Symbol	Description	Value
m	Mass	25
g	Acceleration of gravity	9.8
J_x	X-moment of inertial	$5.2 \cdot 10^{-3}$
J_y	Y-moment of inertial	$1.9 \cdot 10^{-3}$

Table B.2: Parameters of the tailless FWMAV.

PID control. Therefore, I plot the response of the pitch angle using the disturbance frequency of 0.001.

In the case of the roll axis, when only the PID controller is used, the attitude is affected by the disturbance, and the roll angle vibrates along with the same disturbance frequency. On the other hand, when DOB-based controller is used together, the attitude follows the reference angle well.

In the case of the pitch axis, when only the PID controller is used (under very low disturbance frequency), the attitude does not diverge, but it does not follow the reference angle. In the case of using DOB, although there exists a little vibration, the attitude follows the reference angle well. In particular, since the pitch axis is more sensitive than the roll axis, it can be confirmed that a relatively large overshoot occurs when a step input is applied at 5 seconds.

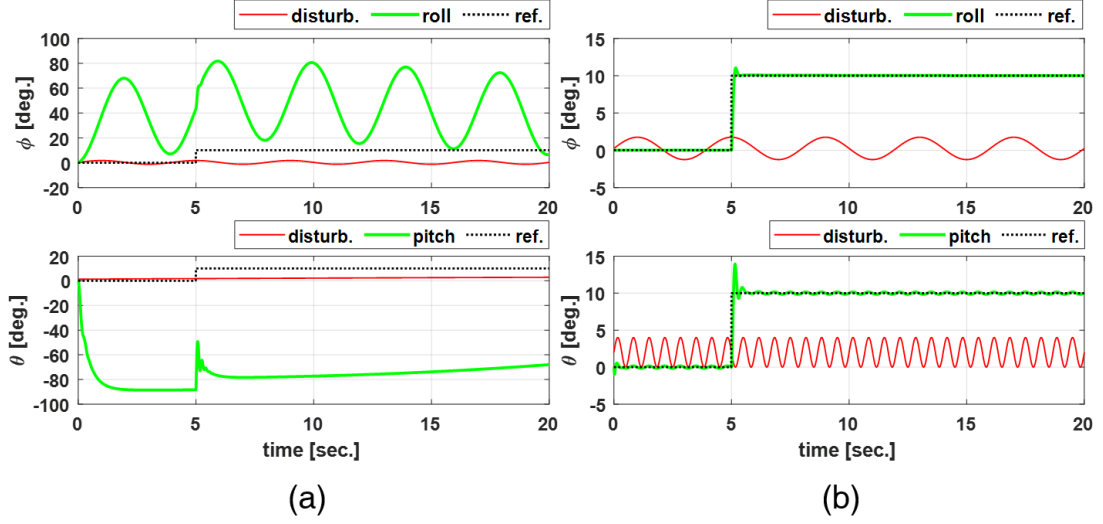


Figure B.3: Time history of Euler angles based on two types of controllers by step input; (a) PID controller, (b) PID+DOB controllers.

B.2.2 Sinusoid input

The simulation result of the PID controller and DOB+PID controllers about the sine input is shown in Fig. B.4. The pitch angle is divergent when only PID controller is used at the disturbance frequency of 1.5. Therefore, I plot the response of the pitch angle using the disturbance frequency of 0.001.

In the case of the roll axis, when only the PID controller is used, the attitude is affected by the disturbance, and the roll angle vibrates along with the same disturbance frequency. On the other hand, the attitude follows the reference angle well when using DOB-based controller. In the case of the pitch axis, although a little overshoot occurs at positive and negative poles, the attitude state follows the reference angle well when using DOB-based controller.

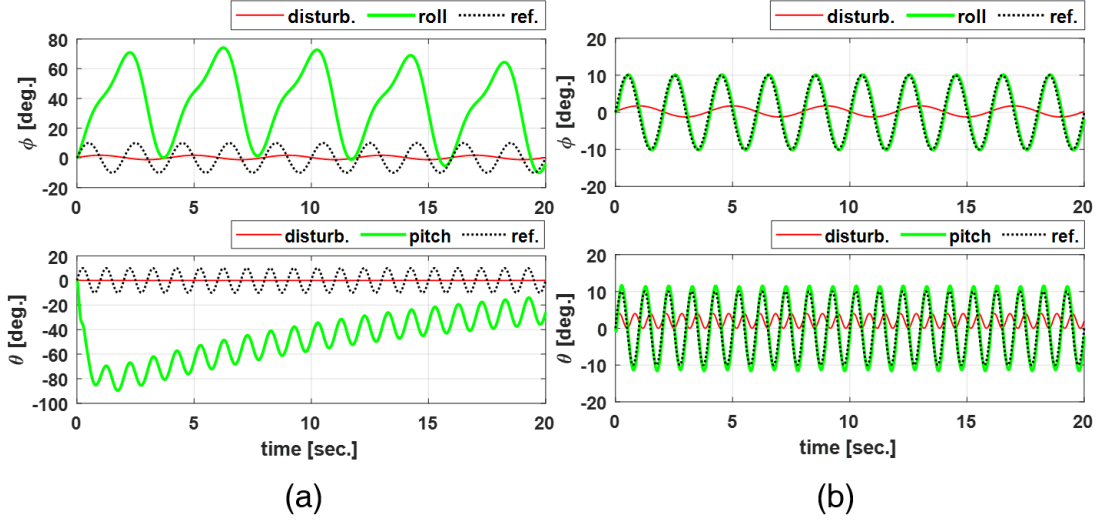


Figure B.4: Time history of Euler angles based on two types of controllers by sine input; (a) PID controller, (b) PID+DOB controllers.

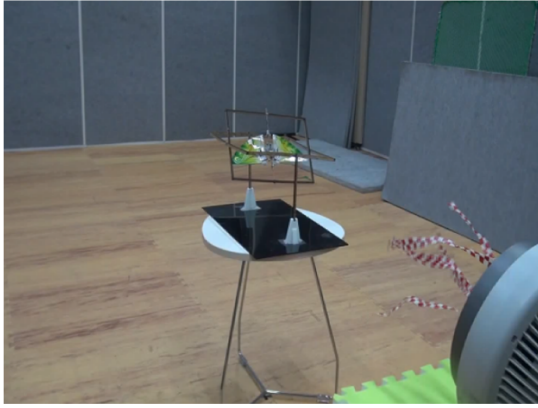
B.3 Experiment

Fig. B.5.(a) shows the experimental environment for verifying the performance of the DOB controller. The fan is located 1 m away from the gyroscope device and is positioned so that the center of the fan matches the center of the testbed. At that location, I measure the amount of wind using a wind gauge, and the measured value is about 2 m/s. From Table B.3, 2 m/s is included in the degree to which the branches shake. To disturb the platform, I shake the fan back and forth and from side to side at the position where the fan is placed so that wind is applied to the vehicle. Fig. B.5.(b) shows how much shaking occurs on the vehicle when the actuators of the platform are not operating. (The initial attitude of the vehicle is directed at a certain angle, but the offset is added to the angle, so the attitude is shifted to zero degrees to draw a graph.)

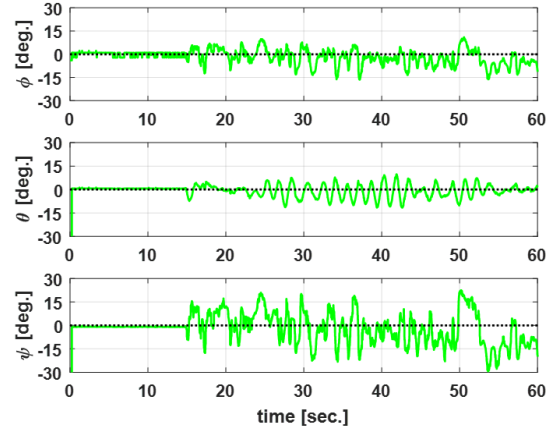
Fig. B.6 shows the experimental results for verifying the performance of the DOB controller. The disturbance is applied around 12 seconds after the vehicle maintains a stable attitude. In the case of Fig. B.6.(a), when there is no wind disturbance, the vehicle maintains a stable attitude but it loses its attitude as soon as the wind blows. On the other hand, even in windy conditions, the platform maintains a stable attitude in Fig. B.6.(b).

Description	Wing speed [m/s]	Specifications
Clam	0 ~ 0.2	smoke goes up straight.
Light air	0.3 ~ 1.5	smoke goes up at an angle
Slight breeze	1.6 ~ 3.3	leave shakes.
Gentle breeze	3.4 ~ 5.4	flag shakes.

Table B.3: Beaufort wing scale.



(a)



(b)

Figure B.5: Experimental environment for validating DOB-based control structure; (a) Actual experimental environment, (b) Time history of Euler angles in wind disturbance.

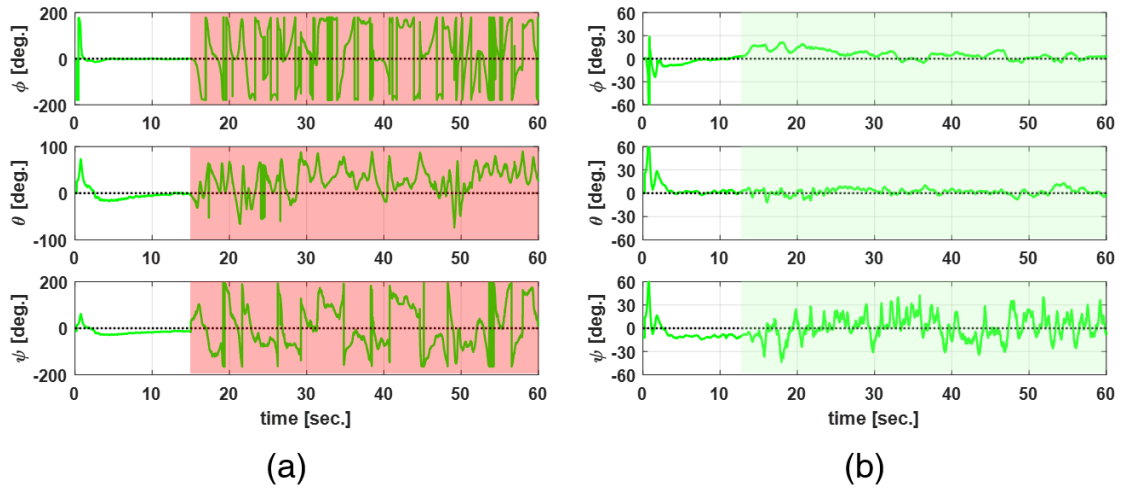


Figure B.6: Experimental results for validating DOB-based controller; (a) PID controller, (b) PID+DOB controllers.

References

- [1] Niquille, Simone C. “Regarding the Pain of SpotMini: Or What a Robot’s Struggle to Learn Reveals about the Built Environment.” *Architectural Design* 89.1 (2019): 84-91.
- [2] Ramezani, Alireza, Soon-Jo Chung, and Seth Hutchinson. “A biomimetic robotic platform to study flight specializations of bats.” *Science Robotics* 2.3 (2017): Art-No.
- [3] Laschi, Cecilia. “Octobot-A robot octopus points the way to soft robotics.” *IEEE Spectrum* 54.3 (2017): 38-43.
- [4] Santos, Daniel, et al. “Gecko-inspired climbing behaviors on vertical and overhanging surfaces.” 2008 IEEE International Conference on Robotics and Automation. IEEE, 2008.
- [5] Folkertsma, Gerrit Adriaan, et al. “Robird: a robotic bird of prey.” *IEEE robotics & automation magazine* 24.3 (2017): 22-29.
- [6] Katzschnmann, Robert K., et al. “Exploration of underwater life with an acoustically controlled soft robotic fish.” *Science Robotics* 3.16 (2018).
- [7] Phan, Hoang Vu, and Hoon Cheol Park. “Insect-inspired, tailless, hover-capable flapping-wing robots: Recent progress, challenges, and future directions.” *Progress in Aerospace Sciences* 111 (2019): 100573.
- [8] Gerdes, John W., Satyandra K. Gupta, and Stephen A. Wilkerson. “A review of bird-inspired flapping wing miniature air vehicle designs.” *Journal of Mechanisms and Robotics* 4.2 (2012).
- [9] Paranjape, Aditya A., et al. “A flight mechanics-centric review of bird-scale flapping flight.” *International Journal of Aeronautical and Space Sciences* 13.3 (2012): 267-281.
- [10] Taha, Haithem E., Muhammad R. Hajj, and Ali H. Nayfeh. “Flight dynamics and control of flapping-wing MAVs: a review.” *Nonlinear Dynamics* 70.2 (2012): 907-939.
- [11] Ward, Thomas A., et al. “A review of biomimetic air vehicle research: 1984-2014.” *International Journal of Micro Air Vehicles* 7.3 (2015): 375-394.

- [12] Hu, Hui, et al. "An experimental investigation on the aerodynamic performances of flexible membrane wings in flapping flight." *Aerospace Science and Technology* 14.8 (2010): 575-586.
- [13] Sibilski, Krzysztof, Jozef Pietrucha, and Maria Zlocka. "Comparative evaluation of power requirements for fixed, rotary, and flapping wings micro air vehicles." *AIAA atmospheric flight mechanics conference and exhibit*. 2002.
- [14] Ellington, Charles P. "The novel aerodynamics of insect flight: applications to micro-air vehicles." *Journal of Experimental Biology* 202.23 (1999): 3439-3448.
- [15] Jackowski, Zachary John. Design and construction of an autonomous ornithopter. Diss. Massachusetts Institute of Technology, 2009.
- [16] De Croon, Guido CHE, et al. "Design, aerodynamics and autonomy of the DelFly." *Bioinspiration & biomimetics* 7.2 (2012): 025003.
- [17] De Wagter, Christophe, et al. "Autonomous flight of a 20-gram flapping wing mav with a 4-gram onboard stereo vision system." *2014 IEEE International Conference on Robotics and Automation (ICRA)*. IEEE, 2014.
- [18] Ryu, Seungwan, Ukjin Kwon, and H. Jin Kim. "Autonomous flight and vision-based target tracking for a flapping-wing mav." *2016 IEEE/RSJ International Conference on Intelligent Robots and Systems (IROS)*. IEEE, 2016.
- [19] Julian, Ryan C., et al. "Cooperative control and modeling for narrow passage traversal with an ornithopter MAV and lightweight ground station." *Proceedings of the 2013 international conference on Autonomous agents and multi-agent systems*. 2013.
- [20] http://www.ornithopter.org/history_mav.shtml
- [21] <https://www.festo.com/group/en/cms/10238.htm>
- [22] <https://bionicbird.com/world/shop/metafly>
- [23] Peters, Hugo J., Johannes FL Goosen, and Fred van Keulen. "Optimal fw mav wing design for a combination of energy-effective hovering and roll control." *International Journal of Micro Air Vehicles* 7.1 (2015): 41-53.

- [24] De Croon, G. C. H. E., et al. "Design, aerodynamics, and vision-based control of the DeFly." *International Journal of Micro Air Vehicles* 1.2 (2009): 71-97.
- [25] Widhiarini, Sriyulianti, et al. "Bird-mimetic wing system of flapping-wing micro air vehicle with autonomous flight control capability." *Journal of Bionic Engineering* 13.3 (2016): 458-467.
- [26] Ryu, Seung Wan, Jong Gu Lee, and Hyoun Jin Kim. "Design, Fabrication, and Analysis of Flapping and Folding Wing Mechanism for a Robotic Bird." *Journal of Bionic Engineering* 17 (2020): 229-240.
- [27] Orlowski, Christopher T., and Anouck R. Girard. "Modeling and simulation of nonlinear dynamics of flapping wing micro air vehicles." *AIAA journal* 49.5 (2011): 969-981.
- [28] Caetano, Joao V., et al. "Linear aerodynamic model identification of a flapping wing mav based on flight test data." *International Journal of Micro Air Vehicles* 5.4 (2013): 273-286.
- [29] 류승완. System Identification and Tracking Control of a Flapping Wing Micro Air Vehicle. Diss. 서울대학교 대학원, 2015.
- [30] Armanini, S. F., et al. "Time-varying model identification of flapping-wing vehicle dynamics using flight data." *Journal of Guidance, Control, and Dynamics* 39.3 (2016): 526-541.
- [31] Baek, Stanley S., and Ronald S. Fearing. "Flight forces and altitude regulation of 12 gram i-bird." 2010 3rd IEEE RAS & EMBS International Conference on Biomedical Robotics and Biomechatronics. IEEE, 2010.
- [32] Lee, Jun-seong, et al. "Periodic tail motion linked to wing motion affects the longitudinal stability of ornithopter flight." *Journal of Bionic Engineering* 9.1 (2012): 18-28.
- [33] Ryu, Seungwan, and H. Jin Kim. "Development of a flapping-wing micro air vehicle capable of autonomous hovering with onboard measurements." 2017 IEEE/RSJ International Conference on Intelligent Robots and Systems (IROS). IEEE, 2017.
- [34] Bermudez, Fernando Garcia, and Ronald Fearing. "Optical flow on a flapping wing robot." 2009 IEEE/RSJ International Conference on Intelligent Robots and Systems. IEEE, 2009.

- [35] Baek, Stanley S., Fernando L. Garcia Bermudez, and Ronald S. Fearing. “Flight control for target seeking by 13 gram ornithopter.” 2011 IEEE/RSJ International Conference on Intelligent Robots and Systems. IEEE, 2011.
- [36] Keennon, Matthew, Karl Klingebiel, and Henry Won. “Development of the nano hummingbird: A tailless flapping wing micro air vehicle.” 50th AIAA aerospace sciences meeting including the new horizons forum and aerospace exposition. 2012.
- [37] Coleman, David, et al. “Design, development and flight-testing of a robotic hummingbird.” AHS 71st annual forum. 2015.
- [38] Nguyen, Quoc-Viet, and Woei Leong Chan. “Development and flight performance of a biologically-inspired tailless flapping-wing micro air vehicle with wing stroke plane modulation.” *Bioinspiration & biomimetics* 14.1 (2018): 016015.
- [39] Phan, Hoang Vu, Taesam Kang, and Hoon Cheol Park. “Design and stable flight of a 21 g insect-like tailless flapping wing micro air vehicle with angular rates feedback control.” *Bioinspiration & biomimetics* 12.3 (2017): 036006.
- [40] Karásek, Matěj, et al. “A tailless aerial robotic flapper reveals that flies use torque coupling in rapid banked turns.” *Science* 361.6407 (2018): 1089-1094.
- [41] Roshanbin, Ali, Emanuele Garone, and André Preumont. “Precision Stationary Flight of a Robotic Hummingbird.” 2019 International Conference on Robotics and Automation (ICRA). IEEE, 2019.
- [42] Ma, Kevin Y., et al. “Controlled flight of a biologically inspired, insect-scale robot.” *Science* 340.6132 (2013): 603-607.
- [43] Zhang, Jian, et al. “Adaptive robust wing trajectory control and force generation of flapping wing MAV.” 2015 IEEE International Conference on Robotics and Automation (ICRA). IEEE, 2015.
- [44] Fei, Fan, et al. “Learning extreme hummingbird maneuvers on flapping wing robots.” 2019 International Conference on Robotics and Automation (ICRA). IEEE, 2019.

- [45] Phan, Hoang Vu, et al. "KUBeetle-S: An insect-like, tailless, hover-capable robot that can fly with a low-torque control mechanism." *International Journal of Micro Air Vehicles* 11 (2019): 1756829319861371.
- [46] Phan, Hoang Vu, et al. "Towards Long-Endurance Flight of an Insect-Inspired, Tailless, Two-Winged, Flapping-Wing Flying Robot." *arXiv preprint arXiv:2005.06715* (2020).
- [47] Nelson, Robert C. *Flight stability and automatic control*. Vol. 2. New York: WCB/McGraw Hill, 1998.
- [48] Fry, Steven N., Rosalyn Sayaman, and Michael H. Dickinson. "The aerodynamics of free-flight maneuvers in *Drosophila*." *Science* 300.5618 (2003): 495-498.
- [49] Deng, Xinyan, et al. "Flapping flight for biomimetic robotic insects: Part I-system modeling." *IEEE Transactions on Robotics* 22.4 (2006): 776-788.
- [50] Khalil, Hassan K., and Jessy W. Grizzle. *Nonlinear systems*. Vol. 3. Upper Saddle River, NJ: Prentice hall, 2002.
- [51] Tayebi, Abdelhamid, and Stephen McGilvray. "Attitude stabilization of a VTOL quadrotor aircraft." *IEEE Transactions on control systems technology* 14.3 (2006): 562-571.
- [52] Hancer, Muhsin, Rahman Bitirgen, and Ismail Bayezit. "Designing 3-DOF Hardware-In-The-Loop Test Platform Controlling Multicopter Vehicles." *IFAC-PapersOnLine* 51.4 (2018): 119-124.
- [53] Motea, Zakarya M., and M. Shukri Z. Abidin. "Empirical Modeling and Control of Quadrotor Unmanned Aerial Vehicle."
- [54] Hunt, Rusty, Gregory S. Hornby, and Jason D. Lohn. "Toward evolved flight." *Proceedings of the 7th annual conference on Genetic and evolutionary computation*. 2005.
- [55] Anderson, Michael. "Design and Testing of Flapping Wing Control for a Micro Air Vehicle." *AIAA Guidance, Navigation, and Control Conference*. 2011.

- [56] Caetano, J. V., et al. “Tethered vs. free flight force determination of the DelFly II Flapping Wing Micro Air Vehicle.” 2014 International Conference on Unmanned Aircraft Systems (ICUAS). IEEE, 2014.
- [57] <https://micronwings.com/Products/MotorBrushed6mmx15mmNegativeTuned/index.shtml>
- [58] <https://micronwings.com/Products/Servo5330WhiteSH/index.shtml>
- [59] Teoh, Zhi Ern, et al. “A hovering flapping-wing microrobot with altitude control and passive upright stability.” 2012 IEEE/RSJ International Conference on Intelligent Robots and Systems. IEEE, 2012.
- [60] Altartouri, Hussein, et al. “Passive stability enhancement with sails of a hovering flapping twin-wing robot.” International Journal of Micro Air Vehicles 11 (2019): 1756829319841817.
- [61] Jafferis, Noah T., et al. “Untethered flight of an insect-sized flapping-wing microscale aerial vehicle.” Nature 570.7762 (2019): 491-495.
- [62] Zhang, Jian, et al. “Design optimization and system integration of robotic hummingbird.” 2017 IEEE International Conference on Robotics and Automation (ICRA). IEEE, 2017.
- [63] 김인래, 김승균, and 석진영. “구동기와 센서를 고려한 날갯짓 초소형 비행체의 외란관측기 기반 제어.” 제어로봇시스템학회 논문지 25.11 (2019): 950-959.
- [64] Jonggu Lee, Seungwan Ryu and H. Jin Kim, “Stable Flight of a Flapping-wing Micro Air Vehicle Under Wind Disturbance,” IEEE Robotics and Automation Letters (RA-L), 2020.
- [65] Shim, Hyungbo, and Nam H. Jo. “An almost necessary and sufficient condition for robust stability of closed-loop systems with disturbance observer.” Automatica 45.1 (2009): 296-299.

국 문 초 록

최근 생체모방에 대한 관심이 커지면서 생명체의 구조, 외형, 움직임, 행동을 분석하여 그들의 장점을 로봇에 적용시켜 기존의 로봇이 해결할 수 없거나 특별한 임무를 좀 더 효과, 효율적으로 해결하려는 시도가 늘어나고 있다. 이러한 시도는 무인비행체 개발에도 적용되고 있으며 날갯짓 비행체가 이에 해당된다. 날갯짓 비행체는 날개의 반복운동을 통해 발생하는 힘을 통해 비행하는 비행체로 일반적으로 꼬리날개의 유무에 따라 새를 모방한 비행체(미익형 비행체)와 곤충을 모방한 비행체(무미익형 비행체)로 구분할 수 있다. 무미익형 비행체의 경우 제자리 비행을 할 수 있고, 크기가 작고 무게가 가벼워 공기저항도 줄일 수 있으며, 날렵한 비행이 가능하다는 장점이 있지만, 수동 안정성을 확보하기 위한 제어면이 충분하지 않고 추력 생성과 동시에 3축으로의 제어 모멘트를 만들 수 있는 복잡한 매커니즘을 가지고 있다는 특징을 가지고 있다.

본 논문에서는 저자의 미익형 비행체의 연구개발 사례를 토대로 자율 비행을 할 수 있는 무미익형 비행체를 개발하기 위한 요소기술들과 초기 비행체 개발을 목표로 한다. 해당 목표를 달성하기 위해 저자는 시중에서 판매되고 있는 RC장난감을 활용해 30 gram 이하의 무게를 가지고 30cm³ 이내의 크기를 가지는 무미익형 날갯짓 비행체를 개발을 진행하였다. 비행체 내부에는 구동기로 DC 모터와 서보모터가 존재하며, DC 모터는 날갯짓을 일으키는 기어 박스를 작동시켜 비행체의 무게를 지탱하기 위한 thrust를 생성하며 roll축 방향으로의 moment 생성에 관여하며, 서보모터는 날갯짓에서 발생하는 좌우 thrust의 방향을 조절하여 pitch 와 yaw 축으로의 모멘트를 생성하는데 사용된다. 비행체 내부에는 아두이노 보드 기반의 마이크로프로세서가 탑재되어 있어 비행체를 제어하기 위한 신호를 생성할 수 있으며 블루투스 통신 모듈을 가지고 있기 때문에 외부와 통신 역시 가능하다.

비행체의 자세를 제어하기 위해서는 구동기의 상호작용으로 인해 발생하는 힘의 물리량을 파악하는 것이 중요하다. 이를 위해 날갯짓 메커니즘에서 발생하는 힘을 측정하는 실험을 수행하였다. 측정실험을 통해 DC모터 입력 대비 thrust 크기, 서보모터 command 입력 대비 moment 크기 등의 관계를 파악하였다. 또한 날갯짓 비행체를 공중에 띄울 수 있는 충분한 크기의 thrust를 발생하는 것을 확인하였으며 자세 제어를 위한 모멘트 생성 역시 가능하다는 것을 확인하였다.

비행체의 자세를 제어하기 위해서는 3축 방향으로의 운동방정식을 유도하는 것이 필요하다. 이를 위해 roll, pitch, yaw 축 방향으로 비행체에서 발생하는 힘과 회전 운동과 관련한 운동방정식을 유도했으며 이를 통해 비행체의 자세를 안정화시킬 수 있도록 하는 PID 제어기 형태의 제어기를 설계하였다. 뿐만 아니라, 비행체의 궤적추종 제어를 위해 내부의 자세 제어기에 비행체의 위치를

토대로 계산되는 추가적인 외부 제어기를 설계하여 이중루프 제어기 형태를 적용시켜 시뮬레이션을 통해 비행체의 자세 제어와 궤적 추종 제어가 이루어짐을 확인하였다.

개발한 비행체와 앞서 설계한 제어기가 사용자의 의도에 맞는 성능을 내는지 확인하기 위해 자이로 실험장치를 제작하여 자세 제어 실험을 수행하였다. 해당 실험장치는 roll, pitch, yaw 축으로 회전이 가능하도록 제작하였으며 실험장치 자체의 무게를 줄이기 위해 MDF 소재를 사용하여 구조물을 만들었다. roll, pitch, yaw 3축이 각각 독립적으로 제어하는 것과 3축을 동시에 제어하는 2가지 상황을 고려하였으며 앞서 설계한 제어기가 해당 실험 장치 내부에서 사용자의 의도에 맞게 제어 성능을 보이는지 확인할 수 있었다.

궤적 추종제어를 위해서는 2가지 비행 상황을 설정하였다. 첫 번째 경우, 천장과 비행체 상단부에 실을 연결하여 2D 평면상에서 비행체가 주워진 궤적에 따라 움직이는지, 두 번째 경우, 비행체 상단부에 헬륨이 주입된 풍선을 연결시켜 3D 공간상에서 주워진 궤적을 따라 추종 비행하는지를 확인할 수 있는 상황이다. 두 가지 상황에서 모두 다양한 형태의 궤적을 비행체가 잘 추종하는지를 확인할 수 있었다. 끝으로, 외부 장치(실, 풍선)를 제거하여 공중에서 비행체가 제자리 비행을 할 수 있는지를 검증하는 실험을 진행하였으며, 15초가량 1m³ 공간 내에서 제자리 비행이 이루어지는 것을 확인하였다.

주요어 : 날갯짓 비행체, 미익형 비행체, 무미익형 비행체, 자세제어, 궤적추종 제어

학번 : 2015-31002